

# Advanced Hybrid Functional Materials for Energy Applications

Lead Guest Editor: Iftikhar Ali Sahito

Guest Editors: Sung Hoon Jeong and Cheng-yu Hong





---

# **Advanced Hybrid Functional Materials for Energy Applications**

Journal of Nanomaterials

---

## **Advanced Hybrid Functional Materials for Energy Applications**

Lead Guest Editor: Iftikhar Ali Sahito

Guest Editors: Sung Hoon Jeong and Cheng-yu Hong



---

Copyright © 2018 Hindawi. All rights reserved.

This is a special issue published in "Journal of Nanomaterials." All articles are open access articles distributed under the Creative Commons Attribution License, which permits unrestricted use, distribution, and reproduction in any medium, provided the original work is properly cited.

## Editorial Board

- Domenico Acierno, Italy  
Katerina Aifantis, USA  
Nageh K. Allam, USA  
Margarida Amaral, Portugal  
Martin Andersson, Sweden  
Raul Arenal, Spain  
Ilaria Armentano, Italy  
Vincenzo Baglio, Italy  
Lavinia Balan, France  
Thierry Baron, France  
Andrew R. Barron, USA  
Stefano Bellucci, Italy  
Enrico Bergamaschi, Italy  
D. Bhattacharyya, New Zealand  
Sergio Bietti, Italy  
Giovanni Bongiovanni, Italy  
Mohamed Bououdina, Bahrain  
Victor M. Castaño, Mexico  
Albano Cavaleiro, Portugal  
Bhanu P. S. Chauhan, USA  
Shafiq Chowdhury, USA  
Yu-Lun Chueh, Taiwan  
Elisabetta Comini, Italy  
Giuseppe Compagnini, Italy  
David Cornu, France  
Miguel A. Correa-Duarte, Spain  
P. Davide Cozzoli, Italy  
Anuja Datta, USA  
Loretta L. Del Mercato, Italy  
Yong Ding, USA  
Yu Dong, Australia  
Zehra Durmus, Turkey  
Joydeep Dutta, Oman  
Ovidiu Ersen, France  
Ana Espinosa, France  
Claude Estournès, France  
Andrea Falqui, Saudi Arabia  
Matteo Ferroni, Italy  
Ilaria Fratoddi, Italy  
Siddhartha Ghosh, Singapore  
Filippo Giubileo, Italy  
Fabien Gresset, Japan  
Jean M. Greneche, France  
Kimberly Hamad-Schifferli, USA
- Simo-Pekka Hannula, Finland  
Michael Harris, USA  
Yasuhiko Hayashi, Japan  
Michael Z. Hu, USA  
Nay Ming Huang, Malaysia  
Zafar Iqbal, USA  
Balachandran Jeyadevan, Japan  
J.-w. Kang, Republic of Korea  
Hassan Karimi-Maleh, Iran  
Antonios Kelarakis, UK  
Alireza Khataee, Iran  
Ali Khorsand Zak, Iran  
Philippe Knauth, France  
Prashant Kumar, UK  
Eric Le Bourhis, France  
Jun Li, Singapore  
Meiyong Liao, Japan  
Shijun Liao, China  
Silvia Licocchia, Italy  
Nathan C. Lindquist, USA  
Zainovia Lockman, Malaysia  
Jim Low, Australia  
Gaurav Mago, USA  
Muhamamd A. Malik, UK  
F. Marotti de Sciarra, Italy  
Ivan Marri, Italy  
Laura Martinez Maestro, UK  
Sanjay R. Mathur, Germany  
Tony McNally, UK  
Yogendra Mishra, Germany  
Paulo Cesar Morais, Brazil  
Paul Munroe, Australia  
J.-M. Myoung, Republic of Korea  
Rajesh R. Naik, USA  
Albert Nasibulin, Russia  
Toshiaki Natsuki, Japan  
Hiromasa Nishikiori, Japan  
Natalia Noginova, USA  
Sherine Obare, USA  
Won-Chun Oh, Republic of Korea  
Abdelwahab Omri, Canada  
Ungyu Paik, Republic of Korea  
Edward A. Payzant, USA  
Alessandro Pegoretti, Italy
- Oscar Perales-Pérez, Puerto Rico  
Jorge Pérez-Juste, Spain  
Alexey P. Popov, Finland  
Thathan Premkumar, Republic of Korea  
Helena Prima-García, Spain  
Alexander Pyatenko, Japan  
Haisheng Qian, China  
You Qiang, USA  
Philip D. Rack, USA  
Peter Reiss, France  
Ilker S. Bayer, Italy  
Lucien Saviot, France  
Sudipta Seal, USA  
Shu Seki, Japan  
Donglu Shi, USA  
Bhanu P. Singh, India  
Surinder Singh, USA  
Vladimir Sivakov, Germany  
Adolfo Speghini, Italy  
Marinella Striccoli, Italy  
Fengqiang Sun, China  
Xuping Sun, Saudi Arabia  
Ashok K. Sundramoorthy, India  
Angelo Taglietti, Italy  
Bo Tan, Canada  
Leander Tapfer, Italy  
Valeri P. Tolstoy, Russia  
Muhammet S. Toprak, Sweden  
R. Torrecillas, Spain  
Achim Trampert, Germany  
Takuya Tsuzuki, Australia  
Tamer Uyar, Turkey  
Luca Valentini, Italy  
Antonio Vassallo, Italy  
Ester Vazquez, Spain  
Ajayan Vinu, Australia  
Ruibing Wang, Macau  
Shiren Wang, USA  
Yong Wang, USA  
Magnus Willander, Sweden  
Ping Xiao, UK  
Zhi Li Xiao, USA  
Yingchao Yang, USA  
Yoke K. Yap, USA



---

Dong Kee Yi, Republic of Korea  
Jianbo Yin, China

William Yu, USA  
Michele Zappalorto, Italy

Renyun Zhang, Sweden

# Contents

## **Advanced Hybrid Functional Materials for Energy Applications**

Iftikhar Ali Sahito , Chengyu Hong , and Sung Hoon Jeong  
Editorial (2 pages), Article ID 7814784, Volume 2018 (2018)

## **Improvement of Solar Cell Characteristics Using PbS Quantum Dot Superlattice Prepared by Sedimentation**

Kohki Mukai  and Yoshikazu Ishida  
Research Article (6 pages), Article ID 3617687, Volume 2018 (2018)

## **Stabilization of Electrospun PAN/Gelatin Nanofiber Mats for Carbonization**

Lilia Sabantina, Daria Wehlage, Michaela Klöcker, Al Mamun, Timo Grothe, Francisco José García-Mateos, José Rodríguez-Mirasol, Tomás Cordero, Karin Finsterbusch, and Andrea Ehrmann   
Research Article (12 pages), Article ID 6131085, Volume 2018 (2018)

## **Opto-Electrical Properties of Composite Materials Based on Two Benzotrithiophene Copolymers and Fullerene Derivatives**

N. Radychev , M. L. Keshotov, H. Borchert, Y. Bondarchuk, S. A. Kuklin, A. Korotaeva, Z. Xie, D. Godovsky, A. R. Khokhlov, and J. Parisi  
Research Article (9 pages), Article ID 4561320, Volume 2018 (2018)

## **Study on the Phase Change Characteristics of Carbon-Based Nanofluids**

Tun-Ping Teng , Shang-Pang Yu , Ting-Chiang Hsiao, and Chun-Chi Chung  
Research Article (12 pages), Article ID 8230120, Volume 2018 (2018)

## **Hole Transport Behaviour of Various Polymers and Their Application to Perovskite-Sensitized Solid-State Solar Cells**

Jeongmin Lim, Seong Young Kong, and Yong Ju Yun   
Research Article (6 pages), Article ID 7545914, Volume 2018 (2018)

## **Self-Ordered Voids Formation in SiO<sub>2</sub> Matrix by Ge Outdiffusion**

B. Pivac , P. Dubček, J. Dasović, H. Zorc, S. Bernstorff , J. Zavašnik, and B. Vlahovic  
Research Article (8 pages), Article ID 9326408, Volume 2018 (2018)

## Editorial

# Advanced Hybrid Functional Materials for Energy Applications

Iftikhar Ali Sahito <sup>1</sup>, Chengyu Hong <sup>2</sup>, and Sung Hoon Jeong<sup>3</sup>

<sup>1</sup>Department of Textile Engineering, Mehran University of Engineering and Technology, Jamshoro 76060, Pakistan

<sup>2</sup>Department of Civil Engineering, Shanghai University, Shanghai 200444, China

<sup>3</sup>Department Organic and Nano Engineering, Hanyang University, Seoul, Republic of Korea

Correspondence should be addressed to Iftikhar Ali Sahito; [iftikhar.sahito@faculty.muett.edu.pk](mailto:iftikhar.sahito@faculty.muett.edu.pk)

Received 14 October 2018; Accepted 14 October 2018; Published 30 December 2018

Copyright © 2018 Iftikhar Ali Sahito et al. This is an open access article distributed under the Creative Commons Attribution License, which permits unrestricted use, distribution, and reproduction in any medium, provided the original work is properly cited.

This special issue is intended to present and discuss recent challenges and technological advancement in development and recent research trends for the use of functional nanomaterials and their application in energy harvesting and energy storage devices and to understand the science of the recently developed functional nanomaterials for energy applications. This special issue gives an insight into the functional materials having potential application in the energy harvesting and storage including the materials used for the recently developed perovskite solar cells. A good number of papers were submitted, and after a thorough peer review process, six papers were selected to be included in this special issue.

The included papers cover important applications of nanomaterials for energy application, including in quantum dot solar cells, perovskite solar cells, optoelectrical properties of fullerene derivatives, phase change behavior of carbon derivatives, stabilization of electrospun nanofiber mats, and self-ordered void formation in silicon dioxide. We believe that the original work published in this special issue highlights the contemporary topics in research related to functional nanomaterials in energy applications and will familiarize readers to the latest advances in the field.

The paper by K. Mukai and Y. Ishida presents a significant improvement in the characteristics of organic solar cells on Si substrates using quantum dot (QD) superlattices prepared by sedimentation. They discovered that the PbS QD grains grew into a large superlattice when the deposition proceeded for a long period of time. They also revealed that when the deposition is slow, the short-circuit current density of the solar cell doubles compared with the rapid deposition case.

The paper by N. Radychev et al. presents an investigation of two donor-acceptor copolymers based in the view of photovoltaic application. They revealed that the resulting copolymers exhibit strong absorption in the visible region with a similar band gap of about 2.2 eV and applying an optimization procedure, a power conversion efficiency of 4.6% is shown to have been achieved for the PC71BM solar cells.

The paper by T.-P. Teng et al. presents a novel carbon-based nanofluids (CBNFs) with the minimized carbon materials (MCMs), prepared using a graphite-powder-based heating and cooling processing method (GP-HCPM), with improved stability. Their results revealed that the CBNFs tend to increase the thermal conductivity  $k$ , viscosity, and density values but reduce the specific heat values of the samples, compared with water.

The paper by L. Sabantina et al. presents first tests of stabilizing PAN/gelatin nanofibers, depicting the impact of different stabilization temperatures and heating rates on the chemical properties as well as the morphologies of the resulting nanofiber mats. They discovered that like the stabilization of pure PAN, a stabilization temperature of 280°C seems suitable. Also, compared to stabilization of pure PAN nanofiber mats, approximately double heating rates can be used for PAN/gelatin blends without creating undesired conglutinations.

The paper by J. Lim et al. presents  $\text{CH}_3\text{NH}_3\text{PbI}_3$  perovskite-sensitized solid state solar cells with the use of different polymer hole transport materials and showed that the device with a spiro-OMeTAD-based hole transport layer shows the highest efficiency of 6.9%. Interestingly, the

PTB7 polymer, which is considered an electron donor material, showed dominant hole transport behaviors in the perovskite solar cell.

The paper by B. Pivac et al. presents the annealing behavior of very thin SiO<sub>2</sub>/Ge multilayers deposited on Si substrate by e-gun deposition. They showed that after annealing at 800°C, in inert atmosphere, Ge is completely out-diffused from the SiO<sub>2</sub> matrix leaving small (about 3 nm) spherical voids embedded in the SiO<sub>2</sub> matrix. These voids are formed at distances governed by the preexisting multilayer structure (in vertical direction) and self-organization (in horizontal direction).

### **Conflicts of Interest**

We, the guest editorial team of the special issue, declare that we do not have any conflict of interest or private agreements with companies.

### **Acknowledgments**

We would like to thank all the authors who contributed to this special issue and the experts who gave the scientific reviews with their expertise in due time, giving us a critical and constructive feedback.

*Iftikhar Ali Sahito  
Chengyu Hong  
Sung Hoon Jeong*

## Research Article

# Improvement of Solar Cell Characteristics Using PbS Quantum Dot Superlattice Prepared by Sedimentation

Kohki Mukai  and Yoshikazu Ishida

Graduate School of Engineering, Yokohama National University, 79-5 Tokiwadai, Hodogaya-Ku, Yokohama, Kanagawa 240-8501, Japan

Correspondence should be addressed to Kohki Mukai; [mukai@ynu.ac.jp](mailto:mukai@ynu.ac.jp)

Received 23 April 2018; Revised 20 September 2018; Accepted 4 October 2018; Published 28 November 2018

Guest Editor: Sung Hoon Jeong

Copyright © 2018 Kohki Mukai and Yoshikazu Ishida. This is an open access article distributed under the Creative Commons Attribution License, which permits unrestricted use, distribution, and reproduction in any medium, provided the original work is properly cited.

We report the characteristics of organic solar cells on Si substrates using quantum dot superlattices (QDSLs) prepared by sedimentation. When colloidal quantum dots (QDs) are deposited on a substrate in a solvent, they are closely packed and form multiple grains in a film. We found that the PbS QD grains grew into a large superlattice when the deposition proceeded for a long period of time. A solar cell was fabricated using the QD superlattice film as an absorbing layer. When the deposition was slow, the short-circuit current density of the solar cell doubled compared with that of the rapid deposition case. Simulations based on the superposition model suggest that the superlattice formation process is responsible for the observed change in the cell characteristics.

## 1. Introduction

Renewable energy continues to attract attention as it reduces current environmental problems like global warming and increased energy demand. Photovoltaic power generation is one renewable energy technology. The maximum power conversion efficiency (PCE) of crystalline Si (c-Si) solar cells, which are currently mainstream, is theoretically approximately 29%. Higher PCE is required if solar cells are to meet future energy demands, requiring a technical breakthrough. The PCE limit is due to heat loss and transmission loss. Electrons and holes excited by photons with energy larger than the band gap of Si (absorption layer) relax to the band edge, releasing their energy as heat. Also, photons with energy smaller than the band gap transmit without being absorbed. It was theoretically predicted that intermediate band-type solar cells with a quantum dot superlattice (QDSL) structure can reduce these losses and yield greater than 60% PCE [1, 2]. Other researches have attempted to fabricate QDSL solar cells with Stranski-Krastanov-type quantum dots (QDs) [3–5]. However, formation of Stranski-Krastanov-type QDs is based on crystal strain; thus, it is difficult to grow QDs with

high uniformity and high density while simultaneously stacking them in three dimensions [6, 7]. On the other hand, colloidal QDs prepared by chemical synthesis are also expected to be a viable material for the organic solar cells [8, 9]. Colloidal QDs have been mixed into a photon-electron conversion material instead of dye to expand the absorption band in solar cells. In another case, colloidal QDs were used as an absorption layer in Schottky junction organic semiconductor solar cells. In organic solar cells, colloidal QD films are prepared by spin coating on a substrate, and the QDs accumulate randomly. We proposed using a superlattice of colloidal QDs in solar cells [10–12]. It is known that, after the evaporation of a solvent, colloidal QDs self-assemble and pack densely in the area with electron-microscopic order [13–17]. The structure functions as a polycrystalline structure in which small single-crystal regions are connected via amorphous regions. We found that the very slow QD sedimentation in a solvent enlarged each single crystalline area in the polycrystalline structure [18]. The single-crystal region can be regarded as a superlattice. By forming a film with a wide QDSL, the absorption band is broadened and the average carrier mobility increases by the generated intermediate

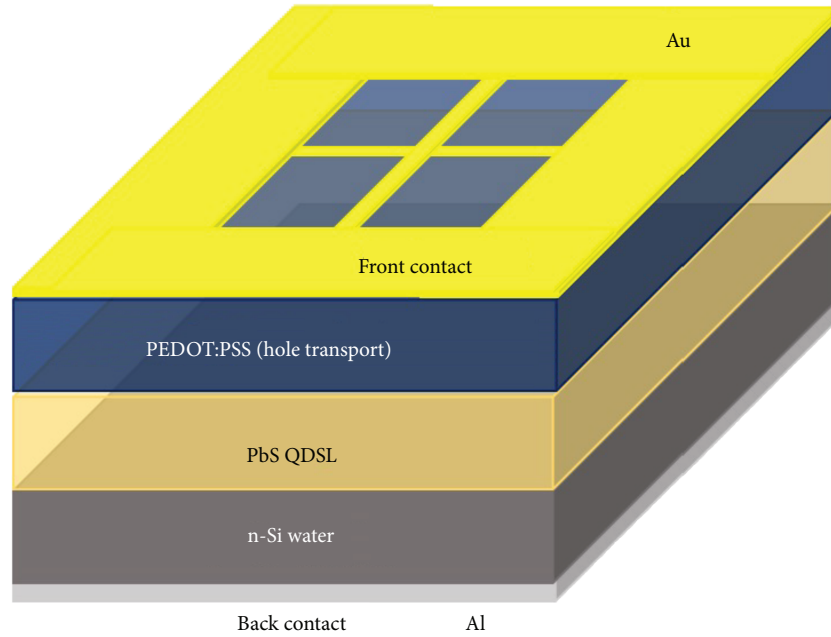


FIGURE 1: Schematic of QD solar cell structure.

band. In this work, we investigated the characteristics of an organic solar cell using PbS QDSL taking into account the sedimentation speed of QDs during QDSL formation.

## 2. Experimental

QD solar cells were fabricated using organic materials on a Si substrate. Figure 1 schematically shows the structure of the fabricated solar cell. After removing organic contamination with piranha solution, washing with buffered HF solution was applied to the n-type (100) c-Si substrate, which was a recycled product (resistivity was 1–10  $\Omega\cdot\text{cm}$ ). Commercially available PbS QDs were used in our device (EviDot, Evident Thermoelectrics Inc.). The sedimentation time of colloidal QDs was adjusted by changing the evaporation speed of the solvent by controlling the atmospheric vapor pressure. Rapid sedimentation was carried out by leaving QD droplets on the Si substrate dry in a nitrogen gas atmosphere. Slow sedimentation occurred by setting the sample in a sealed container with a reservoir of solvent. It has been confirmed in previous studies that free QDs precipitate in a solvent to the substrate over a period of several days [4]. The thickness of the QD layer ranged from several microns to 20 microns. Thereafter, the QD layer was covered with a 40 nm thick poly(3,4-ethylenedioxythiophene) polystyrene sulfonate (PEDOT:PSS) hole transport layer, which was mixed with 5 wt% dimethyl sulfoxide to improve the electric conductivity [19]. The mixture was spin-coated on the QDSL layer at 6000 rpm for 2 minutes and was subsequently annealed for 15 minutes. An aluminum electrode was deposited on the back Si surface, and a cross-shaped gold electrode was deposited on the hole transport layer by vapor deposition.

The QD layers were examined with scanning electron microscopy (SEM) and photoluminescence (PL) measurements. PL at room temperature was evaluated using a

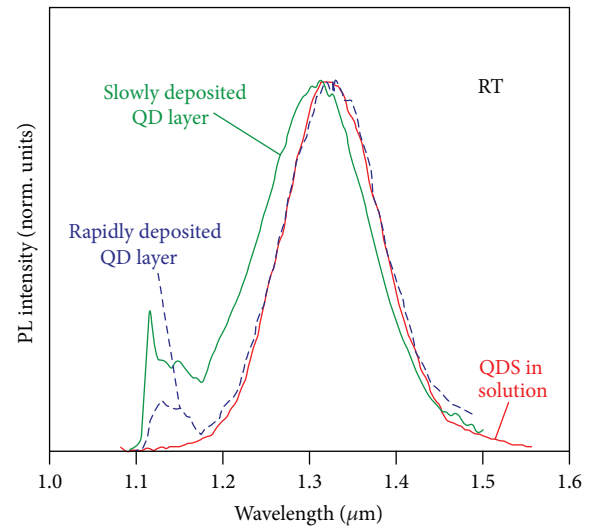


FIGURE 2: Photoluminescence spectra from the colloidal PbS QDs at room temperature.

670 nm diode laser with a monochromator (Jobin Yvon, HR320) and lock-in amplifier (Seiko EG&G Corp., 5210). The PL spectra are shown in Figure 2. Properties of QDs in solution and QD layers were compared. We can see that the QDs have a band gap in the infrared region and will be the complement to the absorption of Si in the solar cell. Evaluation of the solar cell characteristics was conducted with a lab-made apparatus. A conventional variable-illuminance halogen lamp was used as the light source. The irradiation intensity was calibrated using a solar power meter (AS ONE Corp., ST530) and standard Si solar cell. The change in the current with respect to the voltage of the solar cell was evaluated using a measurement power supply (Advantest

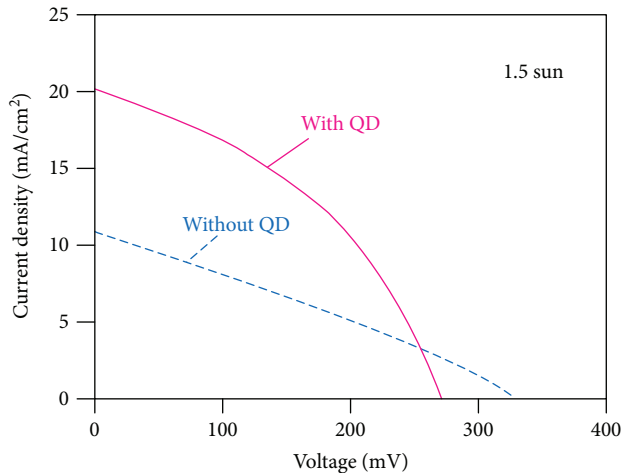


FIGURE 3: Current-voltage characteristics of solar cells. Devices with and without a QD layer are compared.

Corp., TR6134), which was controlled via UBS with a self-built VBA macro in Microsoft Excel.

### 3. Results and Discussion

The current-voltage characteristics of the fabricated QD solar cell at 1.5 suns are shown in Figure 3. A solar cell without the QD layer was prepared and its characteristics were investigated for comparison. The QD layer was formed after several minutes of solvent evaporation from the QD solution. The short-circuit current density improved from 10.4 mA/cm<sup>2</sup> to 20.1 mA/cm<sup>2</sup> after introducing the QD layer. This could occur due to a broadened absorption band in the cell. The solar cell without the QD layer was inferior to a general Si cell. This is probably because the Si substrate we used was a recycled one. PCE increased by a factor of 1.5 (0.92 to 1.42%) after incorporation of the QD layer, although the open-circuit voltage decreased slightly. The filling factor (FF) was 38% and 27% with and without QDs, respectively.

The QD sedimentation time was controlled while fabricating the QD layers. When depositing QDs slowly, free QDs have enough time to reach a stable position in the solvent and, as a result, the size of the densely packed single-crystal region is expected to grow. When the solvent evaporates rapidly, QDs accumulate on the surface of the descending solvent and adhere to the substrate. Figure 4 shows SEM images of the surface of the QD layer deposited for several minutes and that for over 3 days. A random pattern formed on the surface after rapid sedimentation. In the case of slow sedimentation, many clear steps can be seen on the surface. The step structure suggests that QDs were periodically arranged in an area of several hundred square microns. We saw that the wide QDSLs formed in the QD layer after depositing QDs for a long period of time. The PL characteristics also suggest that the unique structure appeared due to slow sedimentation. In Figure 2, one can see that the emission peak from the QD layer shifted slightly towards shorter wavelengths due to slow sedimentation. In addition, the emission intensity at short wavelengths increased and the spectrum

became asymmetric. We deduced that quantum confinement in QDs was weakened due to the formation of intermediate bands in some areas of the QD layer.

Figure 5(a) shows the current-voltage characteristics of the QD solar cell fabricated using rapid and slow deposition at 1 sun. There was almost no difference in the open-circuit voltage between the two deposition times, but the short-circuit current density nearly doubled when QD layers were deposited slowly. As a result, the PCE more than doubled when the QD layers were deposited slowly. Slow deposition caused the FF to increase by approximately a factor 1.5 times. As the irradiation power increased in a solar cell, the short-circuit current density increased. The increase was greater in the solar cell with the QD layer prepared by slow sedimentation. This may be due to the better performance of QDSLs. Comparing the results for rapid sedimentation in Figures 3 and 5(a), it seems that stronger excitation intensity leads to a lower open-circuit voltage. This is because the cells used in the measurement were different. In particular, the reproducibility of the cell performance was not good when sedimentation was rapid. The thickness of the QD layer was somewhat different, and the problem might degrade the quality of the interface between the QD layer and the hole transport layer.

The QD layer fabricated by sedimentation improved the solar cell performances. Since an improved current was observed, the measured current-voltage data from the QD solar cells were compared with simulation results from the standard superposition model [20]. The current density in the superposition model is defined as follows:

$$J = J_{SC} - J_0 \left[ \exp \left( \frac{eV}{kT} \right) - 1 \right], \quad (1)$$

where  $J_{SC}$  is the saturation current density and  $J_0$  is the reverse saturation current density. The reverse saturation current is due to the minority carriers at the depletion layer edge and at the  $i$  region by thermal excitation. During the calculation, we used the measured  $J_{SC}$  value with  $J_0$  as a fitting parameter. The simulation results are shown in Figure 5(b). The experimental results were reproduced very well, i.e., improvements of short-circuit current density, PCE, and FF were explained by the model. The values used were  $J_0 = 2.5$  mA/cm<sup>2</sup> for slow deposition and  $J_0 = 1.3$  mA/cm<sup>2</sup> for rapid deposition. These values of  $J_0$  are very large. The most likely reason for this is that more minority carriers were generated at the depletion layer edge. Considering that the Si substrate we used was a recycled product, we cannot deny the potential adverse effects of the Si substrate. The poor results from the solar cell without QDs support this speculation. Since two types of QD cells suffer from the same performance deterioration due to the fabrication process, there must be a reason why  $J_0$  was larger in the case of slow deposition. A possible reason for the large  $J_0$  value is that minority carriers in the QDSL layer increased due to the formation of intermediate bands. It has been suggested that a wide QDSL, i.e., a broad intermediate band, formed during slow sedimentation. The intermediate band in the

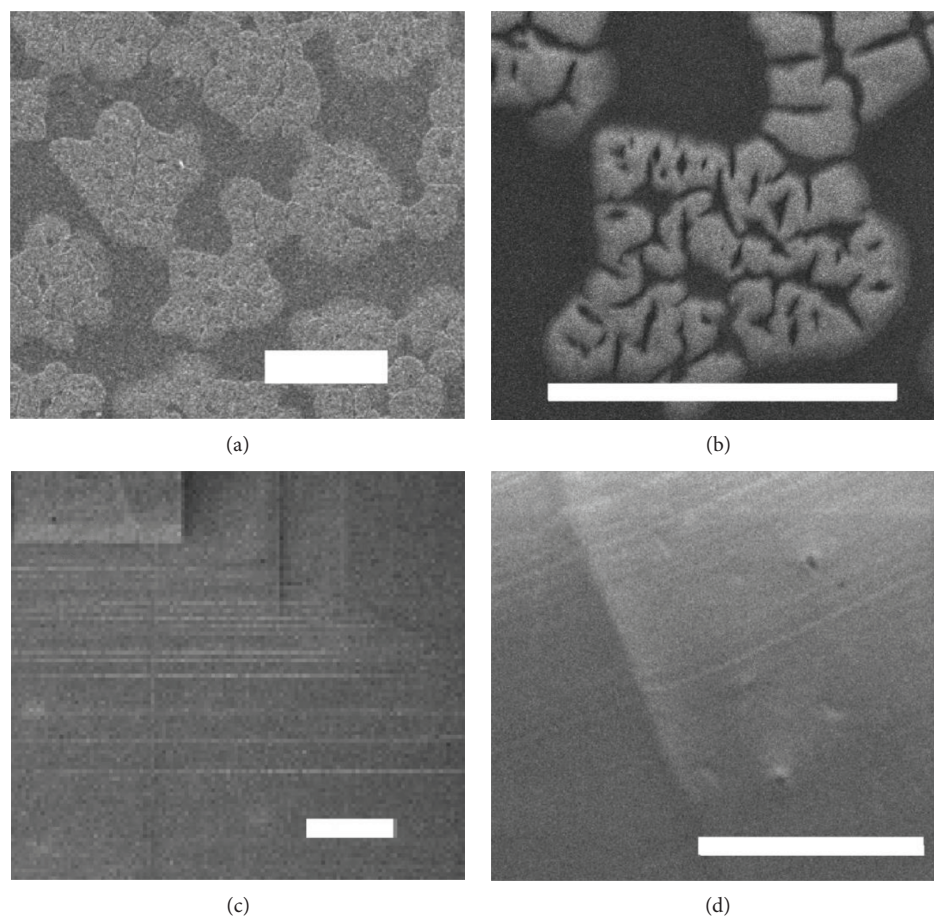


FIGURE 4: SEM images of the QD layer surfaces. (a, b) QD sedimentation time of several minutes and (c, d) sedimentation time greater than 3 days. Scale bars are 100  $\mu\text{m}$ .

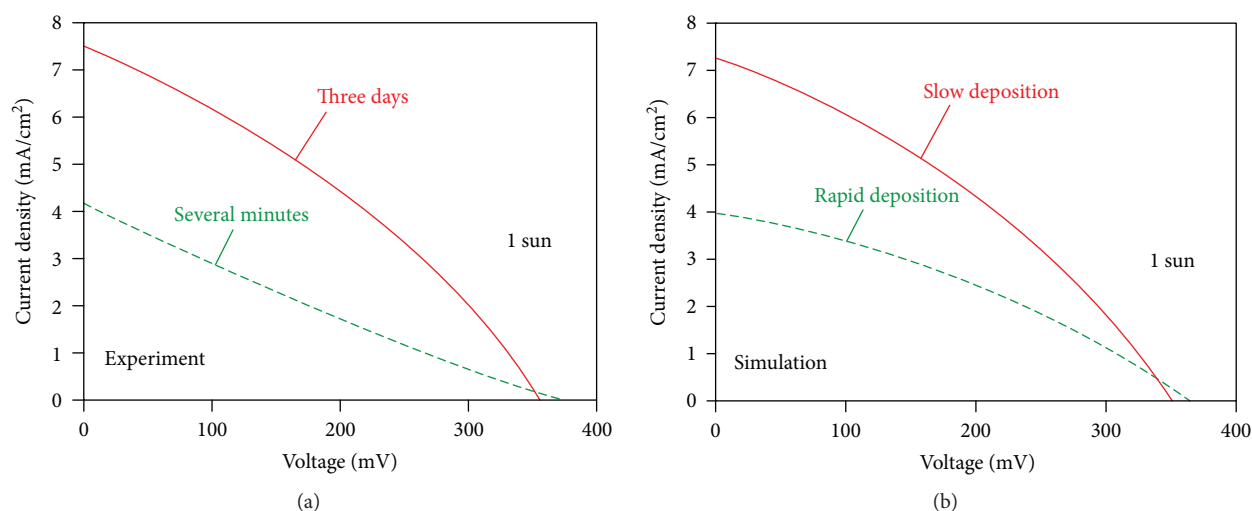


FIGURE 5: (a) Experimental current-voltage data from QD solar cells. Devices with QDs deposited over 3 days and those with QDs deposited for 20 minutes are compared. (b) Simulated current-voltage characteristics in QD solar cells.

infrared region will increase the number of minority carriers due to thermal excitation. The carrier mobility may have also improved in the intermediate band. As a result, the generated minority carriers can reach the electrode more easily, thus increasing the reverse saturation current.

It is also conceivable that  $J_0$  was apparently large due to the cell resistance values. The cell resistance was calculated from the current-voltage data in Figure 5(a). In the case of rapid sedimentation, the series and parallel resistance values were 114 and 79  $\Omega\text{-cm}^2$ , respectively. In the case of slow

sedimentation, they were 29 and 83  $\Omega\text{-cm}^2$ , respectively. The series resistance was very high in the case of rapid sedimentation, and in both cases, the parallel resistance was about one order of magnitude lower than the common value. The series resistance is the sum of various electric resistance sources encountered in the course of carrier transport. For holes, the contributing series resistances are the resistance of the QD layer, the resistance during lateral transport in the p-type layer, and the contact resistance between the electrode and the hole transport layer. Carrier scattering at the uneven PEDOT:PSS/QD layer interface is also presumed to be the cause of series resistance, and one can infer that scattering was more likely to occur in the case of rapid sedimentation. The sedimentation speed likely affects the resistance in the QD layer. For electrons, the resistance in the QD layer and Si substrate and the contact resistance at the back electrode contribute to series resistance. Among them, only the resistance in the QD layer may be influenced by sedimentation speed. Parallel resistance is a component of the leakage current. The parallel resistance is low when insulation between the positive and the negative electrodes is poor. Impurities and defects in the absorption layer lower the parallel resistance, and our cell may have problems in this respect. In particular, the PEDOT:PSS/QD layer interface and the QD layer/n-Si interface were exposed to air during fabrication, and this possibly caused contamination and/or chemical degradation.

It has been shown that QDSLs improved the characteristics of our solar cells. Our QDSL solar cells had three major problems that should be solved in order to further improve their properties. The most effective and immediate way would be to use a solar grade or better Si substrate. Another problem to be solved is control over the thickness of the QDSL layer. First, thickness should be reduced to a few microns or less. It is expected that many carrier recombination events occur since the QDSL layer was too thick to extract carriers before recombination. Also, the nonuniformity of the QDSL film should be improved. By reducing the area of the interface, deterioration in the cell fabrication process will be suppressed during atmospheric exposure. In order to improve the flatness of the film, it is necessary to homogenize the QD solution and to control the affinity between the solution and the substrate. The third point to be improved is the quality of the QDSL itself. By exchanging the QD ligand for a shorter one, the carrier transport property will be further improved [11, 12] and the number of intermediate bands will increase [21]. One would expect that carrier transport would be improved further by matching the crystal orientation of individual QDs. The aligned direction of the wave functions in a QD results in strong coupling between QDs. It has been reported that interactions between QD facets occur during sedimentation in a solvent, thus forming a so-called perfect superlattice from the colloidal QDs [21, 22].

#### 4. Conclusions

We have reported an improved organic solar cell on a Si substrate by using a PbS QDSL prepared by sedimentation.

The short-circuit current density in the solar cell with a QD layer was higher than that without a QD layer. When the QD layer was prepared via slow sedimentation, the short-circuit current density nearly doubled compared to the case of rapid sedimentation. SEM images indicate that a wide QDSL formed when QDs were deposited for a period of time longer than three days. The simulated current-voltage characteristics helped illustrate measures that could further improve the properties of the QDSL solar cells.

#### Data Availability

The data used to support the findings of this study are included within the article.

#### Disclosure

The basis of this study was reported in the 65th JSPS Spring Meeting, 2018 (in Japanese).

#### Conflicts of Interest

The authors declare that they have no conflicts of interest.

#### Acknowledgments

This research was supported by the Canon Foundation for Creation of Industrial Infrastructure Research Grant Program, the Nohmura Foundation for Membrane Structure's Technology, and the Iwatani Naoji Foundation.

#### References

- [1] T. Nozawa and Y. Arakawa, "Detailed balance limit of the efficiency of multilevel intermediate band solar cells," *Applied Physics Letters*, vol. 98, no. 17, article 171108, 2011.
- [2] X. Yang, K. Wang, Y. Gu et al., "Improved efficiency of InAs/GaAs quantum dots solar cells by Si-doping," *Solar Energy Materials & Solar Cells*, vol. 113, pp. 144–147, 2013.
- [3] N. Ahsan, N. Miyashita, M. M. Islam, K. M. Yu, W. Walukiewicz, and Y. Okada, "Two-photon excitation in an intermediate band solar cell structure," *Applied Physics Letters*, vol. 100, no. 17, article 172111, 2012.
- [4] A. Luque and A. Marti, "Increasing the efficiency of ideal solar cells by photon induced transitions at intermediate levels," *Physical Review Letters*, vol. 78, no. 26, pp. 5014–5017, 1997.
- [5] V. Popescu, G. Bester, M. C. Hanna, A. G. Norman, and A. Zunger, "Theoretical and experimental examination of the intermediate-band concept for strain-balanced (In,Ga)As/Ga(As,P) quantum dot solar cells," *Physical Review B*, vol. 78, no. 20, article 205321, 2008.
- [6] A. Marti, N. Lopez, E. Antolin et al., "Emitter degradation in quantum dot intermediate band solar cells," *Applied Physics Letters*, vol. 90, no. 23, article 233510, 2007.
- [7] T. Sogabe, Y. Shoji, M. Ohba et al., "Intermediate-band dynamics of quantum dots solar cell in concentrator photovoltaic modules," *Scientific Reports*, vol. 4, article 4792, 2014.
- [8] A. G. Pattantyus-Abraham, I. J. Kramer, A. R. Barkhouse et al., "Depleted-heterojunction colloidal quantum dot solar cells," *ACS Nano*, vol. 4, no. 6, pp. 3374–3380, 2010.

- [9] Z. Jin, M. Yuan, H. Li et al., “Graphdiyne: an efficient hole transporter for stable high-performance colloidal quantum dot solar cells,” *Advanced Functional Materials*, vol. 26, no. 29, pp. 5284–5289, 2016.
- [10] K. Mukai, A. Hirota, Y. Shimizu, and S. Nakashima, “Template method for nano-order positioning and dense packing of quantum dots for optoelectronic device application,” *Semiconductor Science and Technology*, vol. 30, no. 4, article 044006, 2015.
- [11] K. Mukai, F. Suetsugu, and K. Niwa, “Controlling the electron coupled state in the superlattice of PbS quantum dots by replacing ligands,” *IEEE Transactions on Nanotechnology*, vol. 16, no. 4, pp. 600–605, 2017.
- [12] K. Mukai, F. Suetsugu, and K. Niwa, “Large red shift of emission of PbS quantum-dot superlattice with butylamine ligands,” *Current Nanoscience*, vol. 13, no. 6, p. 574, 2017.
- [13] L. Cademartiri, J. Bertolotti, R. Sapienza, D. S. Wiersma, G. Freymann, and A. Ozin, “Multigram scale, solventless, and diffusion-controlled route to highly monodisperse PbS nanocrystals,” *The Journal of Physical Chemistry B*, vol. 110, no. 2, pp. 671–673, 2006.
- [14] C. B. Murray, C. R. Kagan, and M. G. Bawendi, “Self-organization of CdSe nanocrystallites into three-dimensional quantum dot superlattices,” *Science*, vol. 270, no. 5240, pp. 1335–1338, 1995.
- [15] R. Li, K. Bian, T. Hanrath, W. A. Bassett, and Z. Wang, “Decoding the superlattice and interface structure of truncate PbS nanocrystal-assembled supercrystal and associated interaction forces,” *Journal of the American Chemical Society*, vol. 136, no. 34, pp. 12047–12055, 2014.
- [16] W. V. D. Stam, A. P. Gantapara, Q. A. Akkerman et al., “Self-assembly of colloidal hexagonal bipyramid- and bifrustum-shaped ZnS nanocrystals into two-dimensional superstructures,” *Nano Letters*, vol. 14, no. 2, pp. 1032–1037, 2014.
- [17] J. M. Luther, M. Law, Q. Song, C. L. Perkins, M. C. Beard, and A. J. Nozik, “Structural, optical, and electrical properties of self-assembled films of PbSe nanocrystals treated with 1,2-ethanedithiol,” *ACS Nano*, vol. 2, no. 2, pp. 271–280, 2008.
- [18] Y. Shimizu, I. Morimoto, S. Nakashima, and K. Mukai, “Dense packing of colloidal quantum dots on patterned substrate,” in *26th International Microprocesses and Nanotechnology Conference (MNC2013)*, Hokkaido, Japan, November 2013.
- [19] M. Pietsch, S. Jäckle, and S. Christiansen, “Interface investigation of planar hybrid n-Si/PEDOT:PSS solar cells with open circuit voltages up to 645 mV and efficiencies of 12.6%,” *Applied Physics A*, vol. 115, no. 4, pp. 1109–1113, 2014.
- [20] V. Aroutiounian, S. Petrosyan, and A. Khachatryan, “Quantum dot solar cells,” *Journal of Applied Physics*, vol. 89, no. 4, pp. 2268–2271, 2001.
- [21] C. R. Kagan and C. B. Murray, “Charge transport in strongly coupled quantum dot solids,” *Nature Nanotechnology*, vol. 10, no. 12, pp. 1013–1026, 2015.
- [22] K. Mukai, S. Fujimoto, and F. Suetsugu, “Formation of superlattice with aligned plane orientation of colloidal PbS quantum dots,” *Japanese Journal of Applied Physics*, vol. 57, no. 4S, article 04FS02, 2018.

## Research Article

# Stabilization of Electrospun PAN/Gelatin Nanofiber Mats for Carbonization

**Lilia Sabantina,<sup>1,2</sup> Daria Wehlage,<sup>1</sup> Michaela Klöcker,<sup>1</sup> Al Mamun,<sup>3</sup> Timo Grothe,<sup>1</sup> Francisco José García-Mateos,<sup>2</sup> José Rodríguez-Mirasol,<sup>2</sup> Tomás Cordero,<sup>2</sup> Karin Finsterbusch,<sup>3</sup> and Andrea Ehrmann<sup>1</sup>**

<sup>1</sup>Bielefeld University of Applied Sciences, Faculty of Engineering and Mathematics, Bielefeld, Germany

<sup>2</sup>Universidad de Málaga, Andalucía Tech, Dpto. de Ingeniería Química, Málaga, Spain

<sup>3</sup>Niederrhein University of Applied Sciences, Mönchengladbach, Germany

Correspondence should be addressed to Andrea Ehrmann; [andrea.ehrmann@fh-bielefeld.de](mailto:andrea.ehrmann@fh-bielefeld.de)

Received 18 April 2018; Accepted 30 August 2018; Published 21 October 2018

Academic Editor: Sung Hoon Jeong

Copyright © 2018 Lilia Sabantina et al. This is an open access article distributed under the Creative Commons Attribution License, which permits unrestricted use, distribution, and reproduction in any medium, provided the original work is properly cited.

Due to their electrical and mechanical properties, carbon nanofibers are of large interest for diverse applications, from batteries to solar cells to filters. They can be produced by electrospinning polyacrylonitrile (PAN), stabilizing the gained nanofiber mats, and afterwards, carbonizing them in inert gas. The electrospun base material and the stabilization process are crucial for the results of the carbonization process, defining the whole fiber morphology. While blending PAN with gelatin to gain highly porous nanofibers has been reported a few times in the literature, no attempts have been made yet to stabilize and carbonize these fibers. This paper reports on the first tests of stabilizing PAN/gelatin nanofibers, depicting the impact of different stabilization temperatures and heating rates on the chemical properties as well as the morphologies of the resulting nanofiber mats. Similar to stabilization of pure PAN, a stabilization temperature of 280°C seems suitable, while the heating rate does not significantly influence the chemical properties. Compared to stabilization of pure PAN nanofiber mats, approximately doubled heating rates can be used for PAN/gelatin blends without creating undesired conglutinations, making this base material more suitable for industrial processes.

## 1. Introduction

Functional nanofibers are used in a broad variety of applications, from nanofibrous membranes for filters [1] to substrates in tissue engineering [2, 3] to electrocatalysis [4], capacitors [5], and other applications based on the conductivity of the nanofibers [6]. Especially for batteries and other energy applications, often carbon nanofibers are used [7–11].

Such carbon nanofibers are often prepared via the electrospinning route, followed by stabilization and afterwards carbonization. Both steps influence the morphologies, the mechanical and electrical properties of the final carbon nanofibers significantly. While carbon nanofibers can be produced from a broad variety of materials [12–14], one of the most common materials for this purpose is polyacrylonitrile (PAN). PAN changes fiber diameters and mat

morphologies significantly for varying spinning and solution parameters [15, 16], while the fibers themselves keep their flat, even surfaces.

In most applications, however, it is advantageous to further increase the surface: volume ratio of the nanofibers. This can be done by blending PAN with other polymers or inorganic material, a method which may also alter other physical properties, such as the conductivity. Increased crystallinity and conductivity were found, e.g., when PAN/pitch nanofibers were carbonized [17]. Blending PAN with cellulose acetate resulted in increased adsorption properties of the carbonized nanofibers [18]. Combined with diverse water-soluble polymers, only gelatin showed a significant influence on the PAN fiber diameters [19]. PAN/gelatin blends have also shown to create highly porous fibers by electrospinning [20]. Nevertheless, to the best of our knowledge,

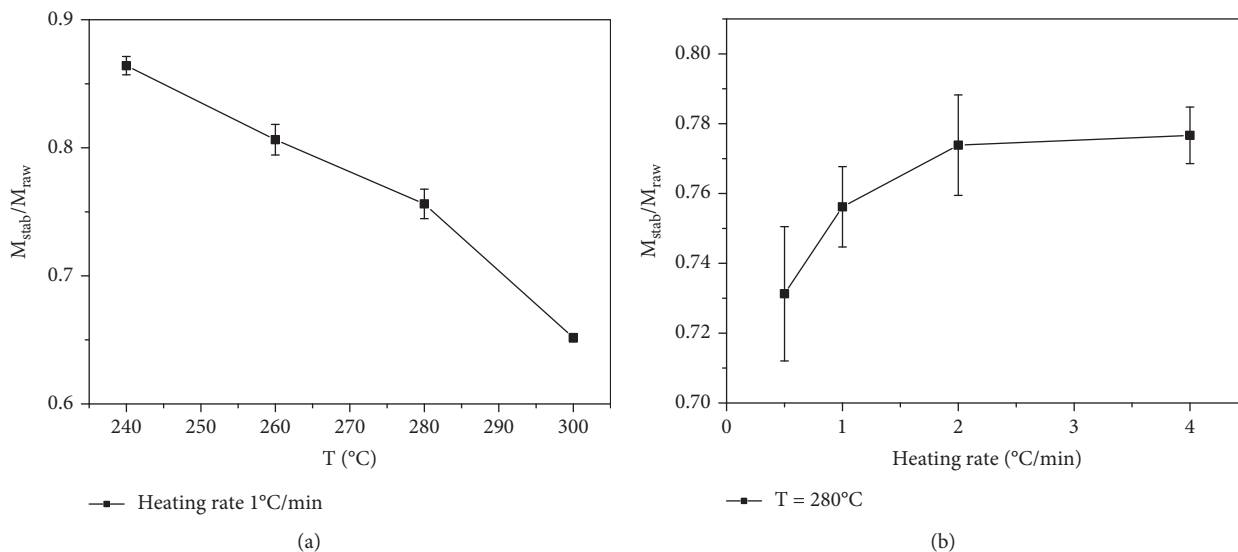


FIGURE 1: Normalized masses after stabilization at different temperatures (a) and using different heating rates (b).

no investigations on the stabilization of such electrospun PAN/gelatin nanofiber mats were performed yet.

In this paper, we report on the influence of the stabilization temperatures and heating rates on the chemical properties and morphologies of the resulting nanofiber mats.

## 2. Materials and Methods

Electrospinning was performed with a “Nanospider Lab” (Elmarco, Czech Republic), a needleless electrospinning machine based on the wire technology, using a polypropylene fiber mat as the substrate. The spinning parameters were high voltage 70 kV, nozzle diameter 1.5 mm, carriage speed 100 mm/s, ground-substrate distance 240 mm, electrode-substrate distance 50 mm, temperature in chamber 22°C, and relative humidity in chamber 33%.

The spinning solution contained 16% PAN in DMSO (min 99.9%, purchased from S3 Chemicals, Germany) and 9% gelatin (Abtei, Germany).

Samples of 50 mm × 50 mm of the electrospun nanofiber mats were stabilized in a muffle furnace B150 (Nabertherm), approaching stabilization temperatures between 240°C and 300°C at heating rates between 0.5°C/min and 4°C/min, and then 1 h of isothermal treatment at the final temperature. For each combination of heating rate and temperature, samples were stabilized with their borders fixed by placing a metal frame with sufficient weight on them as well as freely, without any fixation. Carbonization was performed in a furnace CTF 12/TZF 12 (Carbolite Gero Ltd., Hope, UK), approaching a temperature of 800°C with a heating rate of 10°C/min in a nitrogen flow of 150 mL/min (STP), followed by isothermal treatment for 1 h.

Masses of the samples were taken before and after stabilization using an analytical balance (VWR). Samples dimensions were analyzed by the program ImageJ 1.51j8.

For Fourier-transform infrared (FTIR) spectroscopy, an Excalibur 3100 (Varian, Inc.) was used. Color measurements were performed with a sph900 spectrometer (ColorLite).

Scanning electron microscopy (SEM) images were taken by a Zeiss 1450VPSE with a resolution of 5 nm or a JSM-840 microscope, respectively, using a nominal magnification of 5000x. Optical images of the nanofiber mats were taken using a confocal laser scanning microscope (CLSM) VK-100 with a nominal magnification of 2000x.

## 3. Results and Discussion

Figure 1 depicts the relative mass changes for different stabilization temperatures (Figure 1(a)) and different heating rates (Figure 1(b)), respectively. The trend of smaller normalized masses, i.e., larger losses, for higher stabilization temperatures is clearly visible. Compared to a previous study on pure PAN nanofiber mats, the normalized masses here are generally smaller, and the mass loss is strongly increased for higher temperatures. This indicates clearly the influence of the gelatin in the fibers—since gelatin denaturalizes around 40–90°C, depending on the water content [21], and it can be expected to be released from the nanofibers as long as it is not completely embedded in the fiber.

Opposite to mass measurements on stabilized PAN nanofibers, showing an approximately constant value of ~85% of the original mass, here, a clear heating rate dependence is visible for the lower heating rates. This suggests that here the duration of the heating time plays an important role, i.e., the lower the heating rate, the higher the polymer decomposition obtained due to pyrolysis and recombination reactions.

Besides the masses, the areas of the stabilized samples in fixed and unfixed states were measured. The results are depicted in Figure 2, depending on the temperature (Figure 2(a)) and the heating rate (Figure 2(b)), respectively. The ratio of the areas of the unfixed and the fixed samples decreases with increasing temperature as well as with increasing heating rate, showing that high temperatures and large heating rates cause more stress in the unfixed samples and let them crumple stronger than under less extreme

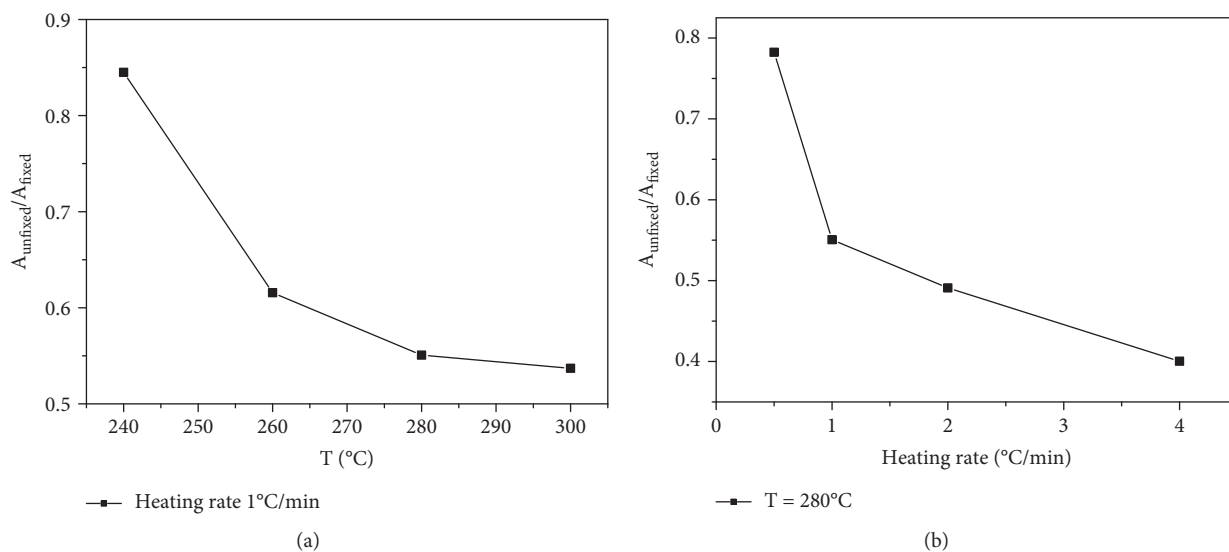


FIGURE 2: Normalized areas after stabilization at different temperatures (a) and using different heating rates (b).

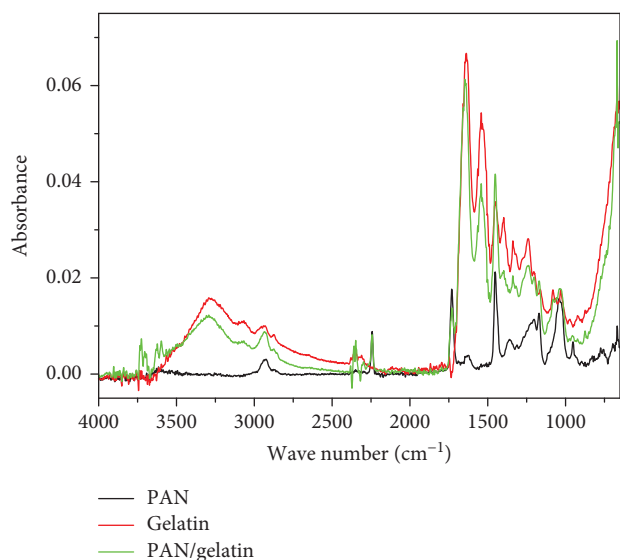


FIGURE 3: FTIR measurements on PAN, gelatin, and PAN/gelatin nanofiber mats.

conditions. This finding underlines the importance of fixing the samples during stabilization.

FTIR measurements were performed on the PAN/gelatin nanofiber mat before stabilization. Figure 3 shows the result together with pure PAN and pure gelatin nanofiber mats. Comparing the spectra shows that the PAN/gelatin line is composed of the typical PAN peaks in the range between 950 cm<sup>-1</sup> and 1700 cm<sup>-1</sup>, at 2240 cm<sup>-1</sup> and 2938 cm<sup>-1</sup> [22, 23] as well as gelatin peaks. The latter can be differentiated into the region around 2700–3600 cm<sup>-1</sup> which is attributed to the amides A and B, the region around 900–1900 cm<sup>-1</sup> showing the amides I, II, and III, and finally the region below 900 cm<sup>-1</sup> depicting amide IV [24]. It should be mentioned that several peaks are hard to distinguish between pure PAN and pure gelatin. The most prominent

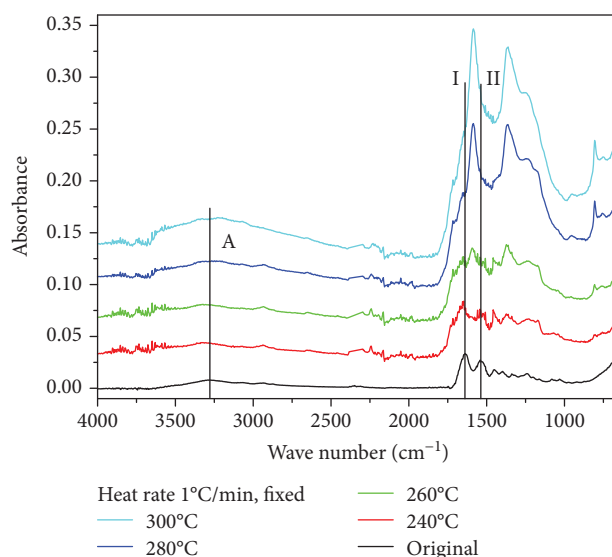


FIGURE 4: FTIR absorbance measurements on fixed samples, stabilized at different temperatures approached with 1°C/min. The lines are offset vertically for clarity.

peaks which are not existent in pure PAN are the peak around 3400 cm<sup>-1</sup>, corresponding with amide A, and the peak near 700 cm<sup>-1</sup>, corresponding to amide IV. In the original state after electrospinning, there are also clear differences between PAN and gelatin around 1640 cm<sup>-1</sup> (amide I) and 1540 cm<sup>-1</sup> (amide II); however, it is well known that in this region, significant changes will occur during the stabilization process, making these peaks possibly less suitable for the examination whether gelatin stays in the fabric during stabilization.

A comparison of the FTIR measurements on PAN/gelatin samples, heated at 1°C/min to different stabilization temperatures, is given in Figure 4. At first glance, the results look very similar to those gained by stabilizing pure PAN

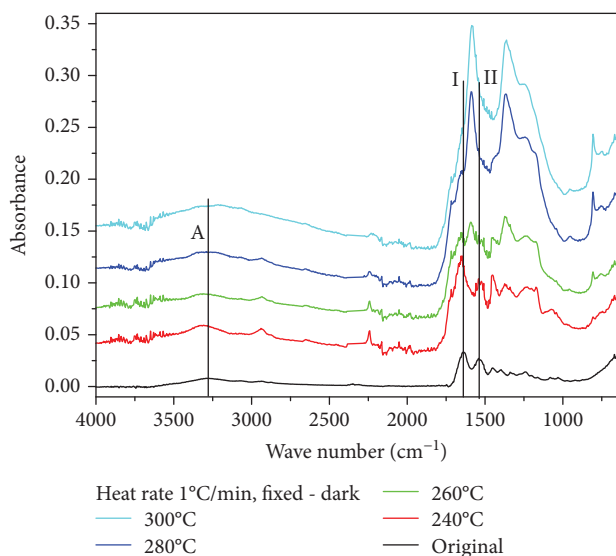


FIGURE 5: FTIR absorbance measurements on the dark areas on the back of fixed samples, stabilized at different temperatures approached with 1°C/min. The lines are offset vertically for clarity.

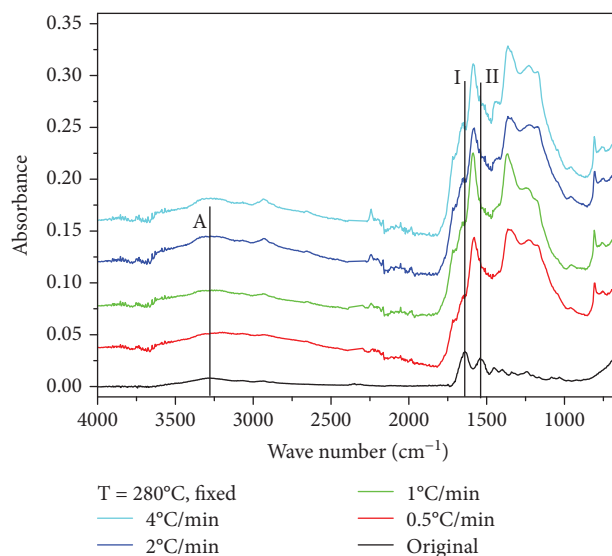


FIGURE 6: FTIR absorbance measurements on the dark areas on the back of fixed samples, stabilized at 280°C, approached with different heating rates. The lines are offset vertically for clarity.

nanofiber mats [23, 24]. Following the most prominent peaks of the original PAN/gelatin peaks shows that during stabilization (amides A, I, and II, as marked in Figure 4), there is no evidence for residual gelatin in the stabilized fiber mat. The same results are visible for the not fixed samples.

Optical examination of the samples after taking them out of the muffle oven revealed dark, nearly black areas on the back in the areas which had touched the underground during stabilization. Since the gelatin is no longer visible in the FTIR measurements taken on the upper surface of the samples, it can be assumed that gelatin—which decomposes above approx. 100°C but needs more than approx. 500°C for complete combustion—has precipitated here after melting. Figure 5 thus depicts FTIR scans of these dark areas.

While for a stabilization temperature of 240°C, the peaks for amides A and I are still clearly visible, they are superposed by the growing PAN stabilization peaks for higher temperatures. Thus, the FTIR results can in this case not clearly state which material causes the black areas on the back.

Figure 6 shows the heating rate dependence of PAN/gelatin nanofiber mats, stabilized at 280°C. While stabilizing pure PAN revealed significant differences in the FTIR measurements for different heating rates [25], here, all curves are very similar. A closer look, however, shows that for higher heating rates, the peaks for the amides A, I, and II stay visible, although strongly superposed by the large peaks of the stabilized PAN in these areas. This indicates that faster heating allows the gelatin to stay in the nanofiber mat to a certain amount. Similar results were found on the dark back of these samples (not shown here).

Optical investigations were performed, using a CLSM. Figure 7 depicts a comparison of an original PAN/gelatin nanofiber mat (Figure 7(a)) and a sample stabilized in fixed position at 280°C, approached at 1°C/min (Figure 7(b)).

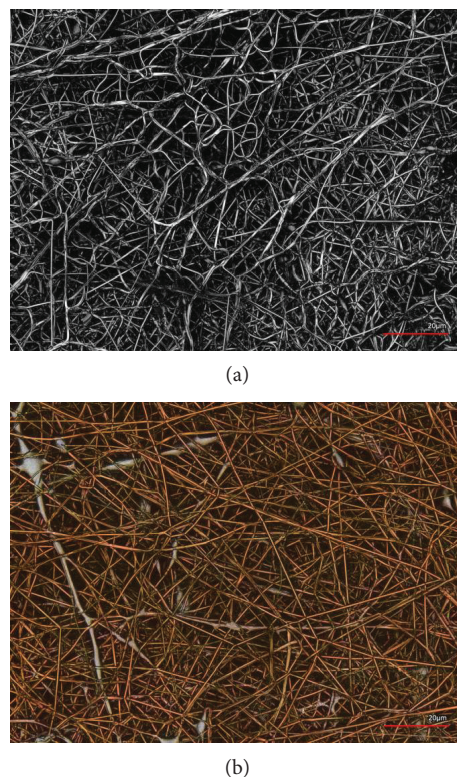


FIGURE 7: CLSM images of an untreated PAN/gelatin nanofiber mat (a) and a sample stabilized at 280°C, approached at 1°C/min (b). The scale bars indicate 20  $\mu\text{m}$ .

Firstly, both images show the typical relatively thick and straight fibers which are typical for gelatin or PAN/gelatin [19]. After stabilization, the usual brown color of the stabilized PAN is visible. Here, however, some silvery fibers can be recognized, clearly indicating gelatin. It should be

TABLE 1: CLSM images of PAN/gelatin nanofiber mat, stabilized in fixed (left panels) and unfixed state (right panels) at different temperatures, approached with 1°C/min. For a better overview, the scale bars here indicate 50 μm.

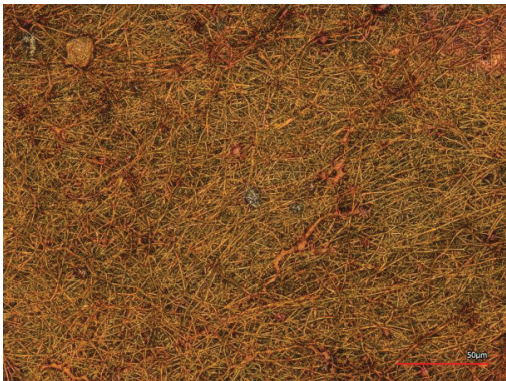
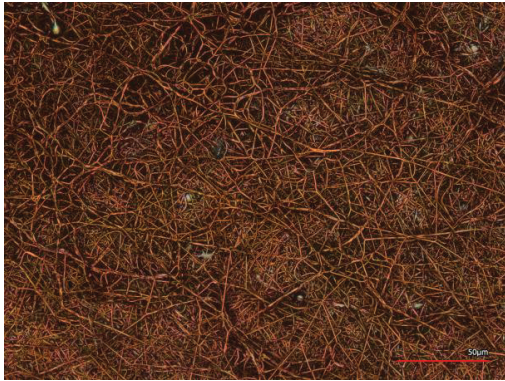
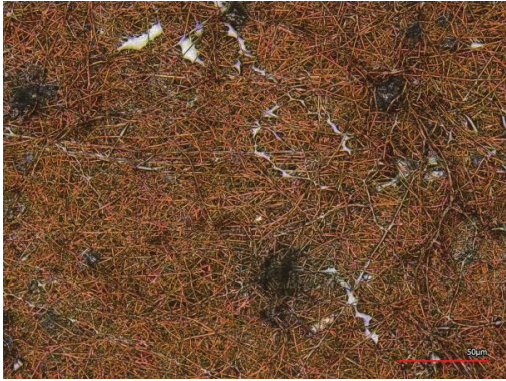
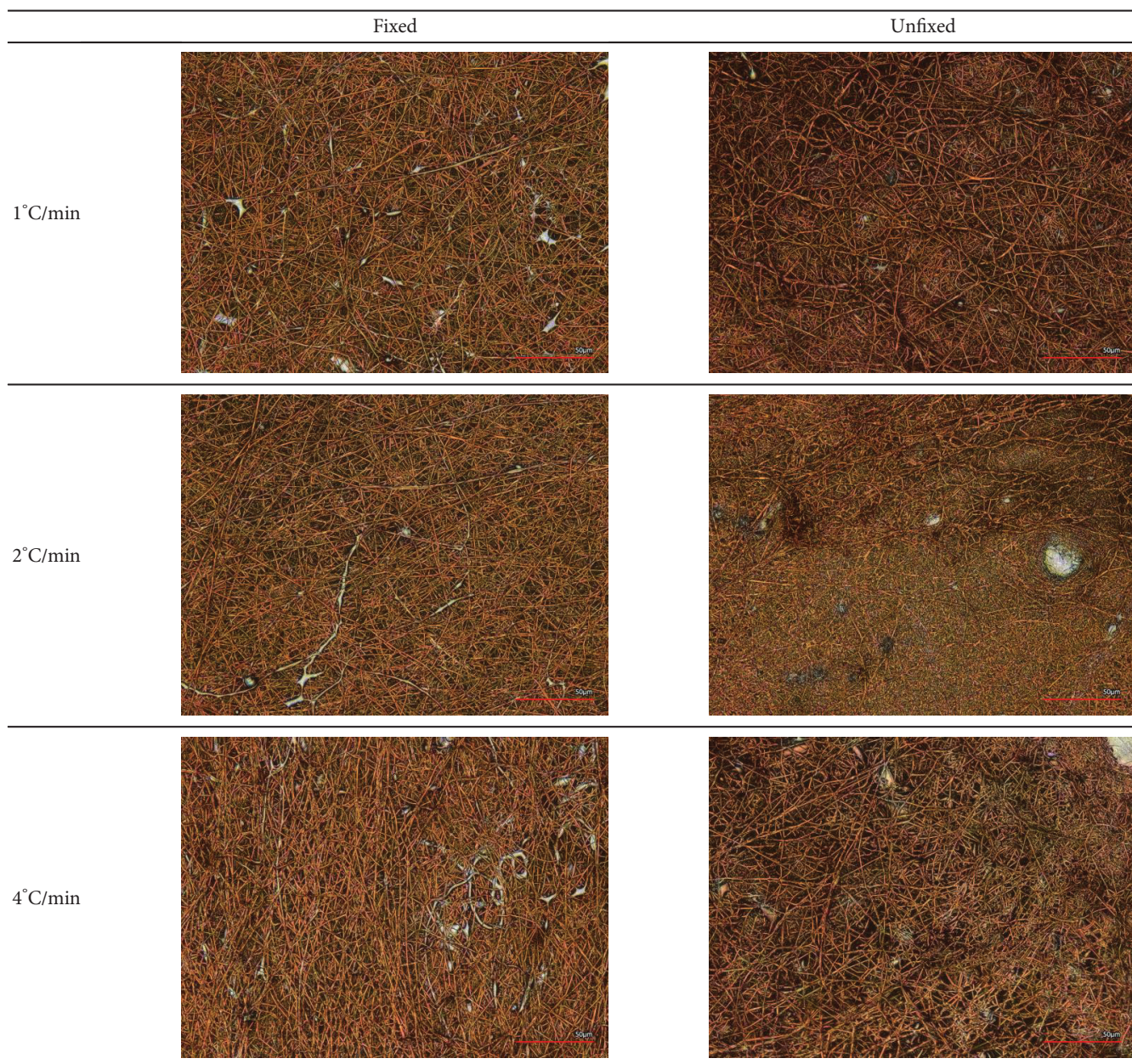
	Fixed	Unfixed
240°C		
260°C		
280°C		
300°C		

TABLE 2: CLSM images of PAN/gelatin nanofiber mat, stabilized in fixed (left panels) and unfixed state (right panels) at 280°C, approached with different heating rates. The scale bars indicate 50  $\mu\text{m}$ .



mentioned that—opposite to stabilization of pure PAN—the stabilization process here seems to straighten the fibers. Another important remark is that no undesired conglutinations are visible in the stabilized sample, as opposed to the stabilization process of pure PAN under identical conditions.

Table 1 compares the samples stabilized at different temperatures, approached with 1°C/min, in fixed and unfixed state. Firstly, most images show some areas in which silvery regions or fibers are visible which can clearly be attributed to gelatin since stabilized PAN shows a strong color change. Second, the typical crumpling of pure PAN fibers during stabilization is invisible for the fixed samples and severely reduced for the unfixed samples. This finding is independent

from the stabilization temperature, thus possibly allowing using higher stabilization temperatures without a problematic influence on the nanofiber dimensions.

This observation shows clearly that blending PAN with gelatin can help to gain straight, long carbon nanofibers, as desired for most technical applications.

Table 2 depicts the dependence of the nanofiber mat morphology after stabilization at 280°C, approached with different heating rates. For the higher heating rates, the more chaotic fiber distribution for the unfixed samples is visible; however, still, no undesired conglutinations seem to appear. The assumption due to Figure 6 that faster heating leads to more remaining gelatin cannot be verified or falsified from these images, especially since gelatin inside

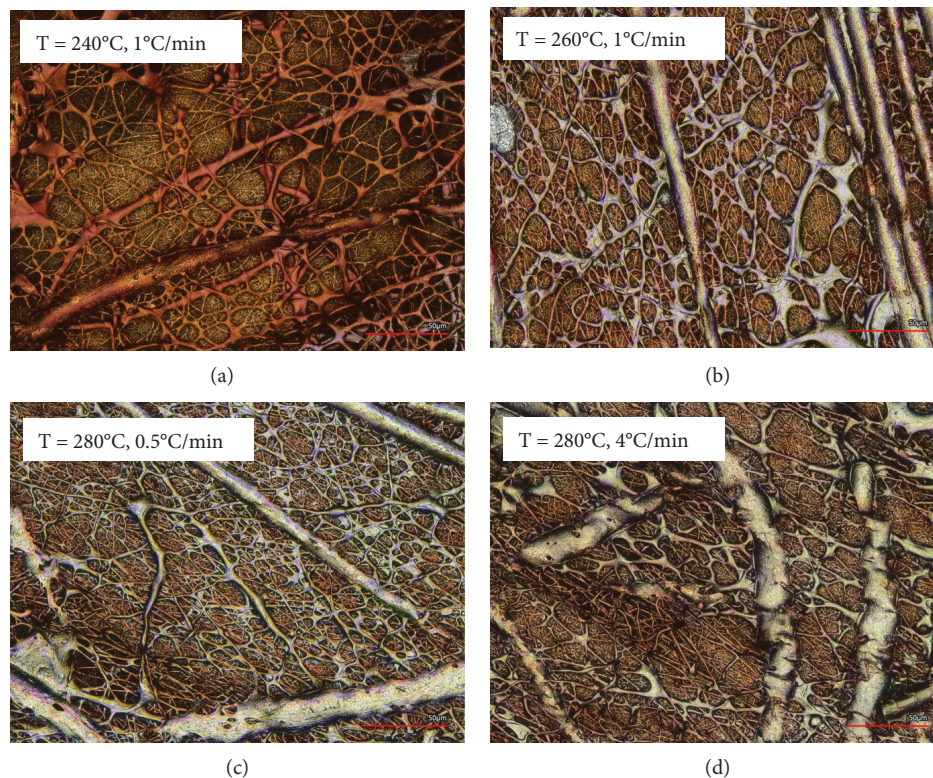


FIGURE 8: CLSM images of the back of different samples (see insets), stabilized under fixed conditions. The scale bars indicate 50  $\mu\text{m}$ .

PAN fibers or blended fibers cannot be distinguished from pure PAN fibers.

All samples were also investigated from the back, where residual gelatin was expected due to the dark color and the slight differences in the FTIR spectra. Some results of fixed samples are depicted in Figure 8.

Firstly, a significant color change from 240°C to 260°C can be recognized. This fits well to the starting point of the main thermal degradation zone of gelatin reported in the literature [26, 27]. Thermal degradation between 250°C and 600°C includes breakage of protein chains and rupture of peptide bonds, involving the evolution of volatile compounds and formation of new C-C and C-N bonds in the solid matrix.

Independent from this finding, in all cases (including the images not shown here), a mixture of broad gelatin bands and fine gelatin membranes connecting PAN fibers can be identified. No clear influence of the heating rate or the temperature (as long as it is higher than 240°C) is visible.

These images show that a stabilization process using hanging samples, without contact to the underground, may be favorable to reduce these large gelatin agglomerations. On the other hand, it should be mentioned that the next step, carbonization of the samples, is usually performed at temperatures higher than 600°C so that gelatin will most probably completely be degraded after the carbonization process. Nevertheless, the influence of such gelatin agglomerations on the morphology of carbonized nanofiber mats should be investigated in the future.

Next, the morphology of the fibers themselves was investigated using SEM. The results for different temperatures are

depicted in Table 3, while Table 4 shows the influence of different heating rates.

In all cases, the unfixed samples show stronger meandering of the fibers, an effect which is supported by high temperatures and high heating rates. Stabilization of fixed nanofiber mats results in most cases in straight, even fibers. Similar to the CLSM images, some gelatin fibers are still visible between the thinner PAN fibers. For the highest temperature and the highest heating rates, the fixed PAN fibers seem to be more irregular; thus, the SEM images suggest stabilization at 280°C (which is sufficient for stabilization, based on the FTIR results) and 1°C/min which is twice as high as the best stabilization temperature for pure PAN nanofiber mats of 0.5°C/min. It must be mentioned that the original aim of this study, creation and stabilization of PAN/gelatin nanofibers with porous surfaces, was not reached here, while the investigation gives a new approach to create smoother, more even fibers which can be stabilized with a higher heating rate than pure PAN nanofibers.

Finally, spectroscopic examinations of the stabilized nanofiber mats were performed. The color differences for the brighter front and the darker back compared to the original white nanofiber mat are depicted in Figure 9.

The difference between the dark and the “normal” areas is also visible in these measurements for all temperatures and heating rates. Interestingly, the maximum color difference is achieved at 280°C and decreases again at 300°C. This may be attributed to structural effects due to the degradation of gelatin. This explanation corresponds to the slightly increasing color differences with

TABLE 3: SEM images of PAN/gelatin nanofiber mat, stabilized in fixed (left panels) and unfixed state (right panels) at different temperatures, approached with 1°C/min. All images were taken using a nominal magnification of 5000x.

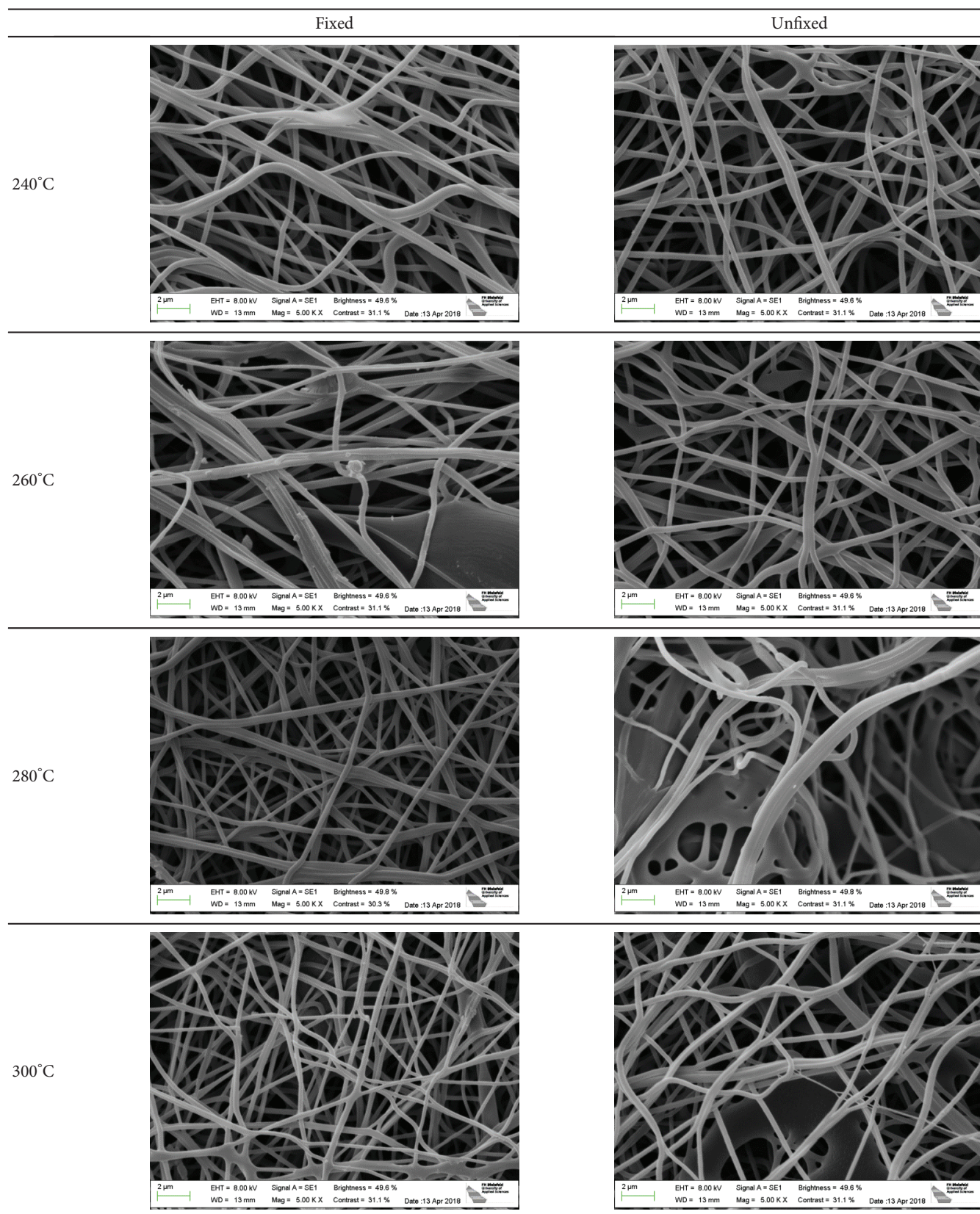
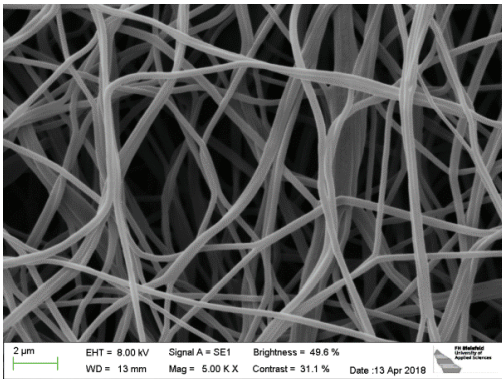
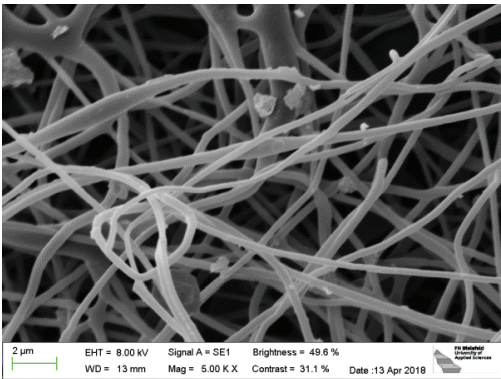
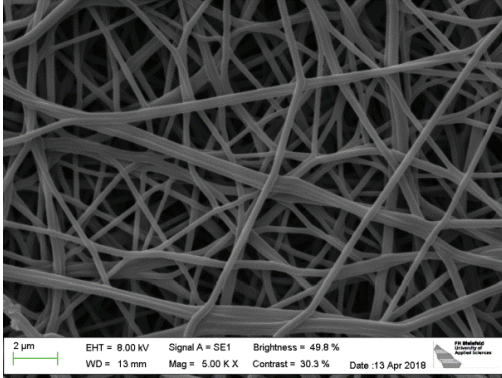
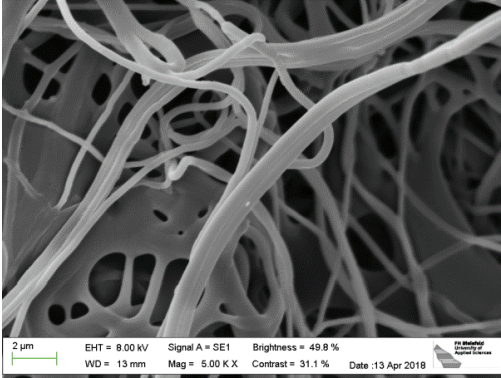
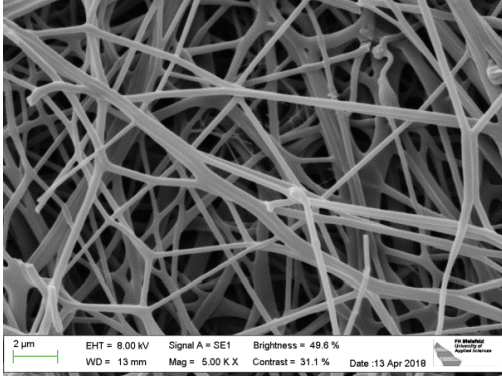
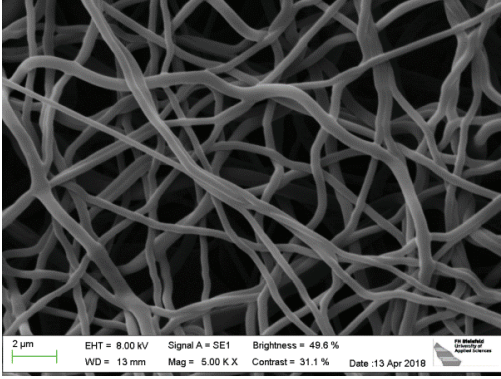
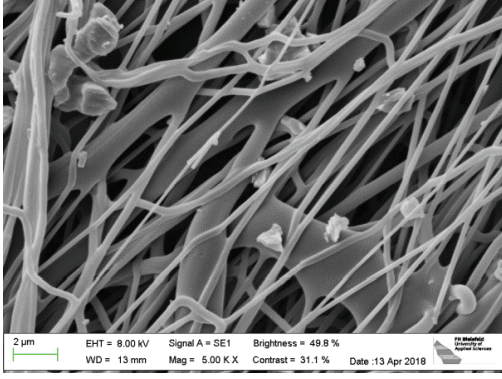
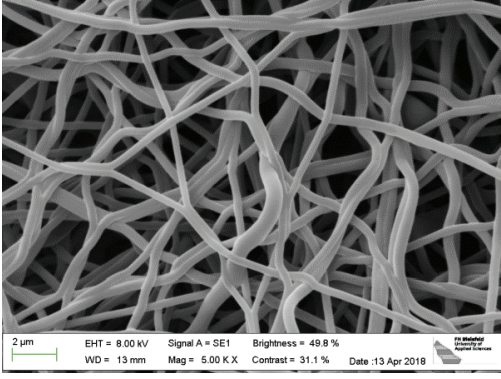


TABLE 4: SEM images of PAN/gelatin nanofiber mat, stabilized in fixed (left panels) and unfixed state (right panels) at 280°C, approached with different heating rates. All images were taken using a nominal magnification of 5000x.

	Fixed	Unfixed
0.5°C/min		
1°C/min		
2°C/min		
4°C/min		

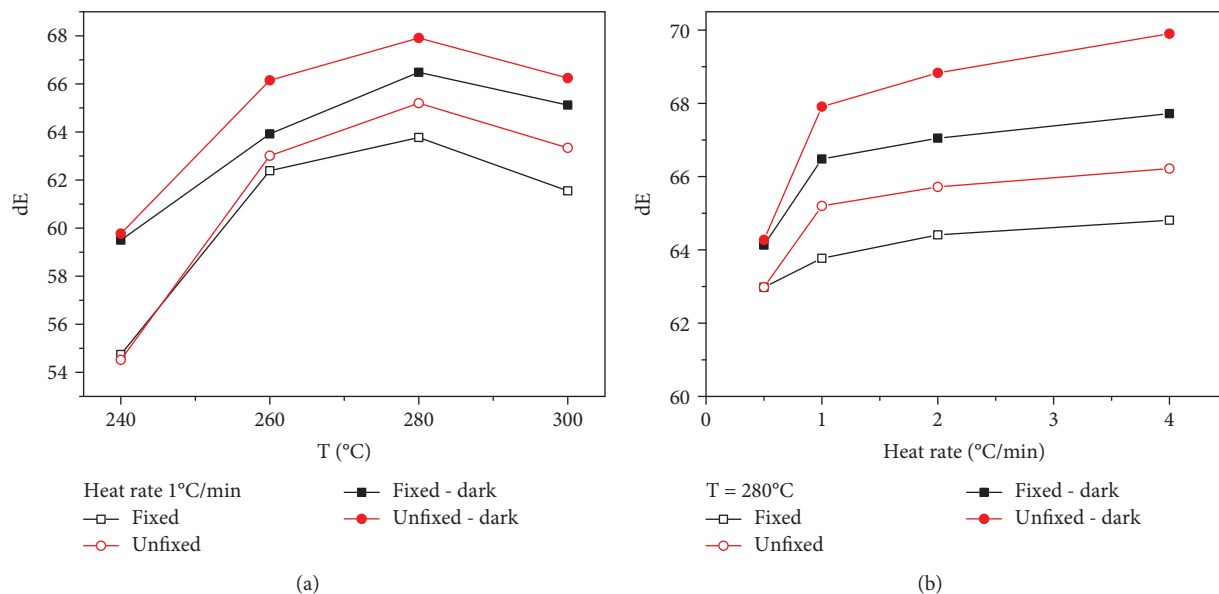


FIGURE 9: Color differences  $dE$  of samples stabilized at different end temperatures (a) and different heating rates (b) and isothermal treatment at the maximum temperature for 1 h.

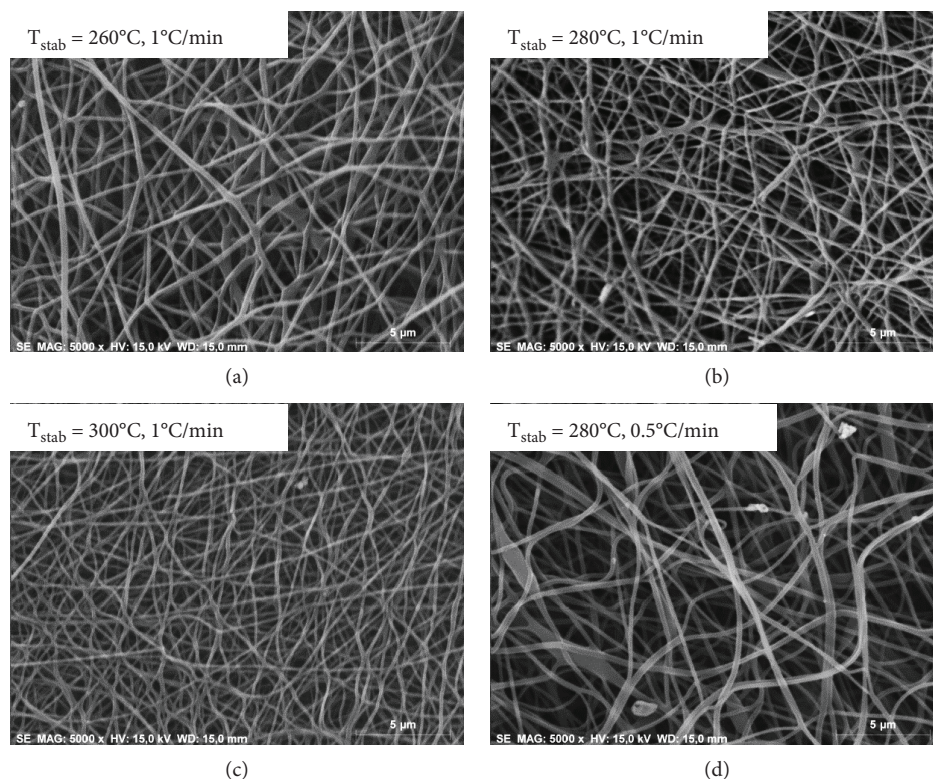


FIGURE 10: SEM images of some samples carbonized at  $800^{\circ}\text{C}$ .

increased heating rates, for which larger amounts of residual gelatin were found in the FTIR measurements (Figure 6).

It should be mentioned that for the smallest heating rate of  $0.5^{\circ}\text{C}/\text{min}$  as well as for the lowest temperature of  $240^{\circ}\text{C}$  (i.e., below the start of the gelatin degradation), there are no differences between fixed and unfixed samples visible. This

may indicate that under these stabilization conditions, the fixation of the samples is not necessary to gain straight fibers without undesired meandering.

Finally, some of the optimally stabilized samples (all fixed during stabilization) were carbonized at a temperature of  $800^{\circ}\text{C}$ . Figure 10 depicts the SEM images taken after carbonization.

TABLE 5: Stabilization and carbonization yields as well as overall yield after the whole process for the samples depicted in Figure 10.

	Stabilization yield	Carbonization yield	Overall yield
$T_{\text{stab}} = 260^{\circ}\text{C}$ , $1^{\circ}\text{C}/\text{min}$	79.8%	14.3%	11.3%
$T_{\text{stab}} = 280^{\circ}\text{C}$ , $1^{\circ}\text{C}/\text{min}$	74.8%	36.4%	27.2%
$T_{\text{stab}} = 300^{\circ}\text{C}$ , $1^{\circ}\text{C}/\text{min}$	64.9%	25.0%	16.2%
$T_{\text{stab}} = 280^{\circ}\text{C}$ , $0.5^{\circ}\text{C}/\text{min}$	71.8%	28.6%	20.5%

Comparing these images, it is clearly visible that thicker fibers are achieved by smaller stabilization temperatures ( $260^{\circ}\text{C}$ ) and lower heating rates ( $0.5^{\circ}\text{C}/\text{min}$ ). This corresponds to the results of the stabilization process, as depicted in Tables 3 and 4, and suggests future tests combining relatively low stabilization temperatures and heating rates to support this property. This result clearly shows that by carefully choosing the stabilization conditions, the intended increase of the fiber diameter can survive the stabilization process, while the blending material responsible for this diameter increase melts at much lower temperatures.

On the other hand, these properties must be balanced against the carbonization yields. Here, we found the values given in Table 5.

According to these numbers, a stabilization temperature of  $280^{\circ}\text{C}$  in combination with a stabilization heating rate of  $1^{\circ}\text{C}/\text{min}$  should be preferred. The temperature of  $260^{\circ}\text{C}$  results in a small carbonization yield, while the highest temperature of  $300^{\circ}\text{C}$  leads to a reduced stabilization yield. Comparing both alternatives resulting in relatively thick fibers, a small heating rate of  $0.5^{\circ}\text{C}/\text{min}$  in combination with the typical stabilization temperature of  $280^{\circ}\text{C}$  is preferable since the overall yield is nearly twice as high as in the case of the lower stabilization temperature.

Figure 11 shows the results of FTIR measurements on the samples depicted in Figure 10. After stabilization, the peaks visible after stabilization are nearly vanished. Only very few functional groups are left after this process, corresponding to the high absorbance of carbon, as it is well known from the carbonization process of PAN and other carbon precursors [28, 29]. It should be mentioned that the small peaks visible here are neither identical with those stemming from PAN nor stabilized PAN nor gelatin, showing that the samples are carbonized to a high degree.

#### 4. Conclusion

In this study, we have investigated electrospun PAN/gelatin nanofiber mats in terms of stabilization parameters and their influences on the resulting stabilized nanofibers. In all cases, the amount of gelatin was significantly reduced, especially above the onset of gelatin degradation at  $250^{\circ}\text{C}$ , as revealed by FTIR, CLSM, and SEM measurements. While adding gelatin did not result in creating porous PAN nanofibers after

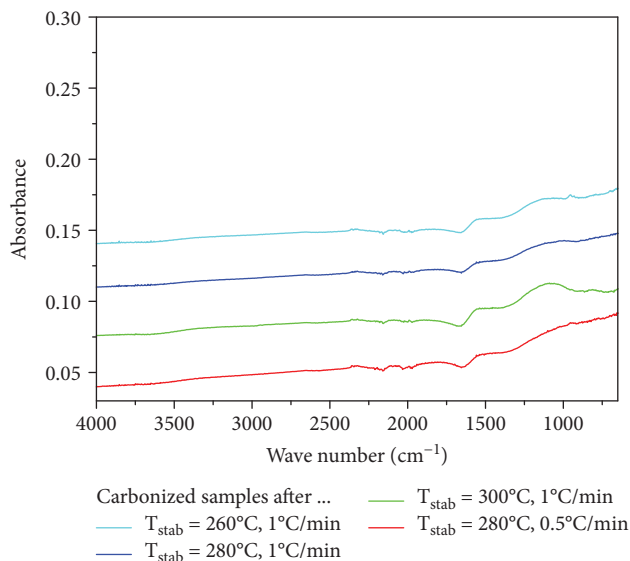


FIGURE 11: FTIR results of the samples carbonized at  $800^{\circ}\text{C}$ . The lines are offset vertically for clarity.

stabilization, we showed that using PAN/gelatin blends as precursors for carbon nanofibers offer a new possibility to create long, straight fibers without many undesired conglomerations. Future tests will concentrate on investigating the influence of the PAN:gelatin ratio on stabilization and subsequent carbonization processes.

#### Data Availability

All data used for the investigation are completely shown in the manuscript.

#### Conflicts of Interest

The authors declare that there is no conflict of interest regarding the publication of this paper.

#### Acknowledgments

The work was partly supported by the HiF funding of Bielefeld University of Applied Sciences. The authors acknowledge gratefully the program FH Basis of the German Federal Country North Rhine-Westphalia for funding the “Nanospider Lab.” We also acknowledge the Junta de Andalucía for the financial support to the group TEP-184.

#### References

- [1] J. He, W. Wang, R. Shi et al., “High speed water purification and efficient phosphate rejection by active nanofibrous membrane for microbial contamination and regrowth control,” *Chemical Engineering Journal*, vol. 337, pp. 428–435, 2018.
- [2] E. M. Cagil, F. Ozcan, and S. Ertul, “Fabrication of calixarene based protein scaffold by electrospin coating for tissue engineering,” *Journal of Nanoscience and Nanotechnology*, vol. 18, no. 8, pp. 5292–5298, 2018.

- [3] G. Potjewyd, S. Moxon, T. Wang, M. Domingos, and N. M. Hooper, "Tissue engineering 3D neurovascular units: a biomaterials and bioprinting perspective," *Trends in Biotechnology*, vol. 36, no. 4, pp. 457–472, 2018.
- [4] H. Tang, W. Chen, J. Wang, T. Dugger, L. Cruz, and D. Kisailus, "Electrocatalytic N-doped graphitic nanofiber – metal/metal oxide nanoparticle composites," *Small*, vol. 14, no. 11, article 1703459, 2018.
- [5] Y. Li and Y. Zheng, "Preparation and electrochemical properties of polyaniline/reduced graphene oxide composites," *Journal of Applied Polymer Science*, vol. 135, no. 16, article 46103, 2018.
- [6] Y. Li, J. Ji, Y. Wang, R. Li, and W. H. Zhong, "Soy protein-treated nanofillers creating adaptive interfaces in nanocomposites with effectively improved conductivity," *Journal of Materials Science*, vol. 53, pp. 8653–8665, 2018.
- [7] H. Wang, Y. Jiang, and A. Manthiram, "Long cycle life, low self-discharge sodium–selenium batteries with high selenium loading and suppressed polyselenide shuttling," *Advanced Energy Materials*, vol. 8, no. 7, article 1701953, 2018.
- [8] S. Yao, J. Cui, J. Huang et al., "Rational assembly of hollow microporous carbon spheres as P hosts for long-life sodium-ion batteries," *Advanced Energy Materials*, vol. 8, no. 7, article 1702267, 2018.
- [9] K. Wu, Y. Hu, Z. Shen et al., "Highly efficient and green fabrication of a modified C nanofiber interlayer for high-performance Li–S batteries," *Journal of Materials Chemistry A*, vol. 6, no. 6, pp. 2693–2699, 2018.
- [10] X. Song, S. Wang, G. Chen et al., "Fe-N-doped carbon nanofiber and graphene modified separator for lithium-sulfur batteries," *Chemical Engineering Journal*, vol. 333, pp. 564–571, 2018.
- [11] L. Zhu, L. You, P. Zhu, X. Shen, L. Yang, and K. Xiao, "High performance lithium–sulfur batteries with a sustainable and environmentally friendly carbon aerogel modified separator," *ACS Sustainable Chemistry & Engineering*, vol. 6, no. 1, pp. 248–257, 2018.
- [12] Y. Zhao, Y. Liu, C. Tong et al., "Flexible lignin-derived electrospun carbon nanofiber mats as a highly efficient and binder-free counter electrode for dye-sensitized solar cells," *Journal of Materials Science*, vol. 53, no. 10, pp. 7637–7647, 2018.
- [13] F. J. García-Mateos, R. Berenguer, M. J. Valero-Romero, J. Rodríguez-Mirasol, and T. Cordero, "Phosphorus functionalization for the rapid preparation of highly nanoporous submicron-diameter carbon fibers by electrospinning of lignin solutions," *Journal of Materials Chemistry A*, vol. 6, no. 3, pp. 1219–1233, 2018.
- [14] W. Fang, S. Yang, T. Q. Yuan, A. Charlton, and R. C. Sun, "Effects of various surfactants on alkali lignin electrospinning ability and spun fibers," *Industrial & Engineering Chemistry Research*, vol. 56, no. 34, pp. 9551–9559, 2017.
- [15] T. Grothe, D. Wehlage, T. Böhm, A. Remche, and A. Ehrmann, "Needleless electrospinning of PAN nanofibre mats," *Tekstilec*, vol. 60, no. 4, pp. 290–295, 2017.
- [16] L. Sabantina, J. R. Mirasol, T. Cordero, K. Finsterbusch, and A. Ehrmann, "Investigation of needleless electrospun PAN nanofiber mats," in *AIP Conference Proceedings*, vol. 1952, article 020085, Secunderabad, India, 2018.
- [17] C. Liu and K. Lafdi, "Fabrication and characterization of carbon nanofibers from polyacrylonitrile/pitch blends," *Journal of Applied Polymer Science*, vol. 134, no. 42, article 45388, 2017.
- [18] Y. W. Ju and G. Y. Oh, "Behavior of toluene adsorption on activated carbon nanofibers prepared by electrospinning of a polyacrylonitrile-cellulose acetate blending solution," *Korean Journal of Chemical Engineering*, vol. 34, no. 10, pp. 2731–2737, 2017.
- [19] D. Wehlage, R. Böttjer, T. Grothe, and A. Ehrmann, "Electrospinning water-soluble/insoluble polymer blends," *AIMS Materials Science*, vol. 5, no. 2, pp. 190–200, 2018.
- [20] L. Yu and L. Gu, "Effects of microstructure, crosslinking density, temperature and exterior load on dynamic pH-response of hydrolyzed polyacrylonitrile-*blend*-gelatin hydrogel fibers," *European Polymer Journal*, vol. 45, no. 6, pp. 1706–1715, 2009.
- [21] A. Bigi, G. Cojazzi, S. Panzavolta, K. Rubini, and N. Roveri, "Mechanical and thermal properties of gelatin films at different degrees of glutaraldehyde crosslinking," *Biomaterials*, vol. 22, no. 8, pp. 763–768, 2001.
- [22] E. Cipriani, M. Zanetti, P. Bracco, V. Brunella, M. P. Luda, and L. Costa, "Crosslinking and carbonization processes in PAN films and nanofibers," *Polymer Degradation and Stability*, vol. 123, pp. 178–188, 2016.
- [23] K. Mólnar, B. Szolnoki, A. Toldy, and L. M. Vas, "Thermochemical stabilization and analysis of continuously electrospun nanofibers," *Journal of Thermal Analysis and Calorimetry*, vol. 117, no. 3, pp. 1123–1135, 2014.
- [24] G. S. Al-Saidi, A. Al-Alawi, M. S. Rahman, and N. Guizani, "Fourier transform infrared (FTIR) spectroscopic study of extracted gelatin from shaari (*Lithrinus microdon*) skin: effects of extraction conditions," *International Food Research Journal*, vol. 19, pp. 1167–1173, 2012.
- [25] L. Sabantina, M. Rodríguez-Cano, M. Klöcker et al., "Fixing PAN nanofiber mats during stabilization for carbonization and creating novel metal/carbon composites," *Polymers*, vol. 10, no. 7, p. 735, 2018.
- [26] C. Peña, K. de la Caba, A. Eceiza, R. Ruseckaite, and I. Mondragon, "Enhancing water repellence and mechanical properties of gelatin films by tannin addition," *Bioresource Technology*, vol. 101, no. 17, pp. 6836–6842, 2010.
- [27] S. Gautam, A. K. Dinda, and N. C. Mishra, "Fabrication and characterization of PCL/gelatin composite nanofibrous scaffold for tissue engineering applications by electrospinning method," *Materials Science and Engineering: C*, vol. 33, no. 3, pp. 1228–1235, 2013.
- [28] S. N. Arshad, M. Naraghi, and I. Chasiotis, "Strong carbon nanofibers from electrospun polyacrylonitrile," *Carbon*, vol. 49, no. 5, pp. 1710–1719, 2011.
- [29] C.-W. Park, W.-J. Youe, S.-Y. Han, Y. S. Kim, and S.-H. Lee, "Characteristics of carbon nanofibers produced from lignin/polyacrylonitrile (PAN)/kraft lignin-g-PAN copolymer blends electrospun nanofibers," *Holzforschung*, vol. 71, no. 9, pp. 743–750, 2017.

## Research Article

# Opto-Electrical Properties of Composite Materials Based on Two Benzotrithiophene Copolymers and Fullerene Derivatives

N. Radychev<sup>1</sup>, M. L. Keshtov,<sup>2</sup> H. Borchert,<sup>1</sup> Y. Bondarchuk,<sup>1</sup> S. A. Kuklin,<sup>2</sup> A. Korotaeva,<sup>3</sup> Z. Xie,<sup>4</sup> D. Godovsky,<sup>2</sup> A. R. Khokhlov,<sup>2</sup> and J. Parisi<sup>1</sup>

<sup>1</sup>University of Oldenburg, Department of Physics, Energy and Semiconductor Research Laboratory, Carl-von-Ossietzky Str. 9-11, 26129 Oldenburg, Germany

<sup>2</sup>Vavilovsk., 28, Institute of Organoelement Compounds of the Russian Academy of Sciences, 119991 Moscow, Russia

<sup>3</sup>University of Oldenburg, Department of Computing Science, Escherweg 2, 26121 Oldenburg, Germany

<sup>4</sup>Changchun Institute of Applied Chemistry, Chinese Academy of Sciences, No. 5625 Renmin Rd., Changchun, Jilin 130022, China

Correspondence should be addressed to N. Radychev; nicolay.radychev@uni-oldenburg.de

Received 19 April 2018; Revised 3 August 2018; Accepted 8 August 2018; Published 14 October 2018

Academic Editor: Cheng-yu Hong

Copyright © 2018 N. Radychev et al. This is an open access article distributed under the Creative Commons Attribution License, which permits unrestricted use, distribution, and reproduction in any medium, provided the original work is properly cited.

Two donor-acceptor copolymers based on a benzotrithiophene acceptor unit and an electron-donor segment of 4,8-didodecyloxybenzo[1,2-b;4,5-b']dithiophene were investigated in the view of photovoltaic application. We provided the complete synthesis procedure supported with NMR spectra of the monomers obtained. The resulting copolymers, labeled P1 and P2 in this work, exhibit strong absorption in the visible region with a similar band gap of about 2.2 eV. In spite of the chemical similarity of both copolymers, the photovoltaic and carrier transport properties of the P1- and P2-based devices demonstrated a noticeable difference. Applying an optimization procedure, a power conversion efficiency of 4.6% has been achieved for the P2/PC<sub>71</sub>BM solar cells.

## 1. Introduction

Over the past years, since Tang et al. reported on a breakthrough in the polymer solar cells, a lot of efforts have been put into the development of organic photovoltaics [1–10]. Although electronic characteristics of the organic materials are still below those of usual inorganic semiconductors, such drawbacks might be compensated by fabrication on flexible substrates via inexpensive solution-phase techniques common in plastic manufacturing, e.g., applying roll-to-roll printing technology. The effective strategy to improve the performance of organic solar cells is the development of novel materials with promising photovoltaic properties. The power conversion efficiency (PCE) in the range of about 8–12% has been achieved for a number of bulk heterojunction solar cells based on novel absorbers with enhanced intrinsic properties [11–16]. One of the promising building blocks for the donor-acceptor copolymers is the benzotrithiophene (BTT) structure, which demonstrates encouraging characteristics

for organic electronics technology [17–22]. A large BTT structure is planar and leads to an effective intermolecular packaging in the solid state. Thereby, BTT-based copolymers have a highly ordered crystal structure and usually exhibit a high mobility of charge carriers in organic field-effect transistors [20, 21].

In spite of BTT blocks having an evident perspective for efficient photovoltaic devices, the synthesis and investigation of the BTT-containing copolymers are rather limited in comparison with the extensively studied benzodithiophene derivatives. In a recent report, we demonstrated that a BTT fragment, which is usually serving as a donor unit for the synthesis of conjugated copolymers, might perform the function of the electron acceptor moiety owing to the carbonyl group attached [23]. In that work, we described the general pathways of the synthesis procedure and performed a few initial tests towards the application potential of two corresponding donor-acceptor copolymers (labeled P1 and P2 in the following, respectively) in the field of organic photovoltaics.

Polymer–fullerene solar cells with P1 and P2 yielded up to 1.7% and 2.5% power conversion efficiency (PCE), respectively [23]. These experimental findings motivated us to focus current research on the opto-electrical properties of both P1 and P2 materials and their mixtures with fullerene derivatives.

## 2. Experimental

**2.1. Experiments and Characterization Methods.**  $^1\text{H}$  and  $^{13}\text{C}$  NMR spectra of the initial reagents and copolymers have been recorded on a spectrometer (Bruker Avance-400) operating at 400.13 and 100.62 MHz, respectively. The optical properties of the copolymers have been investigated with a Varian Cary 50 Scan spectrophotometer. The films were prepared by spin-casting of either P1 or P2 copolymers dissolved in anhydrous 1,2-dichlorobenzene (DCB) with a concentration of 6 mg/ml on quartz substrates. A xenon lamp has been used as an excitation source. The electrochemical properties have been examined by cyclic voltammetry (CV). Cyclic voltammograms were recorded on a CH Instruments (CHI660C) electrochemical work station with a three-electrode cell at a scan rate of  $100\text{ mV}\cdot\text{s}^{-1}$  (glassy carbon electrode, Pt wire, and saturated calomel electrode).  $\text{Bu}_4\text{NPF}_6$  ( $0.1\text{ mol}\cdot\text{l}^{-1}$ ) was used as an electrolyte, and anhydrous acetonitrile (drying with  $\text{CaH}_2$ ) was used as the solvent. Copolymers dissolved in DCB were drop-casted on the working electrode and dried under vacuum ( $\sim 10^{-2}$  torr) for 30 minutes. Transmission electron microscopy (TEM) of the active layers was performed on JEOL JEM-1011 operated at an acceleration voltage of 100 kV. Polymer–fullerene films for TEM were prepared in identical conditions to those prepared for device fabrication. The samples were immersed in water, and the active layer floating on the water surface was transferred to a TEM grid.

**2.2. Fabrication and Characterization of Thin Film Transistors and Organic Solar Cells.** The thin film transistors (TFTs) were prepared in order to examine the transport properties of both P1 and P2 copolymers. TFTs were fabricated on heavily n-doped silicon wafers with 230 nm thermally grown  $\text{SiO}_2$  dielectric layers and equipped with 16 transistors per substrate. Source and drain contacts are interdigitated structures (10 nm ITO, 60 nm Au) with channel lengths  $L = 2.5, 5, 10,$  and  $20\ \mu\text{m}$  and channel width  $W = 1\text{ cm}$ . All of the transistors were in the bottom-contact configuration with gold electrodes. The substrates were purchased from Fraunhofer IPMS (Dresden). The gate dielectric capacitance was calculated to be  $17\text{ nF}/\text{cm}^2$ . The wafers were cleaned in acetone and isopropyl alcohol in an ultrasonic bath for 10 min and then subjected to  $\text{O}_2$  plasma for 5 min. We applied octadecyltrichlorosilane (OTS, purchased from Sigma-Aldrich) as a self-assembled monolayer in order to modify the  $\text{SiO}_2$  dielectric surface and facilitate charge transport properties of the materials investigated [24, 25]. The cleaned substrates were treated with a solution of OTS in toluene (10 mM) for 20 min at  $60^\circ\text{C}$ . Afterwards, thin films (75 nm) of an organic semiconductor were spin-coated onto precleaned substrates and annealed for 15 min at  $140^\circ\text{C}$ . All steps of the TFT fabrication were processed in an  $\text{N}_2$  filled

glovebox. The electrical characterization of the TFTs was carried out at room temperature in the dark. The setup consists of two Keithley 2400 source measure units, 4-point probe station, and a PC running LabTracer program for automated measurements.

The photovoltaic characteristics of the devices have been investigated by fabricating conventional bulk heterojunction solar cells. Therefore, we blended the copolymer synthesized with either [6,6]-phenyl- $\text{C}_{61}$ -butyric acid methyl ester ( $\text{PC}_{61}\text{BM}$ ) or [6,6]-Phenyl  $\text{C}_{71}$  butyric acid methyl ester ( $\text{PC}_{71}\text{BM}$ ) in different weight ratios by dissolving the copolymers and fullerene derivatives in DCB solution at  $50^\circ\text{C}$  and stirring overnight. To avoid local short circuits, the ITO-covered glass substrates have been structured via removing the ITO on half of the substrate using HCl and zinc powder. The structuring was followed by mechanical cleaning as well as cleaning with acetone and isopropyl alcohol in an ultrasonic bath. This procedure was finished by  $\text{O}_2$  plasma etching. As an electron barrier for the anode, a layer of poly(3,4-ethylenedioxythiophene):poly(styrene sulfonate) (PEDOT:PSS, Clevis PVPAl 4083) was spin-coated on the cleaned substrate and dried at  $180^\circ\text{C}$  under nitrogen atmosphere for 10 min. The active layer was spin-coated on top of the PEDOT:PSS layer, and then all samples were annealed for 15 min at  $140^\circ\text{C}$  under an inert atmosphere. The devices were finished by sequential thermal evaporation of 15 nm LiF and 100 nm Al on top as the cathode. Current-voltage measurements were recorded with a Keithley 4200 source measure unit. The laboratory solar cells were illuminated with a simulated AM 1.5G spectrum by a Photo Emission Tech. solar simulator. The intensity of the solar simulator of  $1000\text{ W}/\text{m}^2$  was calibrated using a monocrystalline Si reference solar cell (Fraunhofer ISE, Freiburg). Spectral mismatch was not taken into account. All current-voltage measurements have been carried out at room temperature. The external quantum efficiency (EQE) measurements were performed under short-circuit conditions with a lock-in amplifier (SR830, Stanford Research System) at a chopping frequency of 280 Hz during illumination with a monochromatic light from a xenon lamp.

## 3. Results and Discussion

**3.1. Structural, Optical, and Electrochemical Properties of the Copolymers P1 and P2.** The copolymers P1 and P2 have been synthesized by a Stille reaction as described previously [23]. The details related to the synthesis as well as the chemical analysis of the materials can also be found in the Supporting Information to this article. The chemical structure of the copolymers investigated is shown in Figure 1.

Both organic materials synthesized exhibit strong absorption in the visible range up to 600 nm. The copolymer P1 demonstrates well-pronounced maxima at 400, 485, and 516 nm. The absorption peaks of P2 observed at 514 nm and 560 nm reveal a bathochromic shift when compared to the copolymer P1. The optical spectra of both copolymers have been analyzed with the goal to access optical bandgaps  $E_g^{\text{opt}}$  in accordance with Tauc's model [26]. Figures 2 and 3 demonstrate the plot of  $(\alpha\text{h}\nu)^2$  versus  $\text{h}\nu$  corresponding to the allowed

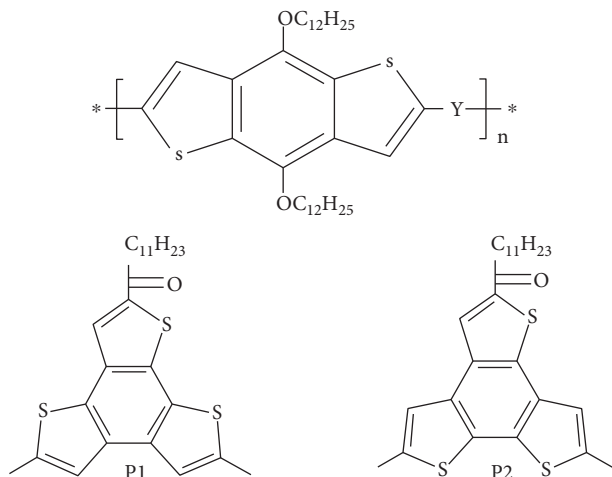


FIGURE 1: Chemical structure of the copolymers P1 and P2.

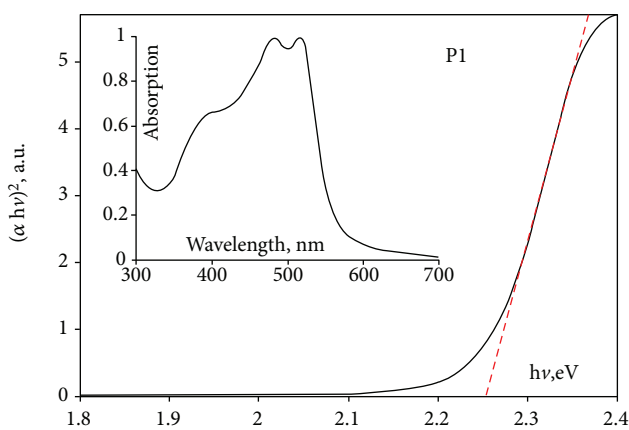


FIGURE 2: Tauc plot and normalized absorption (insert) of the thin films based on P1.

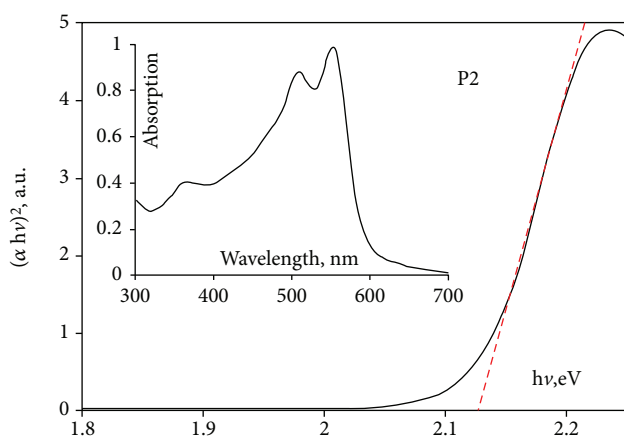


FIGURE 3: Tauc plot and normalized absorption (insert) of the thin films based on P2.

direct optical transitions for both P1- and P2-based thin films. The values of the energy gaps of  $E_{g1}^{\text{opt}} = 2.25$  eV (for P1 copolymer) and  $E_{g2}^{\text{opt}} = 2.12$  eV (for P2 copolymer) were derived by extrapolating the linear segments to the  $h\nu$  axis.

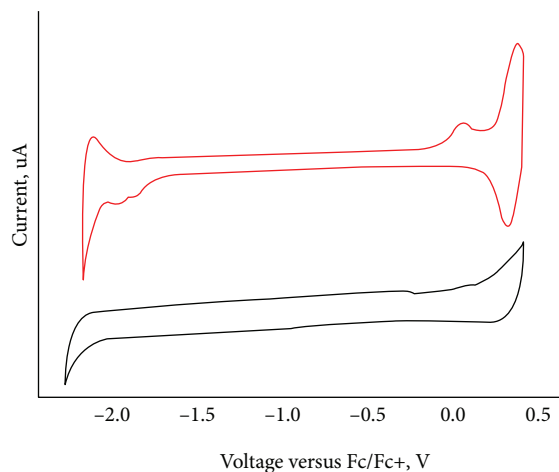


FIGURE 4: Cyclic voltammograms of P1 (red line) and P2 (black line) thin films recorded at a scan rate of 100 mV/s relative to Fc/Fc+.

TABLE 1: Electrochemical parameters and optical bandgaps of P1 and P2.

Polymer	$E^{\text{Homo}}$ (eV)	$E^{\text{Lumo}}$ (eV)	$E_g^{\text{ech}}$ (eV)	$E_g^{\text{opt}}$ (eV)
P1	-5.2	-3.0	2.2	2.25
P2	-5.1	-2.8	2.3	2.12

The electrochemical properties of the copolymers have been examined by CV measurements. Figure 4 shows exemplarily cyclic voltammograms of thin films spin-casted from DCB solutions. Both copolymers revealed reversible redox properties due to the high electroactivity. We attribute the cathodic reduction peak to the formation of thiophene radical anions, while the anodic oxidation peak likely corresponds to the radical cations of the thiophene moiety. The position of the energy levels was calculated from the oxidation potential  $E^{\text{ox}}$  and the reduction potential  $E^{\text{red}}$  in accordance with the equations:

$$\begin{aligned} E^{\text{Homo}} &= -e(E^{\text{ox}} + 4.8) \text{ eV}, \\ E^{\text{Lumo}} &= -e(E^{\text{red}} + 4.8) \text{ eV}. \end{aligned} \quad (1)$$

Taking here the onset potentials, the ionization potential ( $E^{\text{Homo}}$ ) and electron affinity ( $E^{\text{Lumo}}$ ) values of P1 were found to be -5.2 eV and -3.0 eV, respectively. The corresponding values for P2 were -5.1 eV and -2.8 eV, respectively. The bandgaps obtained ( $E_g^{\text{ech}}$ ) from CV measurements are in close agreement with the optical bandgaps estimated. The electrochemical parameters and the bandgaps derived from Tauc plots are summarized in Table 1.

**3.2. Charge Transport Properties.** The potential of two donor-acceptor copolymers as hole transporting materials has been evaluated in TFT structures. Analyzing transistor characteristics, we extracted parameters such as the field-effect mobility ( $\mu_{\text{fe}}$ ) and threshold voltage ( $V_{\text{tr}}$ ), which in turn have a strong influence on the solar cell performance.

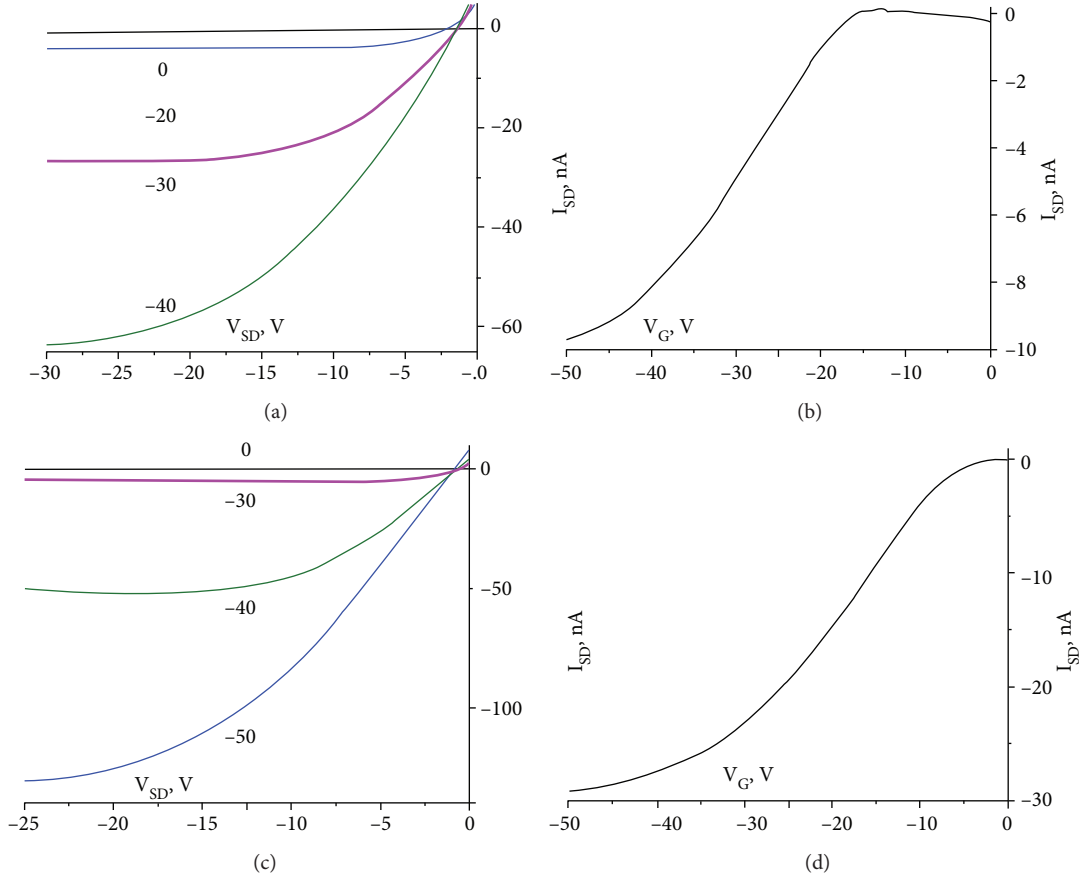


FIGURE 5: Output (a and c) and transfer (b and d) characteristics of thin film transistors based on either P1 (a and b) or P2 (c and d) copolymers.

The value of  $\mu_{fe}$  can be extracted from either the saturation or linear regime of the current-voltage characteristics. However, it was shown that field-effect mobility determined from the linear regime characterizes more precisely the intrinsic properties of a material and estimates the maximum mobility value in a real transistor [27]. Hence, in this work,  $\mu_{fe}$  has been derived from the linear regime in accordance with [28].

The typical transfer curves and output characteristics of both P1 and P2 materials at room temperature are shown in Figure 5. In the linear regime,  $\mu_{fe}$  was evaluated from the current-voltage characteristics of the FET using the following equation, when the source-drain current  $I_{sd}$  is plotted against the gate voltage  $V_{gs}$  at a low, constant source-drain voltage  $V_{sd}$ :

$$\frac{\partial I_{sd}}{\partial V_{gs}} = \mu_{fe} WC_i \frac{V_{sd}}{L}, \quad (2)$$

where  $W$  is the width of the channel,  $C_i$  is the capacitance per unit area of the oxide layer, and  $L$  is the length of the channel. The average value of  $\mu_{feP1}$  obtained for the device based on P1 copolymer was  $4.1 \times 10^{-6} \text{ cm}^2 \text{ V}^{-1} \text{ s}^{-1}$  with a threshold voltage of  $-34 \text{ V}$ . The transport characteristics of the P2 samples revealed us a considerable enhancement of the hole mobility. The current measured in P2-based FETs was about a factor of 3 greater when compared with

P1-based transistors. The average value of  $\mu_{feP2}$  was found to be  $2.5 \times 10^{-5} \text{ cm}^2 \text{ V}^{-1} \text{ s}^{-1}$ , while the threshold voltage remained almost unchanged. We note here that, contrary to expectations, structurally very similar organic materials demonstrated significant difference in charge transport properties. It is reasonable to attribute the phenomenon observed to variable positions of the sulfur atom in copolymers investigated, which plays a key role in the formation of intermolecular interactions and, consequently, impact on the hole transport properties [29, 30].

**3.3. Photovoltaic Response of P1-Based Devices.** The photovoltaic response of the copolymers was investigated by fabricating conventional bulk heterojunction solar cells with fullerene derivatives. In order to optimize the performance of the solar cells prepared, the polymer–fullerene weight ratio and the thickness of the active layer were stepwise varied. At the initial stage of the solar cell investigation, we observed a poor performance of the devices based on P1. Specifically, we obtained extremely low fill factor (FF) of about 0.4 and the maximum PCE of 1.6% even when the optimization procedure has been applied (Figure S4). We assume that limited hole mobility of P1 (obtained in Section 3.2) results in an inefficient charge carrier collection process and, hence, significantly reduces both the FF and photocurrent of P1-based solar cells [31–34]. Moreover, the low value of  $\mu_{feP1}$

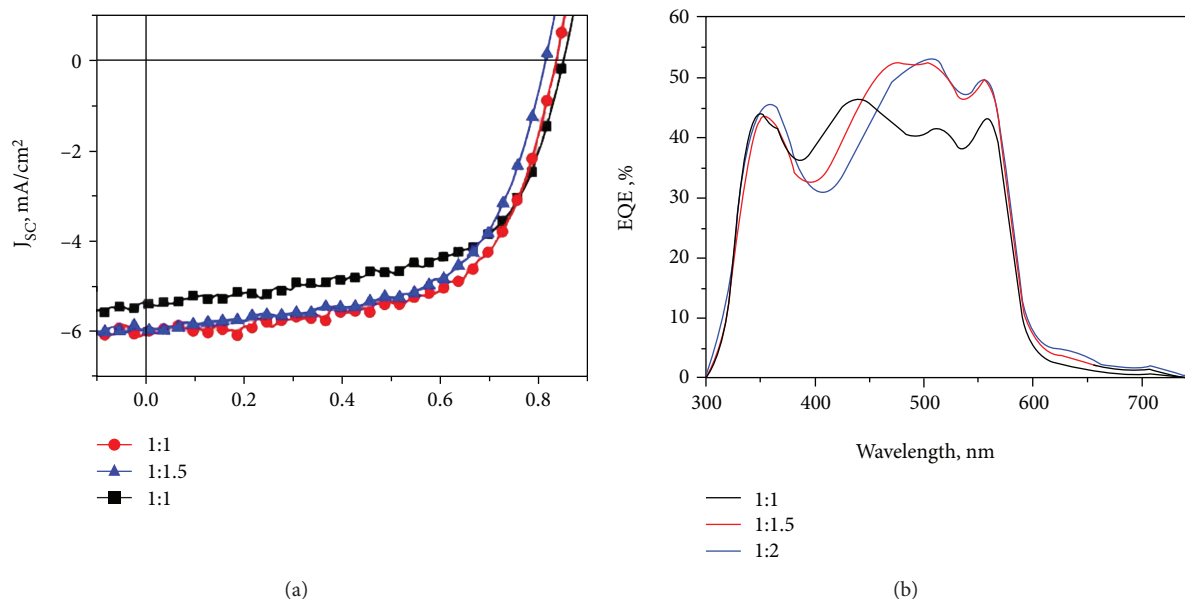


FIGURE 6:  $J$ - $V$  and EQE characteristics of P2/PC<sub>61</sub>BM solar cells with different polymer–fullerene weight ratios. Thickness of the active layer is 110 nm.

can aggravate the problem of balanced charge mobility in the bulk leading to the creation of a space charge region, which may limit the photovoltaic performance as well. Owing to these causes, the photovoltaic parameters presented in Figure S4 are far behind in comparison with state-of-the-art devices based on BTT materials [18, 35]. The current density–voltage characteristics of the P1-based devices are summarized in Table S1.

**3.4. Performance of P2-Based Solar Cells.** In contrast, the laboratory devices mixed with P2 demonstrated reasonable photoresponse, pointing to a promising potential for PV application. Taking these results into account, we focused our efforts on the P2-based solar cells.

According to a number of studies, the polymer : fullerene ratio in the organic solar cells is generally spread in the range of 1 : 3 [36]. Slight variations of the fullerene ratio with respect to the conjugated polymer demonstrate noticeable impact on the photovoltaic parameters. As shown in Figure 6(a), the short-circuit current density ( $J_{sc}$ ) increases from 5.3 mA/cm<sup>2</sup> to 6.1 mA/cm<sup>2</sup> for a polymer : fullerene ratio of 1 : 1 and 1 : 1.5, respectively. Subsequent growth of the fullerene content in the organic mixture results in slight reduction of the photovoltaic characteristics. The noticeable influence of the higher PC<sub>61</sub>BM blending ratio on the density of free charge carriers extracted at the electrodes is represented in Figure 6(b). The advanced devices demonstrate broad photoresponse in the visible part of the spectrum with external quantum efficiency (EQE) up to 52%. It is important to note that we observed about 10% enhancement in EQE within the wavelength range of 450–600 nm for the samples with optimized fullerene content. The corresponding photovoltaic performance values of the solar cells with different ratios are summarized in Table S2.

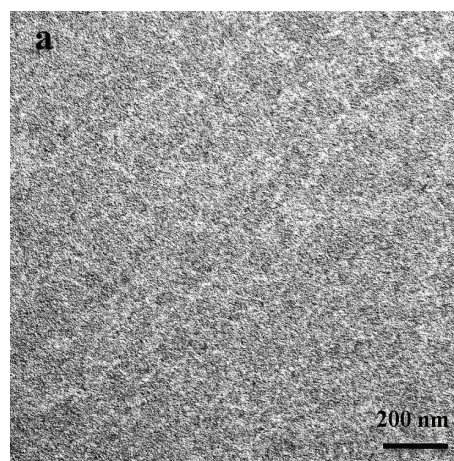


FIGURE 7: TEM picture of P2/PC<sub>61</sub>BM active layers.

It is known that either polymer–fullerene or hybrid solar cells work best across a narrow range of the active layer thickness. However, due to different charge transport characteristics of materials investigated, there is still a wide spread of results discussed in the literature for the appropriate thickness of the absorber, values ranging from 55 nm to 200 nm [36–41]. Applying a favorable polymer : fullerene ratio of 1 : 1.5 and keeping all other conditions of the solar cell preparation constant, the photovoltaic properties of samples set with different active layer thickness were investigated. As can be seen from Table S3, the variation of the active layer did not result in evident improvement of  $J_{sc}$  and open-circuit voltage ( $V_{oc}$ ), which were in the range of 5.8–6.1 mA/cm<sup>2</sup> and 0.82–0.85 V, respectively. However, the fill factor (FF) increases from 58% for a thickness of 130 nm to 65% for an 80 nm thick active layer, leading to

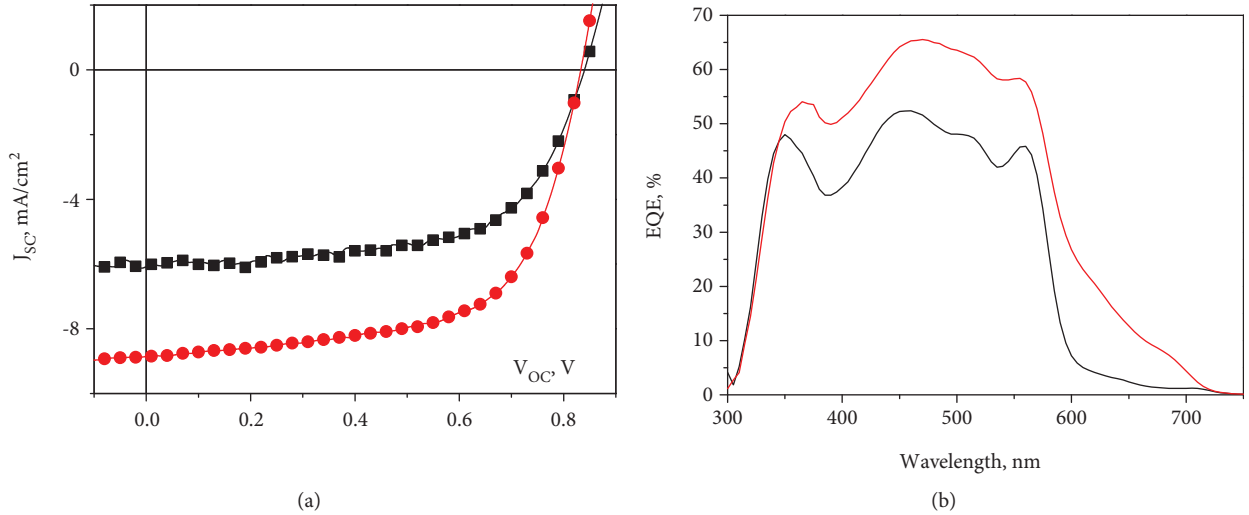


FIGURE 8:  $J$ - $V$  and EQE characteristics of P2/PC<sub>61</sub>BM (black curve) and P2/PC<sub>71</sub>BM (red curves) solar cells.

a PCE enhancement from 2.7% up to 3.3% (Figure S5). For devices with an absorber layer thinner than 80 nm, we observed a dramatic drop of the photocurrent that is attributed, in the first place, to an insufficient light-harvesting process. The results obtained are in good agreement with theoretical modeling done for polymer–fullerene solar cells and with our previous studies devoted to the inorganic-organic solar cells [42, 43]. The active layer morphology of P2/PC<sub>61</sub>BM was controlled by microscopic analysis. According to the differences in the electron scattering densities, the bright and dark regions observed in the TEM picture correspond to polymer and fullerene rich domains, respectively [44]. Figure 7 shows similar bicontinuous blends consisting of P2 and PC<sub>61</sub>BM nanostructured clusters and pointing to appreciable miscibility between the copolymer and fullerene acceptor. However, it is important to note that we observed a poor fibrillar structure associated with the P2 crystalline phase. This finding can cause suppressed charge transport across the polymer matrix and limited photovoltaic performance of P2/PC<sub>61</sub>BM solar cells.

Next, we also examined a combination of P2 with the PC<sub>71</sub>BM acceptor. It is well established that PC<sub>71</sub>BM has similar to PC<sub>61</sub>BM electronic properties but demonstrates a stronger absorption in the visible region [44]. The current density versus voltage characteristics ( $J$ - $V$ ) of the P2/PC<sub>61</sub>BM and P2/PC<sub>71</sub>BM solar cells fabricated in accordance with optimized parameters are shown in Figure 8(a). The application of PC<sub>71</sub>BM did not significantly influence  $V_{oc}$  and FF of the P2/PC<sub>71</sub>BM devices when compared with P2/PC<sub>61</sub>BM solar cells (Table 2). However, we observed considerable improvement of the  $J_{sc}$  from 6.1 mA/cm<sup>2</sup> to 8.8 mA/cm<sup>2</sup>, which is confirmed by the EQE spectrum as well (Figure 8(b)). The external quantum efficiency of the P2/PC<sub>71</sub>BM devices exhibits superior photoresponse when compared with P2/PC<sub>61</sub>BM samples, approaching a value of the EQE of about 60% in the wavelength range from 420 nm to 550 nm. The integration of the EQE spectra for the devices investigated with AM 1.5G solar spectrum

TABLE 2: Photovoltaic parameters of P2-based solar cells mixed with different acceptors.

Acceptor	$V_{oc}$ (V)	$J_{sc}$ (mA/cm <sup>2</sup> )	$J_{sc}^a$ (mA/cm <sup>2</sup> )	FF (%)	PCE (%)
PC <sub>61</sub> BM	0.84	6.1	5.9	62.5	3.2
PC <sub>71</sub> BM	0.83	8.8	8.5	63.1	4.6

<sup>a</sup>Calculated from EQE.

revealed us slightly smaller  $J_{sc}$  than the values gained from  $J$ - $V$  curves (see Table 2), but these differences are not significant and theoretical values of  $J_{sc}$  are in good agreement with the experimental data. Controlling the morphology of the P2/PC<sub>71</sub>BM active layers, we observed pronounced nanometer-scale phase separation. However, in comparison with P2/PC<sub>61</sub>BM, P2/PC<sub>71</sub>BM-based films demonstrated rather unique morphology, where bundles of P2 fibrils can be distinguished. We speculate that advanced performance of the P2/PC<sub>71</sub>BM solar cells originates not only from the stronger absorption of PC<sub>71</sub>BM in the visible range but also from enhancement of the charge-transfer pathways shown in Figure 9. Omitting the introduction of processing additives in the bulk heterojunction solution, the best samples based on the P2/PC<sub>71</sub>BM active layers achieved PCE of 4.6%. The photovoltaic parameters obtained are comparable with the results discussed in similar studies and related to BTT-containing organic solar cells [35, 45]. We should note that photovoltaic response achieved in this work is still behind the PCE of the champion device based on BTT building blocks [46]. Additional strategies, like solvent additives and extra purification of P2 copolymer, might bring further advance in the photovoltaic performance of the devices investigated.

#### 4. Conclusion

We have designed and synthesized two BTT-based D-A copolymers, labeled P1 and P2. The optical and electrochemical properties of the copolymers demonstrated a strong

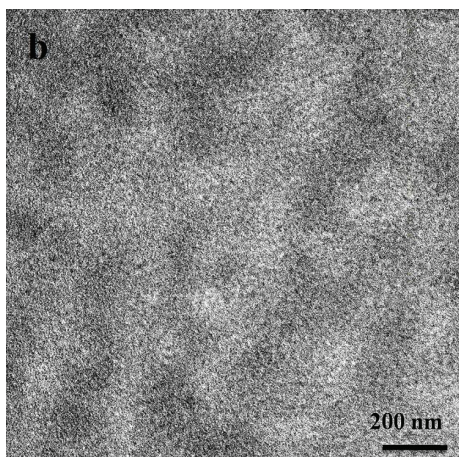


FIGURE 9: TEM picture of the P2/PC<sub>71</sub>BM active layer.

absorption in the UV-visible region with similar bandgap values of about 2.2 eV. The potential of both copolymers as hole transporting materials has been evaluated in TFT structures. The average values of the field-effect mobility obtained for the device based on either P1 or P2 were  $4.1 \times 10^{-6} \text{ cm}^2 \text{ V}^{-1} \text{ c}^{-1}$  and  $2.5 \times 10^{-5} \text{ cm}^2 \text{ V}^{-1} \text{ c}^{-1}$ , respectively. Thus, although the structure of the polymers is rather similar, a pronounced difference of the hole mobility was found. In spite of the fact that we did not achieve a reasonable photovoltaic response for the laboratory devices with a bulk heterojunction composed of the P1 copolymer and fullerene derivatives, the solar cells based on P2:fullerene blends revealed us promising photovoltaic characteristics. P2/PC<sub>71</sub>BM devices demonstrated performance parameters of a short-circuit current density up to  $8.8 \text{ mA/cm}^2$ , an open-circuit voltage of 0.83 V, a fill factor of about 63%, and up to 4.6% power conversion efficiency. The photovoltaic parameters obtained are comparable with known BTT-based organic solar cells so that the new BTT-based copolymer P2 appears as a perspective material for further investigation and advancement in the field of organic electronics.

### Data Availability

The absorption data, the data related to transfer characteristics of thin film transistors, and  $J$ - $V$  and EQE characteristics of the solar cells investigated are available from the corresponding author upon request. The data describing the chemical structure of the copolymers might be found in Supplementary Materials.

### Conflicts of Interest

The authors declare that there are no conflicts of interest regarding the publication of this paper.

### Acknowledgments

The authors thank the EWE AG Oldenburg, Germany, for financial support of the project “EWE Nachwuchsgruppe Dünnschichtphotovoltaik.” M. L. Keshtov, S. A. Kuklin,

D. Y. Godovsky, and N. Radychev thank the Russian Science Foundation (project no. 17-53-53198) for financial support.

### Supplementary Materials

The synthesis pathways of copolymers investigated and characterization of the intermediate compounds by elemental analysis, IR spectroscopy, <sup>1</sup>H and <sup>13</sup>C NMR are described. Additional photovoltaic characterizations of P1/PC<sub>61</sub>BM and P2/PC<sub>61</sub>BM solar cells are available as well. Figure S1: the synthesis pathways of monomers 5 and 8. Figure S2: <sup>1</sup>H (a) and <sup>13</sup>C NMR (b) spectra of 2,5-dibromo-8-dodecanoylbenzo[1,2-b:3,4-b':5,6-d'']trithiophene (5). Figure S3: <sup>1</sup>H NMR of the polymers P1 (a) and P2 (b). Figure S4:  $J$ - $V$  and EQE characteristics of P1/PC<sub>61</sub>BM solar cells with different polymer–fullerene weight ratios. Figure S5:  $J$ - $V$  and EQE characteristics of P2/PC<sub>61</sub>BM solar cells with different active layer thickness. Table S1: photovoltaic characteristics of P1/PC<sub>61</sub>BM devices with different polymer–fullerene weight ratios. Table S2: photovoltaic characteristics of P2/PC<sub>61</sub>BM devices with different polymer–fullerene weight ratios. Table S3: photovoltaic characteristics of P2/PC<sub>61</sub>BM devices with different thickness of the active layers. (Supplementary Materials)

### References

- [1] C. W. Tang, “Two-layer organic photovoltaic cell,” *Applied Physics Letters*, vol. 48, no. 2, pp. 183–185, 1986.
- [2] G. Yu, J. Gao, J. C. Hummelen, F. Wudl, and A. J. Heeger, “Polymer photovoltaic cells: enhanced efficiencies via a network of internal donor-acceptor heterojunctions,” *Science*, vol. 270, no. 5243, pp. 1789–1791, 1995.
- [3] J. Chen and Y. Cao, “Development of novel conjugated donor polymers for high-efficiency bulk-heterojunction photovoltaic devices,” *Accounts of Chemical Research*, vol. 42, no. 11, pp. 1709–1718, 2009.
- [4] M. C. Scharber, D. Mühlbacher, M. Koppe et al., “Design rules for donors in bulk-heterojunction solar cells—towards 10% energy-conversion efficiency,” *Advanced Materials*, vol. 18, no. 6, pp. 789–794, 2006.
- [5] G. P. Smestad, F. C. Krebs, C. M. Lampert et al., “Reporting solar cell efficiencies in solar energy materials and solar cells,” *Solar Energy Materials & Solar Cells*, vol. 92, no. 4, pp. 371–373, 2008.
- [6] C. Duan, F. Huang, and Y. Cao, “Recent development of push-pull conjugated polymers for bulk-heterojunction photovoltaics: rational design and fine tailoring of molecular structures,” *Journal of Materials Chemistry*, vol. 22, no. 21, pp. 10416–10434, 2012.
- [7] Z. He, B. Xiao, F. Liu et al., “Single-junction polymer solar cells with high efficiency and photovoltage,” *Nature Photonics*, vol. 9, no. 3, pp. 174–179, 2015.
- [8] J. Zhao, Y. Li, G. Yang et al., “Efficient organic solar cells processed from hydrocarbon solvents,” *Nature Energy*, vol. 1, no. 2, article 15027, 2016.
- [9] H. Zhou, Y. Zhang, C.-K. Mai et al., “Polymer homo-tandem solar cells with best efficiency of 11.3%,” *Advanced Materials*, vol. 27, no. 10, pp. 1767–1773, 2015.

- [10] S. Bi, Z. Ouyang, S. Shaik, and D. Li, "Effect of donor-acceptor vertical composition profile on performance of organic bulk heterojunction solar cells," *Scientific Reports*, vol. 8, no. 1, p. 9574, 2018.
- [11] Y. Lin, J. Wang, Z. G. Zhang et al., "An electron acceptor challenging fullerenes for efficient polymer solar cells," *Advanced Materials*, vol. 27, no. 7, pp. 1170–1174, 2015.
- [12] S. Li, L. Ye, W. Zhao et al., "Energy-level modulation of small-molecule electron acceptors to achieve over 12% efficiency in polymer solar cells," *Advanced Materials*, vol. 28, no. 42, pp. 9423–9429, 2016.
- [13] J. Subbiah, B. Purushothaman, M. Chen et al., "Organic solar cells using a high-molecular-weight benzodithiophene-benzothiadiazole copolymer with an efficiency of 9.4%," *Advanced Materials*, vol. 27, no. 4, pp. 702–705, 2015.
- [14] P. Liu, K. Zhang, F. Liu et al., "Effect of fluorine content in thienothiophene-benzodithiophene copolymers on the morphology and performance of polymer solar cells," *Chemistry of Materials*, vol. 26, no. 9, pp. 3009–3017, 2014.
- [15] N. Wang, Z. Chen, W. Wei, and Z. Jiang, *American Chemical Society*, vol. 135, no. 45, pp. 17060–17068, 2013.
- [16] P. R. Berger and M. Kim, "Polymer solar cells: P3HT:PCBM and beyond," *Journal of Renewable and Sustainable Energy*, vol. 10, no. 1, article 013508, 2018.
- [17] X. Guo, S. R. Puniredd, M. Baumgarten, W. Pisula, and K. Müllen, *Advanced Materials*, vol. 25, no. 38, pp. 5467–5472, 2013.
- [18] X. Zhao, D. Yang, H. Lv, L. Yin, and X. Yang, *Polymer Chemistry*, vol. 4, no. 1, pp. 57–60, 2013.
- [19] S.-C. Lan, P.-A. Yang, M.-J. Zhu, C.-M. Yu, J.-M. Jiang, and K.-H. Wei, *Polymer Chemistry*, vol. 4, no. 4, pp. 1132–1140, 2013.
- [20] B. C. Schroeder, C. B. Nielsen, Y. J. Kim et al., *Chemistry of Materials*, vol. 23, no. 17, pp. 4025–4031, 2011.
- [21] B. C. Schroeder, S. Rossbauer, R. J. Kline et al., "Benzotrithiophene copolymers: influence of molecular packing and energy levels on charge carrier mobility," *Macromolecules*, vol. 47, no. 9, pp. 2883–2890, 2014.
- [22] A. Molina-Ontoria, I. Zimmermann, I. Garcia-Benito et al., "Benzotrithiophene-based hole-transporting materials for 18.2% perovskite solar cells," *Angewandte Chemie, International Edition*, vol. 55, no. 21, pp. 6270–6274, 2016.
- [23] M. L. Keshtov, S. A. Kuklin, V. S. Kochurov, N. A. Radychev, Z. Xie, and A. R. Khokhlov, *Doklady Chemistry*, vol. 464, no. 2, pp. 231–235, 2015.
- [24] H. Sirringhaus, P. J. Brown, R. H. Friend et al., "Two-dimensional charge transport in self-organized, high-mobility conjugated polymers," *Nature*, vol. 401, no. 6754, pp. 685–688, 1999.
- [25] F. Todescato, R. Capelli, F. Dinelli et al., "Correlation between dielectric/organic interface properties and key electrical parameters in PPV-based OFETs," *The Journal of Physical Chemistry B*, vol. 112, no. 33, pp. 10130–10136, 2008.
- [26] J. Tauc and F. Abeles, *Optical Properties of Solids*, North-Holland, Amsterdam, Netherlands, 1972.
- [27] Y. Xu, T. Minari, K. Tsukagoshi, J. A. Chroboczek, and G. Ghibaudo, *Journal of Applied Physics*, vol. 107, no. 11, article 114507, 2010.
- [28] G. Horowitz, R. Hajlaoui, D. Fichou, and A. el Kassmi, "Gate voltage dependent mobility of oligothiophene field-effect transistors," *Journal of Applied Physics*, vol. 85, no. 6, pp. 3202–3206, 1999.
- [29] W. Yi, S. Zhao, H. Sun et al., "Isomers of organic semiconductors based on dithienothiophenes: the effect of sulphur atoms positions on the intermolecular interactions and field-effect performances," *Journal of Materials Chemistry C*, vol. 3, no. 41, pp. 10856–10861, 2015.
- [30] R. K. Hallani, K. J. Thorley, A. K. Hailey, S. R. Parkin, Y. L. Loo, and J. E. Anthony, "The effect of regioisomerism on the crystal packing and device performance of desymmetrized anthradithiophenes," *Journal of Materials Chemistry C*, vol. 3, no. 34, pp. 8956–8962, 2015.
- [31] A. M. Ballantyne, L. Chen, J. Dane et al., "The effect of poly(3-hexylthiophene) molecular weight on charge transport and the performance of polymer:fullerene solar cells," *Advanced Functional Materials*, vol. 18, no. 16, pp. 2373–2380, 2008.
- [32] K. Tajima, Y. Suzuki, and K. Hashimoto, "Polymer photovoltaic devices using fully regioregular poly[(2-methoxy-5-(3',7'-dimethyloctyloxy))-1,4-phenylenevinylene]," *Journal of Physical Chemistry C*, vol. 112, no. 23, pp. 8507–8510, 2008.
- [33] P. Vanlaeke, A. Swinnen, I. Haeldermans et al., "P3HT/PCBM bulk heterojunction solar cells: relation between morphology and electro-optical characteristics," *Solar Energy Materials and Solar Cells*, vol. 90, no. 14, pp. 2150–2158, 2006.
- [34] L. M. Andersson, C. Müller, B. H. Badada, F. Zhang, U. Würfel, and O. Inganäs, "Mobility and fill factor correlation in geminate recombination limited solar cells," *Journal of Applied Physics*, vol. 110, no. 2, pp. 024509–024507, 2011.
- [35] G. Zhang, J. Yuan, P. Li et al., "Benzotrithiophene and benzodithiophene-based polymers for efficient polymer solar cells with high open-circuit voltage," *Polymer Chemistry*, vol. 4, no. 11, pp. 3390–3397, 2013.
- [36] P. P. Khlyabich, B. Burkhart, A. E. Rudenko, and B. C. Thompson, "Optimization and simplification of polymer--fullerene solar cells through polymer and active layer design," *Polymer*, vol. 54, no. 20, pp. 5267–5298, 2013.
- [37] C. B. Nielsen, B. C. Schroeder, A. Hadipour, B. P. Rand, S. E. Watkins, and I. McCulloch, "A benzotrithiophene-based low band gap polymer for polymer solar cells with high open-circuit voltage," *Journal of Materials Chemistry*, vol. 21, no. 44, pp. 17642–17645, 2011.
- [38] C. E. Small, S. W. Tsang, S. Chen et al., "Loss mechanisms in thick-film low-bandgap polymer solar cells," *Advanced Energy Materials*, vol. 3, no. 7, pp. 909–916, 2013.
- [39] W. U. Huynh, J. J. Dittmer, and A. P. Alivisatos, "Hybrid nanorod-polymer solar cells," *Science*, vol. 295, no. 5564, pp. 2425–2427, 2002.
- [40] S. D. Oosterhout, M. M. Wienk, S. S. van Bavel et al., "The effect of three-dimensional morphology on the efficiency of hybrid polymer solar cells," *Nature Materials*, vol. 8, no. 10, pp. 818–824, 2009.
- [41] P. Morvillo, E. Bobeico, S. Esposito, and R. Diana, *Energy Procedia*, vol. 31, pp. 69–73, 2012.
- [42] J. D. Kotlarski, D. J. D. Moet, and P. W. M. Blom, "Role of balanced charge carrier transport in low band gap polymer : fullerene bulk heterojunction solar cells," *Journal of Polymer Science Part B: Polymer Physics*, vol. 49, no. 10, pp. 708–711, 2011.
- [43] N. Radychev, I. Lokteva, F. Witt, J. Kolny-Olesiak, H. Borchert, and J. Parisi, "Physical origin of the impact of different nanocrystal surface modifications on the performance of CdSe/

- P3HT hybrid solar cells,” *The Journal of Physical Chemistry C*, vol. 115, no. 29, pp. 14111–14122, 2011.
- [44] M.-S. Su, C.-Y. Kuo, M.-C. Yuan, U. S. Jeng, C.-J. Su, and K.-H. Wei, “Improving device efficiency of polymer/fullerene bulk heterojunction solar cells through enhanced crystallinity and reduced grain boundaries induced by solvent additives,” *Advanced Materials*, vol. 23, no. 29, pp. 3315–3319, 2011.
- [45] C. B. Nielsen, R. S. Ashraf, B. C. Schroeder et al., “Random benzotrithiophene-based donor–acceptor copolymers for efficient organic photovoltaic devices,” *Chemical Communications*, vol. 48, no. 47, pp. 5832–5834, 2012.
- [46] C. B. Nielsen, R. S. Ashraf, N. D. Treat et al., *Advanced Materials*, vol. 27, no. 5, pp. 948–953, 2015.

## Research Article

# Study on the Phase Change Characteristics of Carbon-Based Nanofluids

Tun-Ping Teng <sup>1</sup>, Shang-Pang Yu <sup>2</sup>, Ting-Chiang Hsiao,<sup>1</sup> and Chun-Chi Chung<sup>1</sup>

<sup>1</sup>Department of Industrial Education, National Taiwan Normal University, No. 162, Sec. 1, Heping E. Road, Da'an District, Taipei City 10610, Taiwan

<sup>2</sup>Department of Mechatronic Engineering, National Taiwan Normal University, No. 162, Sec. 1, Heping E. Road, Da'an District, Taipei City 10610, Taiwan

Correspondence should be addressed to Tun-Ping Teng; tube5711@ntnu.edu.tw

Received 7 March 2018; Revised 1 May 2018; Accepted 4 June 2018; Published 8 July 2018

Academic Editor: Iftikhar Ali Sahito

Copyright © 2018 Tun-Ping Teng et al. This is an open access article distributed under the Creative Commons Attribution License, which permits unrestricted use, distribution, and reproduction in any medium, provided the original work is properly cited.

In this study, carbon-based nanofluids (CBNFs) with the minimized carbon materials (MCMs) were prepared using a graphite powder-based heating and cooling processing method (GP-HCPM). In addition, sodium dodecyl benzenesulfonate (SDBS) was added as a dispersant to enhance the stability of the CBNFs. Two methods, one involving fixed heating and cooling rates and the other involving fixed heating and cooling temperatures, were used to measure and analyze the phase change characteristics of the CBNFs and SDBS aqueous solution in order to evaluate the feasibility of employing CBNFs as phase change materials (PCMs) for cold storage applications. Results revealed that SDBS reduced the thermal conductivity ( $k$ ) and increased the viscosity ( $\mu$ ), density ( $\rho$ ), and specific heat ( $c_p$ ) of the samples; the CBNFs tended to increase the  $k$ ,  $\mu$ , and  $\rho$  values but reduce the  $c_p$  values of the samples, compared with water. Furthermore, the SDBS aqueous solution and CBNFs significantly reduced the contact angle of droplets, compared with water. Phase change experiments conducted for all samples revealed that the CBNF sample S4 demonstrated the greatest reduction ratios in onset nucleation time, solidification time, and subcooling degree (38.98%, 11.05%, and 35.41%, resp.); thus, S4 was determined to be the most suitable CBNF for use as a PCM in cold storage applications.

## 1. Introduction

Water is the most commonly used phase change material (PCM) for cold storage in ice storage air-conditioning systems, because of its low cost and substantial latent heat of freezing and melting. Ice storage air-conditioning systems work according to peak and off-peak power demand; therefore, they can be useful for power scheduling and power system optimization. Consequently, improving the performance of PCMs is a critical factor when improving the operational efficiency of ice storage air-conditioning systems [1, 2]. Before freezing, the water temperature must first reach a particular temperature below the freezing temperature. Once this temperature is reached, the temperature is stabilized at approximately 0°C and the water starts to freeze. This temperature is the nucleation temperature ( $T_n$ ) or the subcooling temperature ( $T_{sub}$ ). The subcooling degree (SD) is defined as

the difference between the freezing temperature and  $T_{sub}$ . That is, a higher  $T_{sub}$  level means a lower SD. Water must reach  $T_{sub}$  to undergo nucleation and become ice. Therefore, chillers must operate below  $T_{sub}$  to induce freezing. Furthermore,  $T_{sub}$  affects the evaporation temperature setting of a chiller; a higher evaporation temperature engenders higher chiller efficiency. Therefore, reducing the SD, nucleation time, and solidification time and elevating the latent heat of freezing are vital to improving the efficiency of ice storage air-conditioning systems.

Factors that affect the SD, nucleation time, and solidification time of a PCM include the type of nucleation (homogenous or heterogeneous), cooling rate, container surface roughness, and solid-liquid interface [3–5]. In general, heterogeneous nucleation occurs more easily than homogenous nucleation and allows the freezing process to occur at higher temperatures and with a shorter phase change time.

To avoid the aforementioned factors negatively affecting the nucleation rate and SD, researchers have proposed several methods such as adding nucleating agents or undissolved impurities [6–12], changing the size and shape of the PCMs [13–15], inputting external energy (mechanical and ultrasonic vibration) [16, 17], increasing the thermal conductivity of the PCMs [18–20], reducing the kinematic viscosity of the PCM [20–23], encapsulating the PCMs [24], and using the porous structure and network of the PCM to enhance their energy storage performance [25, 26]. Such methods can effectively suppress SD and improve the energy storage performance of PCMs. The most prevalent method is using nucleating agents to promote heterogeneous nucleation of PCMs to suppress SD and accelerate nucleation for cold storage. Nucleating agents are solid particles or crystals of materials that initiate crystallization but do not dissolve at the operational temperature. Although nucleating agents can suppress the SD of a PCM, they do not undergo a phase change during the phase change process. Therefore, nucleating agents do not contribute to the phase change heat of freezing and may reduce the freezing temperature [21, 27].

In recent years, numerous studies of carbon-based nanomaterials (CBNMs) such as nanocarbons, carbon nanotubes (CNTs), graphene (GN), and graphene oxide (GO) have been conducted, which indicate these materials have high thermal conductivity [28, 29], excellent heat transfer performance [30, 31], and low SD and freezing duration in phase change process [7–9, 11]. In addition, CBNMs have high stability and are nonperishable in liquids. Therefore, the use of CBNMs to make nanofluids and thermal applications is a worthwhile research direction. Chandrasekaran et al. [7] prepared nanofluid phase change material (NFPCM) by adding 0.1 wt.% multiwall carbon nanotubes (MWCNT) in deionized (DI) water along with pseudomonas and sodium dodecyl benzene sulfonate (SDBS) as a nucleating agent and surfactant for cold storage. The phase change experiments were carried out by isothermal bath at bath temperatures of  $-2^{\circ}\text{C}$  and  $-6^{\circ}\text{C}$  with the NFPCM. The results demonstrated that the pseudomonas eliminated the SD of the NFPCM completely and the MWCNT resulted with the reduction in the freezing duration of 25% in the case of NFPCM compared to that of water. The fraction of solidified mass revealed that 50% of phase change material (PCM) was frozen in 25% of the total freezing time for both the water and NFPCM. Li et al. [8] adopted the ultrahigh specific surface area of GN as an additive in DI water to reduce the SD of freezing water. SDBS was used to enhance the stability of the nanofluids. The phase change experiments for temperature profile and heat were conducted by isothermal bath ( $-25^{\circ}\text{C}$ ) and differential scanning calorimeter (DSC), respectively. The results showed that only the addition of 0.020 wt.% of GN was needed to completely eliminate the SD. The GN nanofluids had less SD and shorter total freezing time compared to  $\text{SiO}_2$  and  $\text{TiO}_2$  nanofluids at the same concentration. The addition of SDBS could improve suspension stability of nanofluids and further reduce the SD, but it also slightly increases the total freezing time. Liu et al. [9] prepared low concentration of GO nanosheet aqueous nanofluids without any dispersants as a PCM for cold storage. The SD of nanofluids with different

concentrations was tested experimentally in an isothermal bath at  $-15^{\circ}\text{C}$ . The results indicated that the SD could be reduced by 69.1%, and the time to start nucleation was reduced by 90.7%. Fan et al. [11] used DSC with various cooling rates to measure and analyze nonisothermal crystallization of CNT and GN nanoplatelet (GNP) aqueous nanofluids with various concentrations. The results showed that low concentration of CNTs or GNPs led to reduction of the SD up to  $5^{\circ}\text{C}$  because of the nucleating effect. The GNPs with large contact area conducted better than CNTs in facilitating heterogeneous nucleation, which greatly suppress crystal growth during the late phase of nonisothermal crystallization. However, the relatively low concentrations of CNTs nanofluids could accelerate crystallization up to nearly 37% at low cooling rate. From the above literatures, it can be known that the addition of a large specific surface area such as CNTs, GN, and GO in water has considerable benefits for reducing SD and increasing the freezing rate. However, the manufacturing costs of CNTs and GN are still quite high at present; therefore, there are still some obstacles to actually making large amounts of PCMs for cold storage.

In the present study, a graphite powder-based heating and cooling processing method (GP-HCPM) was used to produce carbon-based nanofluids (CBNFs) as PCMs. The production of CBNFs by GP-HCPM had the advantages of simple manufacturing equipment, mass and rapid production, low cost, and no need to add toxic chemical agents. Therefore, the GP-HCPM of the CBNMs and CBNFs has a relatively high applicability and scalability. The related fundamental characteristics of the CBNFs were measured and analyzed. Finally, methods involving a fixed cooling rate and fixed cooling temperature were used to conduct experiments on phase change characteristics to evaluate the feasibility of the CBNFs as PCMs for cold storage. Simultaneous use of the above two methods to evaluate the phase change characteristics will help people better understand the availability of PCMs under different cooling modes.

## 2. Freezing Nucleation Theories and Sample Preparation

*2.1. Homogeneous and Heterogeneous Nucleation.* Freezing nucleation can be divided into homogeneous nucleation and heterogeneous nucleation. The nuclei in homogeneous nucleation are uniformly present in the main phase (e.g., water). The appearance of nuclei is closely related to free energy variation. The total free energy variation of homogeneous nucleation occurs at the critical radius ( $r^*$ ) is called the critical free energy variation ( $\Delta G_{\text{ho}}^*$ ) [32–34]. When the nuclei of heterogeneous nucleation are preferentially present at the vessel surface, the undissolved particle interface, and other nonmain phase positions, it is termed heterogeneous nucleation. Most of the forms of freezing nucleation are heterogeneous nucleation. Water nucleated in a closed container or an ice-making coil is an example of heterogeneous nucleation [35]. As illustrated in Figure 1, nucleation occurs on a substrate interface and the nuclei formed are similar and hemispherical; the contact angle between the nuclei and the substrate interface on which they rest is  $\theta$ , and the change

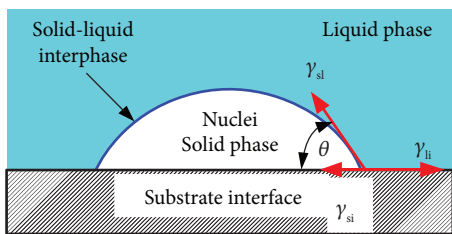


FIGURE 1: Schematic of heterogeneous nucleation.

in critical free energy when the nuclei are formed can be expressed as  $\Delta G_{he}^*$  [32].

$$\Delta G_{he}^* = \Delta G_{ho}^* \times S(\theta), \quad (1)$$

where

$$S(\theta) = \frac{[(2 + \cos \theta)(1 - \cos \theta)^2]}{4}. \quad (2)$$

When heterogeneous nucleation occurs on the substrate interface,  $S(\theta)$  is between 0 and 1. From (1) and (2), a lower  $\theta$  value of the nuclei signifies less critical free energy at heterogeneous nucleation. This geometrical effect reduces the barrier, which increases the rate of nucleation as opposed to having a surface with a higher  $\theta$  value [35, 36]. Therefore, the critical free energy required for heterogeneous nucleation is smaller than that required for homogeneous nucleation. Water is more susceptible to nucleation and icing by heterogeneous nucleation than homogeneous nucleation at the same cooling temperature.

**2.2. CBNF Preparation.** In this study, a GP-HCPM was used for producing CBNF as a PCM. The GP-HCPM process for CBNF preparation is briefly described as follows (Figure 2) [37, 38]: 5 g of graphite powder (hexagonal graphite-2H; mean size:  $3.2 \mu\text{m}$ ) was heated in a stainless steel dipper at  $600^\circ\text{C}$  using an oxygen ( $\text{O}_2$ )-acetylene ( $\text{C}_2\text{H}_2$ ) flame, and the red hot graphite powder was quickly transferred into cold water (300 ml,  $3\text{--}5^\circ\text{C}$ ) in the sample collector for cooling to produce the CBNF. In this method, graphite powder was heated at a high temperature and then rapidly cooled in cold water; a slight explosion was thus produced on the graphite powder, which crushed the graphite powder to generate minimized carbon materials (MCMs) in the water. This process can be attributed to the rapid expansion and contraction resulting from the temperature difference between the graphite and water. The CBNF was then alternately dispersed using a stirrer hot plate (PC420D, Corning, USA), ultrasonic bath (5510R-DTH, Branson, USA), homogenizer (YOM300D, Yotec, Taiwan), and ultrasonic liquid processor (Q700, Qsonica, USA) to enhance the stability (dispersion and suspension performance) of the MCMs in the CBNF. Figure 3 exhibits field emission scanning electron microscope (FESEM) and transmission electron microscope (TEM) images of the MCMs. The generated MCMs were mostly irregular and flaky in appearance. The two-dimensional size (length  $\times$  width) of these MCMs was determined using the FESEM and TEM images to be generally less than  $1 \mu\text{m}$ ; however, the thickness was less than 100 nm. Therefore, the

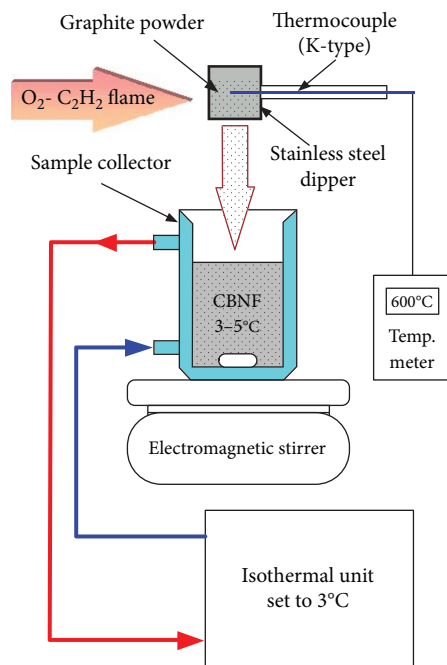


FIGURE 2: GP-HCPM process for CBNF preparation.

MCMs were considered nanomaterials. In addition, after X-ray diffraction analysis, the main components of the MCMs were determined to be hexagonal graphite-2H, amorphous carbon, and a small amount of graphene oxide.

The original CBNF was diluted with water to obtain 1.2 wt.% CBNF. 1.2 wt.% CBNF was added with different concentrations (0.06, 0.12, 0.24, 0.48, 0.96, and 1.92 wt.%) of SDBS (Sigma-Aldrich, USA) to form samples. Next, a spectrometer (V670, JASCO, Japan) was used to measure the differences in absorbance before and after the samples were left standing for 7 days to determine the optimal concentration of added SDBS. The experimental results showed that adding 0.48 wt.% SDBS to the CBNF had the best stability. A defoamer (DF, Antifoam B Silicone Emulsion, J. T. Baker, USA) at concentration of 25% of the weight of the added SDBS was used to suppress bubble formation. The determination of the concentration of the added DF was effective to suppress the foam of CBNF during stirring (stirrer was set at 400 rpm). The suspended mean particle size ( $d_p$ ) and zeta potential ( $\zeta$ ) of the CBNF were tested using a nanoparticle analyzer (SZ-100, HORIBA, Japan). The  $d_p$  and  $\zeta$  values of 1.2 wt.% MCMs in the CBNF with 0.48 wt.% SDBS were 1536.1 nm and  $-63.3$  mV, respectively. The particle size distribution of the CBNF presented a bimodal distribution with peak values of 212.8 and 6691.6 nm, with the two peak distributions accounting for 80% and 20%, respectively. However, because of the asymmetric morphology of suspended particles in liquid, using dynamic light scattering (DLS) to measure particle size usually results in overestimation of the particle size. Test results of  $\zeta$  indicate that the CBNF had excellent stability [39, 40].

The 1.2 wt.% CBNF with 0.48 wt.% SDBS solution was further diluted with water to obtain 0.3, 0.6, and 0.9 wt.% CBNFs. The MCMs:SDBS weight ratio was 5:2 (1.2:0.48)

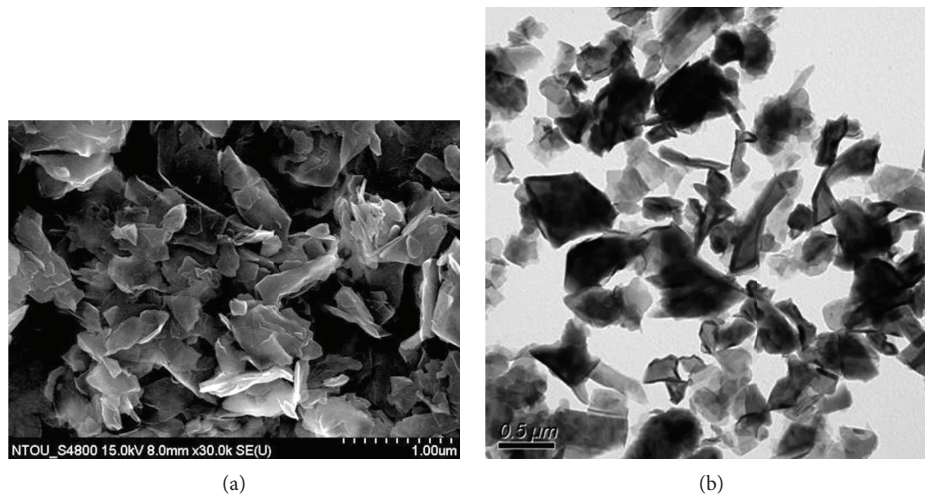


FIGURE 3: (a) FESEM and (b) TEM images of MCMs.

for all CBNFs, which demonstrated high stability and presented no observable solid-liquid separation even after undergoing static standing for over 45 days. The final experimental sample configuration is listed in Table 1. The final samples used in this experiment are used to evaluate the effect of SDBS and MCMs on the fundamental and phase change characteristic of CBNFs.

### 3. Experimental Design and Procedures

**3.1. Fundamental Characteristic Experiments.** The thermal conductivity ( $k$ ), viscosity ( $\mu$ ), and density ( $\rho$ ) of the samples were measured using a thermal property analyzer (KD-2 Pro, Decagon Devices, USA) with an accuracy of  $\pm 5.0\%$ , a resonant viscometer (VL700-T15, Hydramotion, UK) with an accuracy of  $\pm 1.0\%$ , and a liquid density meter (DA-130N, KEM, Japan) with an accuracy of  $\pm 0.001$  g/ml, respectively, in an isothermal unit (HW401L, HILES, Taiwan; accuracy:  $\pm 0.5^\circ\text{C}$ ) at  $25^\circ\text{C}$ . The handheld measuring instruments were prone to deviation due to human factors. Therefore, the experiments were repeated 10 times, and the average of the five closest values was used as the test value to reduce experimental deviation.

The specific heat ( $c_p$ ) of the samples was measured using a differential scanning calorimeter (DSC, Q20, TA, USA) with a mechanical refrigeration system (RCS40, TA, USA) in a high-purity nitrogen (5 N) atmosphere. The temperature and calorimetric accuracies of the DSC were  $\pm 0.1^\circ\text{C}$  and  $\pm 1.0\%$ , respectively. An electronic pipette (5–100  $\mu\text{l}$ ; Xplorer, Eppendorf, Germany) was used to draw a 12  $\mu\text{l}$  sample that was dripped into the sample pan (Tzero Pan: T100915), and then a precision electronic balance (0.1 mg/42 g, GR202, A&D, Japan) was used to weigh the sample. The  $c_p$  test method is a standard reference approach, and the standard reference was pure water [41]. The experimental temperature ranged from 10 to  $60^\circ\text{C}$ , and the heating rate was set at  $10^\circ\text{C}/\text{min}$ . The maximum deviation of the DSC measurement was mainly from weighing the sample. Therefore, the experiment for determining  $c_p$  was conducted five

times for each sample, and the average of the three closest results was determined to obtain the  $c_p$  value of each sample, thereby reducing the effect of measurement deviations.

Each sample's  $\theta$  was estimated by measuring a droplet of sample on the test substrate at room temperature and in ambient atmosphere using a video tensiometer (FTA188, First Ten Ångströms, UK) with an experimental deviation of less than  $1^\circ$ . Due to the addition of SDBS to the sample, the  $\theta$  value of the sample droplet was expected to be small. Therefore, the study adopted a glass substrate with a flat polyimide film tape attached on its surface to provide greater hydrophobicity in order to improve the identifiability and accuracy of the  $\theta$  experiments. The experiment for determining  $\theta$  was conducted five times for each sample, and the average of the results was determined to obtain the  $\theta$  value of each sample.

**3.2. Phase Change Experiments.** The freezing and melting of water in an ice storage air-conditioning system are often referred to as charging and discharging processes. The phase change experiment in this study was conducted using two methods, one of which entailed fixed heating and cooling rates (method 1) and the other entailed fixed heating and cooling temperatures (method 2). Method 1 was conducted using the DSC; the instrument type, sampling method, sample size, and sample pan type were the same as those used for the  $c_p$  measurement. The experimental temperature ranged from  $-25$  to  $25^\circ\text{C}$ , and the heating and cooling rate was set at  $10^\circ\text{C}/\text{min}$ . Figure 4(a) illustrates the DSC endothermic and exothermic curves for water. The melting ( $T_{\text{mp}}$ ) and solidification ( $T_{\text{sp}}$ ) peak temperatures were the melting ( $T_{\text{m}}$ ) and solidification ( $T_{\text{s}}$ ) temperatures for the discharging and charging processes, respectively. The difference between  $T_{\text{mp}}$  and  $T_{\text{sp}}$  was defined as the SD of the sample [18, 22].  $T_{\text{ms}}$  was the starting temperature for melting. The area of discharging and charging peak was calculated by the test software (Universal Analysis 2000, TA, USA) to obtain the phase change heat of melting ( $\Delta H_{\text{m}}$ ) and solidification ( $\Delta H_{\text{s}}$ ). Each sample was tested five times, and the average of the three

TABLE 1: Configuration of experimental samples.

Ingredient concentration (wt.%)	Sample name								
	Water	S1BF	S2BF	S3BF	S4BF	S1	S2	S3	S4
SDBS	0	0.12	0.24	0.36	0.48	0.12	0.24	0.36	0.48
MCMs	0	0	0	0	0	0.3	0.6	0.9	1.2

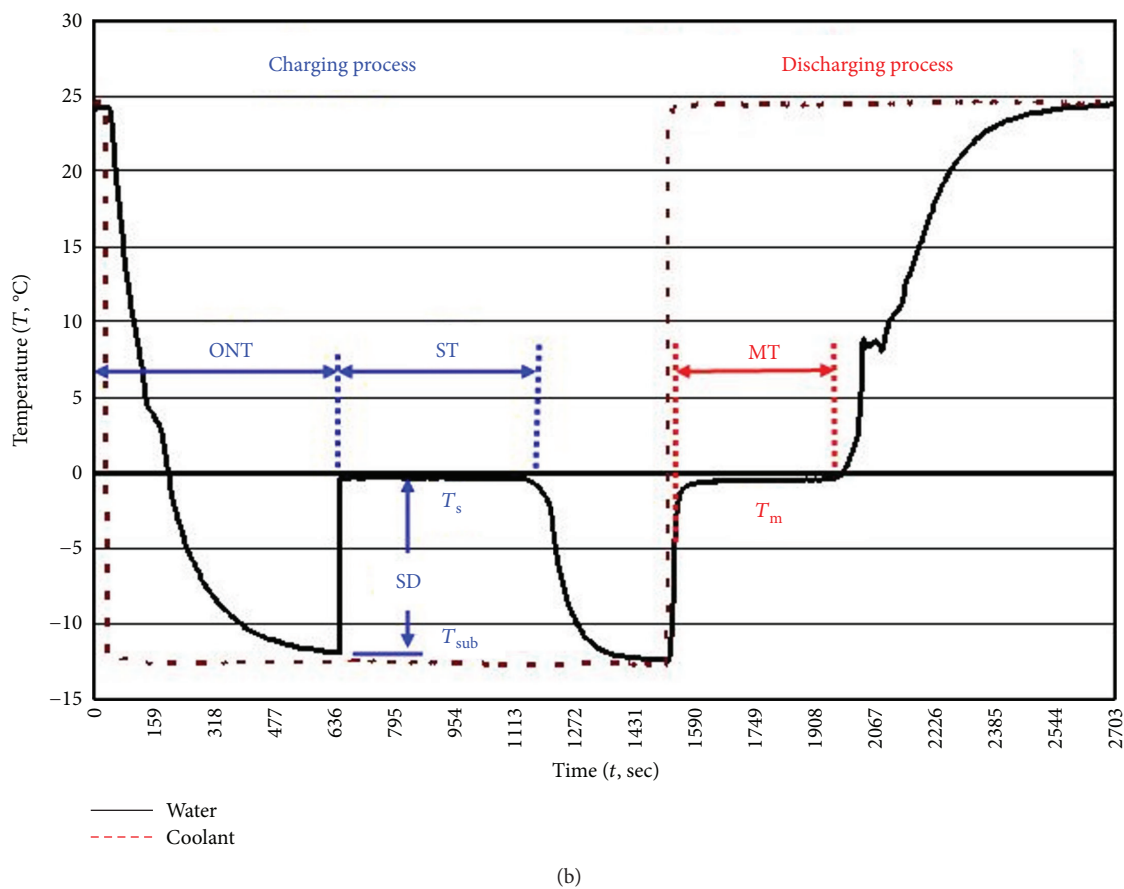
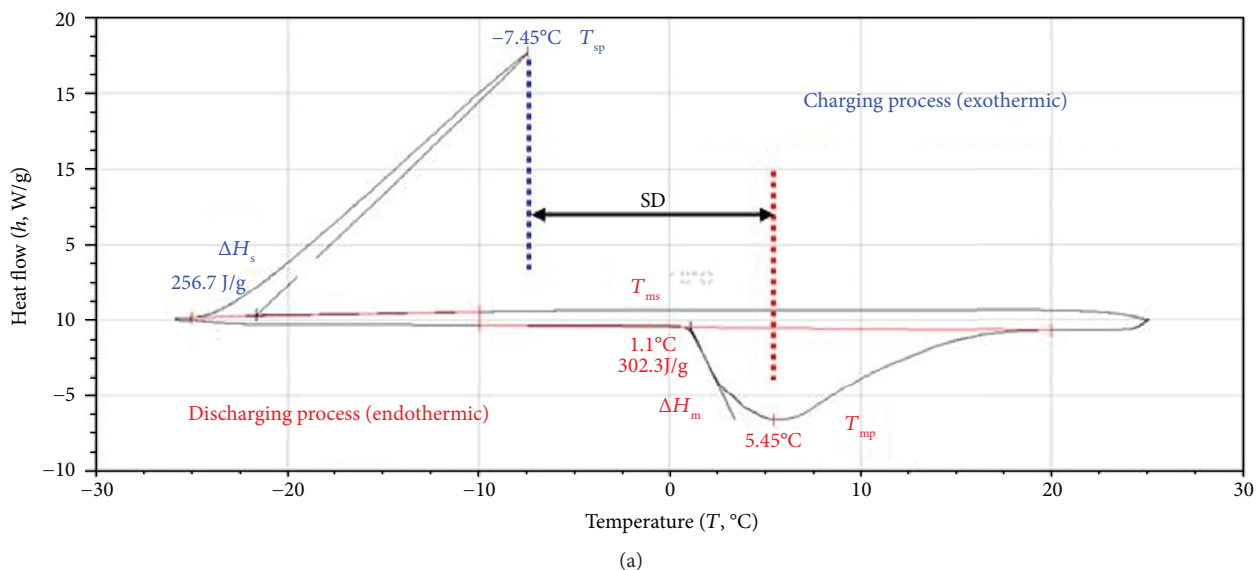


FIGURE 4: Charging and discharging curves of water obtained using (a) method 1 and (b) method 2.

TABLE 2: Results from experiments conducted on fundamental characteristics of samples.

Number	Experimental results				Change ratio (%)			
	$k$ (W/m $^{\circ}$ C)	$\mu$ (mPa s)	$\rho$ (kg/m $^3$ )	$c_p$ (kJ/kg $^{\circ}$ C)	$CR_k$	$CR_{\mu}$	$CR_{\rho}$	$CR_{c_p}$
Water	0.606	0.88	997.16	4.183	—	—	—	—
S1BF	0.594	0.90	997.58	4.194	-1.93	1.89	0.04	0.26
S2BF	0.584	0.92	998.38	4.207	-3.58	3.77	0.12	0.58
S3BF	0.581	0.93	999.04	4.224	-4.11	5.66	0.19	0.99
S4BF	0.579	0.95	999.08	4.242	-4.49	7.55	0.19	1.42
S1	0.596	0.93	999.46	4.181	-1.73	5.66	0.23	-0.06
S2	0.598	0.95	1001.50	4.178	-1.31	7.55	0.44	-0.12
S3	0.601	1.00	1003.90	4.164	-0.82	13.21	0.68	-0.44
S4	0.616	1.02	1005.10	4.145	1.62	15.09	0.80	-0.92

closest results (referred to as solidification heat) was determined to obtain the test result of the phase change experiments for the DSC.

Method 2 was performed using two isothermal units set at  $-12$  and  $25^{\circ}\text{C}$ . In this method, 12 ml of the sample was loaded in a polypropylene (PP) test tube (capacity specification: 15 ml). A T-type thermocouple (accuracy:  $\pm 0.75\%$  or  $\pm 0.5^{\circ}\text{C}$ ) with a stainless steel protective tube (outer diameter: 0.6 mm) was installed in the center of the PP test tube, and the contact location between the thermocouple and the lid of the PP test tube was fixed using epoxy. A 0.8 mm hole was made in the lid of the PP test tube to ensure pressure stability inside and outside. First, the sample was placed in an isothermal unit (P-20, YSC, Taiwan; accuracy:  $\pm 0.5^{\circ}\text{C}$ ) at  $25^{\circ}\text{C}$  to maintain the initial temperature of the sample at  $25 \pm 0.5^{\circ}\text{C}$ ; subsequently, the sample was transferred to another isothermal unit (TC-650SD, Brookfield, USA; accuracy:  $\pm 0.5^{\circ}\text{C}$ ) at  $-12^{\circ}\text{C}$  for the charging process. After the charging process was completed, the sample was relocated to an isothermal unit at  $25^{\circ}\text{C}$  for the discharging process. Once the sample reached  $25 \pm 0.5^{\circ}\text{C}$ , the discharging process was completed. Temperature data of the phase change experiment for each sample were recorded using a data recorder (TRM-20, TOHO, Japan; accuracy:  $\pm 0.1\%$ ) at a sampling rate of 1.0 s. Figure 4(b) illustrates the charging and discharging process curves for water determined using method 2. As shown in Figure 4(b), the time from the original temperature ( $25^{\circ}\text{C}$ ) to  $T_{\text{sub}}$ , the time from  $T_{\text{sub}}$  to the end of freezing, and the time from the start to the end of melting were referred to as the onset nucleation time (ONT), the solidification time (ST), and the melting time (MT), respectively. SD was defined as the difference between  $T_s$  and the  $T_{\text{sub}}$ . This experiment was conducted six times for each sample, and the average of the results was determined to obtain the phase change characteristics for each sample.

**3.3. Data and Uncertainty Analysis.** The experimental results are presented as a change ratio (CR) to reveal the differences between the experimental results of water ( $D_w$ ) and those of the other samples ( $D_{ts}$ ); CR can be expressed as

$$CR = \left[ \frac{D_{ts} - D_w}{D_w} \right] \times 100\%. \quad (3)$$

Uncertainty analysis entailed calculating deviations in the measurements. The uncertainty ranges determined for the fundamental characteristics of the samples, such as  $k$ ,  $\mu$ ,  $\rho$ ,  $c_p$ , and  $\theta$ , refer to deviations from the relevant measuring instruments and temperature controller. According to standard uncertainty analysis [42], the maximum uncertainty ranges for  $k$ ,  $\mu$ ,  $\rho$ ,  $c_p$ , and  $\theta$  were within  $\pm 5.39\%$ ,  $\pm 2.24\%$ ,  $\pm 2.00\%$ ,  $\pm 1.47\%$ , and  $\pm 3.57\%$ , respectively. The temperature and calorimetric deviations of the phase change experiment conducted using the DSC were  $\pm 0.1^{\circ}\text{C}$  and  $\pm 1.0\%$ , respectively. Use of isothermal units for the phase change experiments required consideration of deviations resulting from the data recorder, thermocouple, and temperature controller; therefore, the maximum deviation was  $\pm 2.14\%$ .

The temperature and calorimetric accuracies of the DSC were  $\pm 0.1^{\circ}\text{C}$  and  $\pm 1.0\%$ , respectively.

## 4. Results and Discussions

Table 2 presents experimentally derived  $k$ ,  $\mu$ ,  $\rho$ , and  $c_p$  values of the samples. Regarding the measured  $k$  values of the samples, the results revealed that adding SDBS to water engendered a reduction in the  $k$  value of the water; moreover, the reduction ratio of  $k$  was proportional to the SDBS concentration. However, adding MCMs of different concentrations to each base fluid (SDBS aqueous solution) tended to engender an increase in the  $k$  values of the samples. The 0.48 wt.% SDBS aqueous solution with 1.2 wt.% MCMs (S4) increased  $k$  by 1.62%, compared with water. These experimental results demonstrate that although adding SDBS can improve the stability of a CBNF, it does not help to improve the  $k$  value of the CBNF. However, the paramount performance index for a CBNF in energy storage applications is heat exchange. Therefore, considering the long-term useful life and feasibility of a CBNF, adding a dispersant is imperative. Moreover,  $k$  is only one of the factors influencing heat transfer performance. In an actual heat exchange system, increasing the  $k$  value of the working fluid has little effect on heat transfer performance.

Regarding the measured  $\mu$  values of the samples, the results revealed that adding SDBS and MCMs to the base fluid increased the  $\mu$  value of the base fluid; additionally,

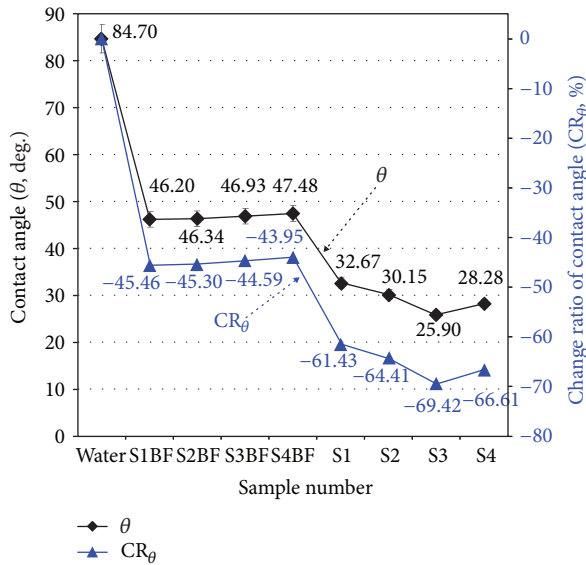


FIGURE 5: Average value and CR of  $\theta$  of each sample droplet.

the increase ratio of  $\mu$  was proportional to the concentration of SDBS and MCMs. A CBNF belongs to a solid-liquid mixture. In general, a nanofluid has a higher  $\mu$  value than that of a base fluid, and the increase ratio of  $\mu$  is related to the particle size of the additives, solid-liquid interface characteristics, and stability. The 0.48 wt.% SDBS aqueous solution with 1.2 wt.% MCMs (S4) increased the  $\mu$  value by 15.09%, compared with water.

Regarding the measured  $\rho$  and  $c_p$  values of the samples, the results showed that adding SDBS and MCMs to the base fluid increased the  $\rho$  value of the base fluid; moreover, the increase ratio of  $\rho$  was proportional to the concentration of SDBS and MCMs. However, adding SDBS to water slightly increased the  $c_p$  value of the water, whereas adding MCMs slightly reduced the  $c_p$  value of the base fluid. MCMs are carbon-based materials and have higher  $\rho$  and lower  $c_p$  values than those of water. According to the concept underlying a solid-liquid mixture, adding MCMs to water increases and reduces the  $\rho$  and  $c_p$  values of the water, respectively. Due to the low concentration of SDBS and MCMs in this study, the effect on the  $\rho$  and  $c_p$  values of the CBNF was not significant (the variation was within the uncertainty of the experiment). The 0.48 wt.% SDBS aqueous solution with 1.2 wt.% MCMs (S4) changed the  $\rho$  and  $c_p$  values by 0.80% and  $-0.92\%$ , respectively, compared with water. The results of the experiments on the fundamental sample characteristics confirm that adding SDBS reduced the  $k$  value and increase the  $\mu$ ,  $\rho$ , and  $c_p$  values of the samples, whereas adding the CBNFs tended to increase the  $k$ ,  $\mu$ , and  $\rho$  values and reduce the  $c_p$  value of the samples, compared with water.

Figure 5 illustrates the average and CR of  $\theta$  for each sample droplet. As indicated in this figure, adding SDBS to water significantly reduced the  $\theta$  values of the sample droplets, and adding MCMs to the SDBS aqueous solution further reduced the  $\theta$  values of the sample droplets. The  $\theta$  values of S1BF, S2BF, S3BF, S4BF, S1, S2, S3, and S4 were lower than

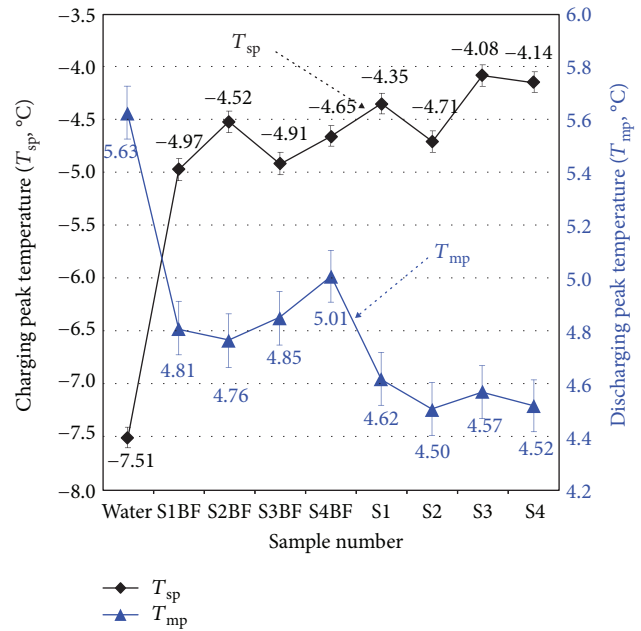


FIGURE 6:  $T_{sp}$  and  $T_{mp}$  for each sample in the experiment conducted using method 1.

those of water by 45.46%, 45.30%, 44.59%, 43.95%, 61.43%, 64.41%, 69.42%, and 66.61%, respectively. In addition, the influence of SDBS concentration on  $\theta$  was less clear, compared with that of CBNF concentration. According to the aforementioned heterogeneous nucleation theory ((1) and (2)), the low  $\theta$  values of the sample droplets contributed to the occurrence of freezing nucleation, facilitating PCM freezing [32, 35, 36].

Figure 6 shows the  $T_{sp}$  and  $T_{mp}$  values obtained for each sample in the experiment conducted using method 1. Adding SDBS to water increased the  $T_{sp}$  value of the water, and adding MCMs to the SDBS aqueous solution further enhanced the  $T_{sp}$  value of the water. Although the experimental data presented a beating condition, the overall trend demonstrated an increase in  $T_{sp}$  with increasing SDBS and MCM concentrations.  $T_{mp}$  tended to gradually increase with SDBS concentration, whereas  $T_{mp}$  tended to decrease gradually with increased MCM concentration. However, the  $T_{mp}$  values of the aqueous SDBS and CBNF were lower than that of water throughout the experiments. A high  $T_{sp}$  helps to increase the temperature difference between the coolant of a chiller and the PCM at a fixed evaporation temperature to shorten the freezing time or enhance heat transfer capacity. A low  $T_{mp}$  provides a lower coolant temperature for the discharging process, thus engendering a higher temperature difference between the air-conditioning load and the coolant to increase the heat transfer capacity of the heat exchanger (fan coil units). Compared with water, the highest increase in  $T_{sp}$  was observed for S3 (3.43°C) and the highest reduction in  $T_{mp}$  was observed for S2 (1.12°C). The presented experimental results reveal that the  $T_{sp}$  and  $T_{mp}$  values of water were not near 0°C mainly because of the cooling and heating rates of the DSC. Cooling and heating rates affect the phase change condition; low heating and cooling rates result in water  $T_{sp}$

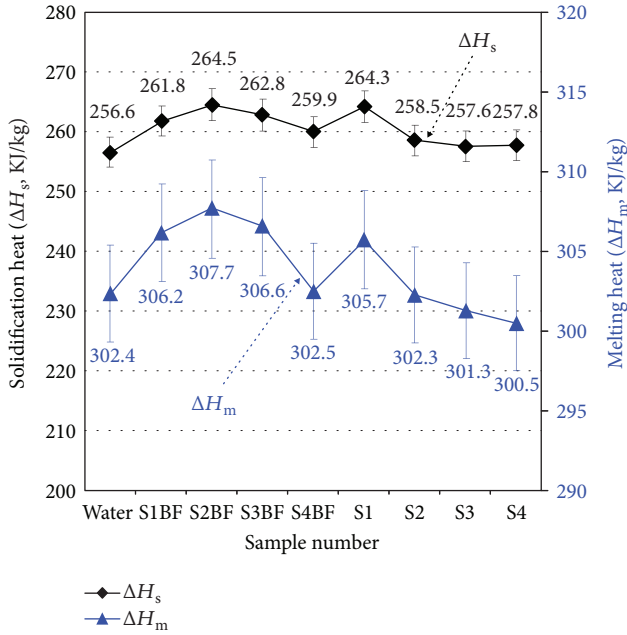


FIGURE 7:  $\Delta H_s$  and  $\Delta H_m$  for each sample in the experiment conducted using method 1.

and  $T_{mp}$  values closer to  $0^\circ\text{C}$ . However, excessively low cooling and heating rates result in longer measurement times that in turn lead to more severe sample weight loss and pressure changes within the sample pan, which can also cause measurement deviations. Therefore, in the present study, higher heating and cooling rates were used to conduct the DSC experiments to ensure relatively accurate measurements. A comparison of the relative differences between the various samples was made under the same experimental conditions.

Figure 7 displays the  $\Delta H_s$  and  $\Delta H_m$  values for each sample in the experiment conducted using method 1, indicating similar trends of  $\Delta H_s$  and  $\Delta H_m$ . The  $\Delta H_s$  and  $\Delta H_m$  values increased and then decreased as the SDBS concentration increased; moreover, the values decreased as the MCM concentration increased. Overall, adding a small amount of SDBS (within 0.24 wt.%) to water slightly increased the  $\Delta H_s$  and  $\Delta H_m$  values of the water.  $\Delta H_s$  less than  $\Delta H_m$  are mainly affected by the perfect degree of freezing crystallization of the samples, which is primarily influenced by the DSC cooling rates. PCMs with higher phase change heat can increase thermal storage density and thus reduce the volume of the thermal storage tank required under the same thermal storage capacity. However, in this study, the differences in phase change heat among all samples were not significant; the CR values of  $\Delta H_s$  and  $\Delta H_m$  relative to water were 0.39%–3.08% and  $-0.03\%$ – $-1.75\%$ , respectively. Therefore, all study samples would not be able to significantly contribute to increasing thermal storage density and reducing the volume of the thermal storage tank in an ice storage air-conditioning system.

Figure 8 illustrates the  $T_s$  and  $T_m$  values obtained for each sample in the experiment conducted using method 2, demonstrating similar variation trends for  $T_s$  and  $T_m$ . Adding SDBS to water led to an increase in  $T_s$  and  $T_m$ , which then decreased as the SDBS concentration increased;

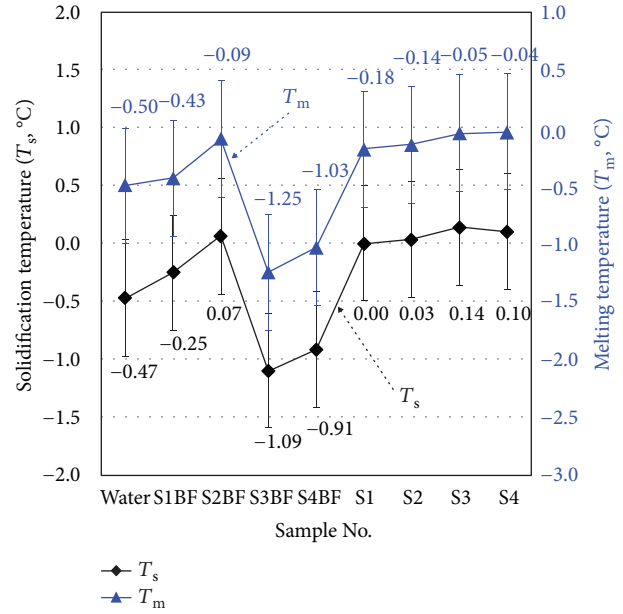


FIGURE 8:  $T_s$  and  $T_m$  for each sample in the experiment conducted using method 2.

furthermore, adding MCMs to the SDBS aqueous solution induced a gradual increase in  $T_s$  and  $T_m$  as the MCM concentration increased. As mentioned ( $T_{sp}$  and  $T_{mp}$ ), high  $T_s$  and low  $T_m$  contribute to the operational performance of ice storage air-conditioning systems. However, in this study, the applied SDBS aqueous solution and CBNFs had no significant effect on  $T_s$  and  $T_m$ , and the largest difference relative to water was only  $0.75^\circ\text{C}$ . Therefore, the SDBS aqueous solution and CBNFs would not significantly contribute to the operational performance of an ice storage air-conditioning system.

Figure 9 demonstrates the ONT, ST, and MT values for each sample in method 2. Adding SDBS and MCMs to water shortened the observed ONT of the water, but the reduction rate was not significantly related to the SDBS or MCM concentration. The highest reduction in ONT was observed for S4 (38.98%), compared with water. The reduction in the water ONT after SDBS and MCM addition was mainly due to the decrease in SD that resulted in a shorter ice nucleation time. However, adding SDBS and MCMs to water did not necessarily shorten the water ST and MT, and the CR values of ST and MT were  $-11.05\%$  (S4)– $-1.39\%$  (S2BF) and  $-10.05\%$  (S1)– $-5.39\%$  (S3BF), compared with water. Shorter ST and MT can improve the charging efficiency and respond to the air-conditioning load capacity, respectively. The S4 and S1 samples had the highest ST and MT reduction ratios (11.05% and 10.05%, resp.) when compared with water.

Figure 10 displays the SD for each sample in method 1 and method 2. The SD values obtained from the experiments conducted using method 1 and method 2 differed considerably, but the two methods exhibited similar trends. The difference between the SD values can be primarily attributed to differences in the cooling rate. However, the SD values obtained through method 1 and method 2 both indicate that adding SDBS and MCMs to water reduced the SD

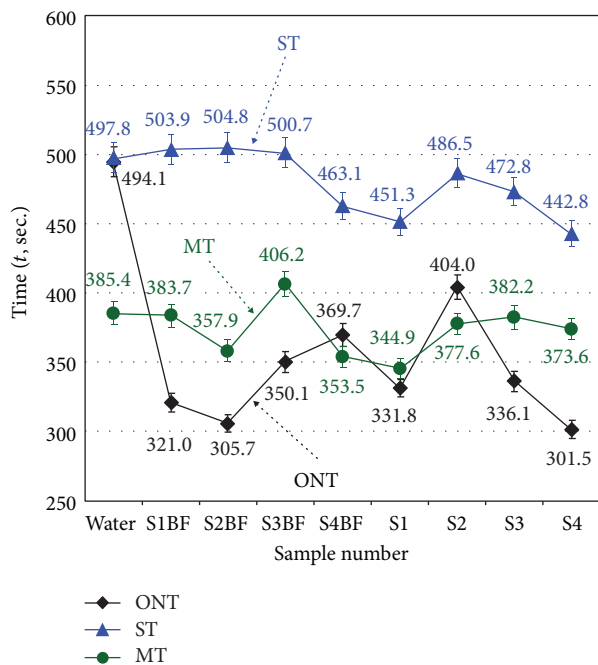


FIGURE 9: ONT, ST, and MT for each sample in the experiment conducted using method 2.

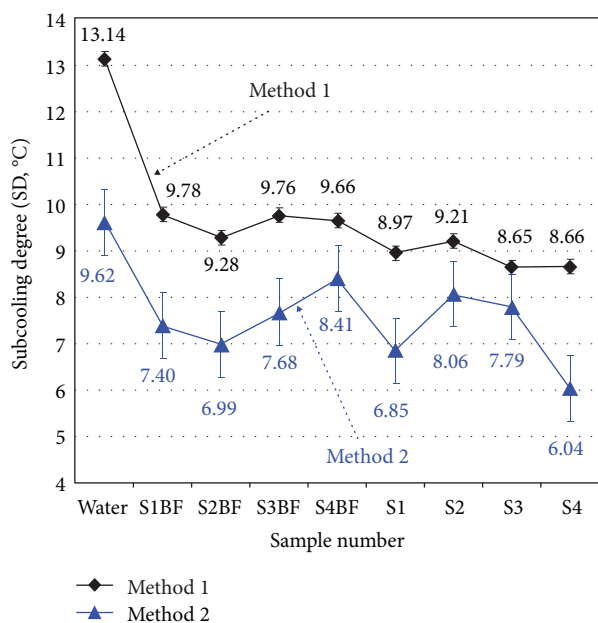


FIGURE 10: SD for each sample in the experiments conducted using both methods.

value of the water. This phenomenon is a result of three major factors:

- (1) Adding SDBS and MCMs to water reduced the  $\theta$  of the water between the sample and the substrate (increasing the wettability of the interface) and contribute to freezing nucleation [6, 12, 35, 36].

- (2) MCMs act as nucleating agents.

- (3) SDBS provides better suspension and dispersion performance for MCMs in water, which facilitates the transmission of energy to enhance the freezing phase change of CBNFs.

In both method 1 and method 2, S3 and S4 had the lowest SD ( $-34.18\%$  and  $-37.23\%$ , resp.), compared with water. According to the average of the two test methods, the SD values of S1BF, S2BF, S3BF, S4BF, S1, S2, S3, and S4 were lower than those of water by 24.50% ( $2.79^\circ\text{C}$ ), 28.47% ( $3.24^\circ\text{C}$ ), 23.34% ( $2.66^\circ\text{C}$ ), 20.57% ( $2.34^\circ\text{C}$ ), 30.49% ( $3.47^\circ\text{C}$ ), 24.10% ( $2.74^\circ\text{C}$ ), 27.76% ( $3.16^\circ\text{C}$ ), and 35.41% ( $4.03^\circ\text{C}$ ), respectively. Based on the SD results obtained from the experiments conducted using method 1 and method 2, S4 demonstrated optimal SD suppression. According to the  $\theta$  measurement results (Figure 6), the  $\theta$  values of the CBNFs (S1–S4) were lower than those of the SDBS aqueous solution (S1BF–S4BF). However, not all CBNF samples had lower SD values than those of the SDBS aqueous solution. Such a finding can be attributed to the influence of particle size distribution and the stability of MCMs in CBNFs. The particle size distribution of MCMs is relatively broad when determined using both electron microscope images and DLS. Smaller specific surface areas of larger or aggregated MCMs provide a less heterogeneous nucleation interface area. In addition, large MCMs or aggregated MCMs are less stable and provide a relatively lower contribution to energy transfer. The interface effects and combination between water, SDBS, and MCMs are also crucial factors influencing the SD characteristics of CBNFs. The aforementioned factors affected the SD value of each sample to varying degrees. Overall, the effect of SD on the CBNFs was greater than that on the SDBS aqueous solution.

Based on the results, the ONT, ST, MT, and SD values of all CBNFs were significantly different from those of water, and ONT had a strong correlation with SD. In general, as a chiller's evaporation temperature increases by  $1^\circ\text{C}$ , its power consumption decreases by 3%–5%. Therefore, a low SD value helps improve the evaporation temperature of a chiller, thus considerably improving the chiller's operating efficiency. From the presented results, this study determined S4 to be the most suitable sample for use as a PCM in ice storage air-conditioning systems.

Figure 11 depicts a photograph of the four different concentrations of CBNF samples after 20 phase change experiments (method 2), revealing the stability of the CBNFs. Sedimentation from solid-liquid separation could not be observed even after the CBNFs underwent 20 repetitions of the charging and discharging processes. Therefore, the CBNFs in this study had considerable stability as a PCM for cold storage application.

## 5. Conclusion

CBNFs were prepared using a GP-HCPM, and SDBS was added as a dispersant to enhance the stability of the CBNFs. The fundamental characteristics of the CBNFs, suspended CBNMs, and SDBS aqueous solution were examined. Two

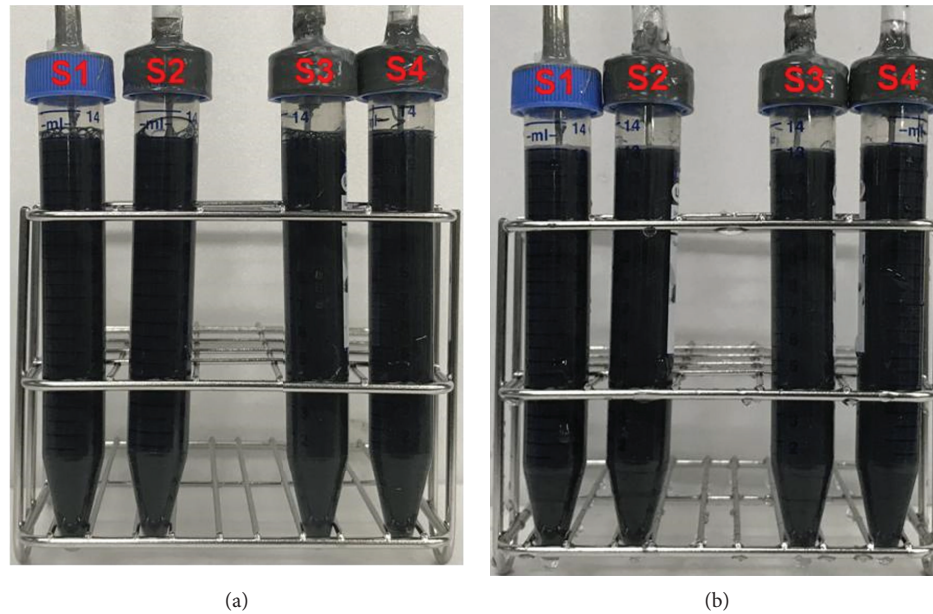


FIGURE 11: Photographs of the CBNF for (a) initial and (b) after undergoing 20 phase change experiments.

methods, one involving a fixed heating and cooling rate and the other involving a fixed heating and cooling temperature, were used to evaluate the feasibility of the CBNFs as PCMs for cold storage applications. The primary findings of this study are outlined as follows:

- (1) The SDBS aqueous solution reduced the  $k$  values and increased the  $\mu$ ,  $\rho$ , and  $c_p$  values of the samples, and the CBNFs tended to increase the  $k$ ,  $\mu$ , and  $\rho$  values of the samples but tended to reduce the  $c_p$  values of the samples, compared with water. In all the test samples, the  $k$ ,  $\mu$ , and  $\rho$  of S4 had the maximum increase ratio of 1.62, 15.09, 0.80%, and  $c_p$  of S4 had the maximum decrease ratio of 0.92% that compared with water.
- (2) The SDBS aqueous solution and CBNFs significantly reduced  $\theta$ . The  $\theta$  of SDBS aqueous solution and CBNFs had the maximum decrease ratio of 45.46% (S1BF) and 69.42% (S3), compared with water.
- (3) The CBNFs significantly reduced the ONT, ST, MT, and SD values, compared with water.
- (4) The highest reductions in ONT, ST, and SD were observed for S4 (38.98%, 11.05%, and 35.41%, resp.), compared with water.
- (5) The CBNF sample S4 had the lowest ONT, ST, and SD of all the samples in the phase change experiments; thus, S4 was determined to be the most suitable CBNF for use as a PCM for cold storage applications.

### Data Availability

The data used to support the findings of this study are available from the corresponding author upon request.

### Conflicts of Interest

The authors declare that they have no competing interests.

### Acknowledgments

The authors would like to thank the Ministry of Science and Technology of Republic of China (Taiwan) for their financial support to this research under Contract nos. MOST 104-2221-E-003-019-MY2 and MOST 106-2221-E-003-021-MY3.

### References

- [1] Z. Kang, R. Wang, X. Zhou, and G. Feng, "Research status of ice-storage air-conditioning system," *Procedia Engineering*, vol. 205, pp. 1741–1747, 2017.
- [2] B. Parsons, *Design Guide for Cool Thermal Storage*, ASHRAE, Atlanta, GA, Georgia, 1993.
- [3] M. Faucheux, G. Muller, M. Havet, and A. LeBail, "Influence of surface roughness on the supercooling degree: case of selected water/ethanol solutions frozen on aluminium surfaces," *International Journal of Refrigeration*, vol. 29, no. 7, pp. 1218–1224, 2006.
- [4] M. Keinänen, "Latent heat recovery from supercooled sodium acetate trihydrate using a brush heat exchanger, M.S. thesis," Department of Mechanical Engineering, Helsinki University of Technology, Finland, Europe, 2007.
- [5] A. Safari, R. Saidur, F. A. Sulaiman, Y. Xu, and J. Dong, "A review on supercooling of phase change materials in thermal energy storage systems," *Renewable and Sustainable Energy Reviews*, vol. 70, pp. 905–919, 2017.
- [6] S. Wu, D. Zhu, X. Li, H. Li, and J. Lei, "Thermal energy storage behavior of  $\text{Al}_2\text{O}_3\text{-H}_2\text{O}$  nanofluids," *Thermochimica Acta*, vol. 483, no. 1-2, pp. 73–77, 2009.
- [7] P. Chandrasekaran, M. Cheralathan, V. Kumaresan, and R. Velraj, "Solidification behavior of water based nanofluid

- phase change material with a nucleating agent for cool thermal storage system,” *International Journal of Refrigeration*, vol. 41, pp. 157–163, 2014.
- [8] X. Li, Y. Chen, Z. Cheng, L. Jia, S. Mo, and Z. Liu, “Ultra-high specific surface area of graphene for eliminating subcooling of water,” *Applied Energy*, vol. 130, pp. 824–829, 2014.
- [9] Y. Liu, X. Li, P. Hu, and G. Hu, “Study on the supercooling degree and nucleation behavior of water-based graphene oxide nanofluids PCM,” *International Journal of Refrigeration*, vol. 50, pp. 80–86, 2015.
- [10] A. A. Altohamy, M. F. Abd Rabbo, R. Y. Sakr, and A. A. Attia, “Effect of water based  $Al_2O_3$  nanoparticle PCM on cool storage performance,” *Applied Thermal Engineering*, vol. 84, pp. 331–338, 2015.
- [11] L.-W. Fan, X.-L. Yao, X. Wang et al., “Non-isothermal crystallization of aqueous nanofluids with high aspect-ratio carbon nano-additives for cold thermal energy storage,” *Applied Energy*, vol. 138, pp. 193–201, 2015.
- [12] L. Jia, L. Peng, Y. Chen, S. Mo, and X. Li, “Improving the supercooling degree of titanium dioxide nanofluids with sodium dodecylsulfate,” *Applied Energy*, vol. 124, pp. 248–255, 2014.
- [13] T. Oya, T. Nomura, N. Okinaka, and T. Akiyama, “Phase change composite based on porous nickel and erythritol,” *Applied Thermal Engineering*, vol. 40, pp. 373–377, 2012.
- [14] P. Chandrasekaran, M. Cheralathan, V. Kumaresan, and R. Velraj, “Enhanced heat transfer characteristics of water based copper oxide nanofluid PCM (phase change material) in a spherical capsule during solidification for energy efficient cool thermal storage system,” *Energy*, vol. 72, pp. 636–642, 2014.
- [15] X. Zhang, X. Chen, Z. Han, and W. Xu, “Study on phase change interface for erythritol with nano-copper in spherical container during heat transport,” *International Journal of Heat and Mass Transfer*, vol. 92, pp. 490–496, 2016.
- [16] E. P. Ona, X. Zhang, S. Ozawa et al., “Influence of ultrasonic irradiation on the solidification behavior of erythritol as a PCM,” *Journal of Chemical Engineering of Japan*, vol. 35, no. 3, pp. 290–298, 2002.
- [17] E. P. Ona, S. Ozawa, Y. Kojima et al., “Effect of ultrasonic irradiation parameters on the supercooling relaxation behavior of PCM,” *Journal of Chemical Engineering of Japan*, vol. 36, no. 7, pp. 799–805, 2003.
- [18] U. Stritih, “An experimental study of enhanced heat transfer in rectangular PCM thermal storage,” *International Journal of Heat and Mass Transfer*, vol. 47, no. 12-13, pp. 2841–2847, 2004.
- [19] J. M. Khodadadi, L. Fan, and H. Babaei, “Thermal conductivity enhancement of nanostructure-based colloidal suspensions utilized as phase change materials for thermal energy storage: a review,” *Renewable and Sustainable Energy Reviews*, vol. 24, pp. 418–444, 2013.
- [20] V. Kumaresan, P. Chandrasekaran, M. Nanda, A. K. Maini, and R. Velraj, “Role of PCM based nanofluids for energy efficient cool thermal storage system,” *International Journal of Refrigeration*, vol. 36, no. 6, pp. 1641–1647, 2013.
- [21] S. Harikrishnan, S. Magesh, and S. Kalaiselvam, “Preparation and thermal energy storage behaviour of stearic acid- $TiO_2$  nanofluids as a phase change material for solar heating systems,” *Thermochimica Acta*, vol. 565, pp. 137–145, 2013.
- [22] A. Zabalegui, D. Lokapur, and H. Lee, “Nanofluid PCMs for thermal energy storage: latent heat reduction mechanisms and a numerical study of effective thermal storage performance,” *International Journal of Heat and Mass Transfer*, vol. 78, pp. 1145–1154, 2014.
- [23] X. Zhang, J. Niu, S. Zhang, and J. Y. Wu, “PCM in water emulsions: supercooling reduction effects of nano-additives, viscosity effects of surfactants and stability,” *Advanced Engineering Materials*, vol. 17, no. 2, pp. 181–188, 2015.
- [24] R. Al-Shannaq, J. Kurdi, S. Al-Muhtaseb, M. Dickinson, and M. Farid, “Supercooling elimination of phase change materials (PCMs) microcapsules,” *Energy*, vol. 87, pp. 654–662, 2015.
- [25] S. I. Golestaneh, A. Mosallanejad, G. Karimi, M. Khorram, and M. Khashi, “Fabrication and characterization of phase change material composite fibers with wide phase-transition temperature range by coelectrospinning method,” *Applied Energy*, vol. 182, pp. 409–417, 2016.
- [26] C.-S. Heu, S.-W. Kim, K.-S. Lee, and D.-R. Kim, “Fabrication of three-dimensional metal-graphene network phase change composite for high thermal conductivity and suppressed subcooling phenomena,” *Energy Conversion and Management*, vol. 149, pp. 608–615, 2017.
- [27] M. M. Farid, A. M. Khudhair, S. A. K. Razack, and S. Al-Hallaj, “A review on phase change energy storage: materials and applications,” *Energy Conversion and Management*, vol. 45, no. 9-10, pp. 1597–1615, 2004.
- [28] F.-C. Li, J.-C. Yang, W.-W. Zhou, Y. R. He, Y. M. Huang, and B. C. Jiang, “Experimental study on the characteristics of thermal conductivity and shear viscosity of viscoelastic-fluid-based nanofluids containing multiwalled carbon nanotubes,” *Thermochimica Acta*, vol. 556, pp. 47–53, 2013.
- [29] M. Soltanimehr and M. Afrand, “Thermal conductivity enhancement of COOH-functionalized MWCNTs/ethylene glycol-water nanofluid for application in heating and cooling systems,” *Applied Thermal Engineering*, vol. 105, pp. 716–723, 2016.
- [30] D. Huang, Z. Wu, and B. Sunden, “Effects of hybrid nanofluid mixture in plate heat exchangers,” *Experimental Thermal and Fluid Science*, vol. 72, pp. 190–196, 2016.
- [31] Y.-H. Hung, W.-P. Wang, Y.-C. Hsu, and T.-P. Teng, “Performance evaluation of an air-cooled heat exchange system for hybrid nanofluids,” *Experimental Thermal and Fluid Science*, vol. 81, pp. 43–55, 2017.
- [32] R. P. Sear, “Nucleation: theory and applications to protein solutions and colloidal suspensions,” *Journal of Physics: Condensed Matter*, vol. 19, no. 3, article 033101, 2007.
- [33] X.-J. Wang, X. F. Li, Y. H. Xu, and D. S. Zhu, “Thermal energy storage characteristics of Cu- $H_2O$  nanofluids,” *Energy*, vol. 78, pp. 212–217, 2014.
- [34] E. Günther, L. Huang, H. Mehling, and C. Dötsch, “Subcooling in PCM emulsions- part 2: interpretation in terms of nucleation theory,” *Thermochimica Acta*, vol. 522, no. 1-2, pp. 199–204, 2011.
- [35] R. P. Sear, “Quantitative studies of crystal nucleation at constant supersaturation: experimental data and models,” *CrystEngComm*, vol. 16, no. 29, pp. 6506–6522, 2014.
- [36] C. A. Sholl and N. H. Fletcher, “Decoration criteria for surface steps,” *Acta Metallurgica*, vol. 18, no. 10, pp. 1083–1086, 1970.
- [37] T.-P. Teng, J.-Y. Li, and W.-P. Wang, “Preparation and characterization of carbon-based nanofluid through a heating and cooling processing method,” in *Asian Conference on Engineering and Natural Sciences (ACENS 2016)*, pp. 150–159, Fukuoka, Japan, February 2016, ID: ACENS-8908.

- [38] T.-C. Hsiao, T.-P. Teng, J.-Y. Li, and C.-Y. Yu, "Effect of temperature on the characteristic of carbon-based nanofluid," in *Tokyo 14th International Conference on Engineering & Technology, Computer, Basic & Applied Sciences (ECBA-2017)*, Tokyo, Japan, March 2017ID: TKE-537-102.
- [39] R. Greenwood and K. Kendall, "Selection of suitable dispersants for aqueous suspensions of zirconia and titania powders using acoustophoresis," *Journal of the European Ceramic Society*, vol. 19, no. 4, pp. 479–488, 1999.
- [40] D. Hanaor, M. Michelazzi, C. Leonelli, and C. C. Sorrell, "The effects of carboxylic acids on the aqueous dispersion and electrophoretic deposition of  $ZrO_2$ ," *Journal of the European Ceramic Society*, vol. 32, no. 1, pp. 235–244, 2012.
- [41] ASHRAE, "Chapter 30 Thermophysical properties of refrigerants," in *ASHRAE Handbook-Fundamentals (SI)*, pp. 30.1–30.75, ASHRAE, Atlanta, GA, Georgia, 2009.
- [42] H.-M. Nieh, T.-P. Teng, and C.-C. Yu, "Enhanced heat dissipation of a radiator using oxide nano-coolant," *International Journal of Thermal Sciences*, vol. 77, pp. 252–261, 2014.

## Research Article

# Hole Transport Behaviour of Various Polymers and Their Application to Perovskite-Sensitized Solid-State Solar Cells

Jeongmin Lim, Seong Young Kong, and Yong Ju Yun 

Department of Energy Engineering, Konkuk University, Seoul 05029, Republic of Korea

Correspondence should be addressed to Yong Ju Yun; [yjyun@konkuk.ac.kr](mailto:yjyun@konkuk.ac.kr)

Received 1 February 2018; Revised 15 May 2018; Accepted 29 May 2018; Published 25 June 2018

Academic Editor: Iftikhar Ali Sahito

Copyright © 2018 Jeongmin Lim et al. This is an open access article distributed under the Creative Commons Attribution License, which permits unrestricted use, distribution, and reproduction in any medium, provided the original work is properly cited.

Inorganic-organic mesoscopic solar cells become a promising alternative for conventional solar cells. We describe a  $\text{CH}_3\text{NH}_3\text{PbI}_3$  perovskite-sensitized solid-state solar cells with the use of different polymer hole transport materials such as 2,2',7,7'-tetrakis-(N,N-di-p-methoxyphenyl-amine)-9,9'-spirobifluorene (spiro-OMeTAD), poly(3-hexylthiophene-2,5-diyl) (P3HT), and poly[[4,8-bis[(2-ethylhexyl)oxy]benzo[1,2-b:4,5-b']dithiophene-2,6-diyl][3-fluoro-2-[(2-ethylhexyl)carbonyl]thieno[3,4-b]thiophenediyl]] (PTB7). The device with a spiro-OMeTAD-based hole transport layer showed the highest efficiency of 6.9%. Interestingly, the PTB7 polymer, which is considered an electron donor material, showed dominant hole transport behaviors in the perovskite solar cell. A 200 nm thin layer of PTB7 showed comparatively good efficiency (5.5%) value to the conventional spiro-OMeTAD-based device.

## 1. Introduction

The third-generation photovoltaic devices such as thin-film solar cells, organic solar cells, and solid-state solar cells are considered to be a promising energy conversion devices due to their ease of fabrication and cost-effective materials. Although highly efficient solar cells have already been commercialized based on silicon and other semiconductor materials, the fabrication cost of those photovoltaic devices is still expensive that prevents the technology from reaching widespread consumers. Generally, the purification of silicon-based materials involves high-temperature processing, and the device fabrication of such highly efficient solar cells relies on the vacuum deposition or/and thermal treatment methods which potentially increase the manufacturing cost and decrease the productivity. Third-generation solar cells such as dye-sensitized solar cells [1–5], quantum dot solar cells [6–9], and organic solar cells [10–13] are developed with various structures and diverse material applications. However, the theoretical maximum efficiency performances were far above with those of solar cells due to the energy losses or low dielectric [14]. Recently, a new class of light-absorbing material based on perovskite-structured organolead trihalide ( $\text{CH}_3\text{NH}_3\text{PbI}_3$ ) compound has been synthesized for the

development of high-efficiency solid-state solar cells [15]. A device using a thin layer of organolead trihalide perovskite as the light absorber and thin  $\text{TiO}_2$ - or  $\text{Al}_2\text{O}_3$ -based nanoporous scaffold layers could be fabricated using a simple solution process [15–17]. The active research on perovskite solar cell is blooming nowadays. For example, the role of mixed halide ( $\text{CH}_3\text{NH}_3\text{PbI}_{3-x}\text{Cl}_x$ ) perovskite with alumina scaffold layer enhances a faster electron transport [17]; Eperon et al. have reported on the PCE of 11.4% using the morphology-controlled perovskite photoactive layer [18]; Carnie et al. simplified a fabrication process of photoactive layer and achieved a power conversion efficiency (PCE) of 7.16% [19]; Heo et al. reported a PCE of 12% by replacing the spiro-OMeTAD hole transport materials with polytriarylamine (PTAA) polymer [20]; and other researchers represent a two-step deposition of perovskite materials for uniformly coated layer [21, 22]. One of the essential qualifications for the high efficiency of solar cells is a proper balance of series and shunt resistance. However, because of the high conductivity of perovskite materials, it demands a thick layer of HTM to evade the imbalance or pinhole effect [23, 24]. Due to these drawbacks, a thick layer of HTM was necessary, even though they have less conductivity with high series resistance. Herein, we investigated the roles of different

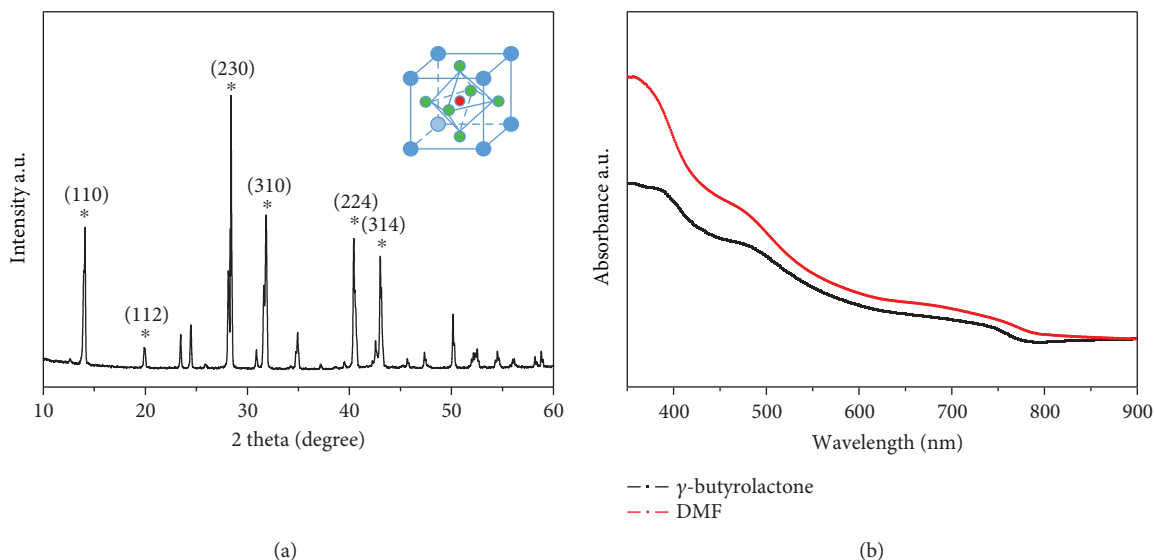


FIGURE 1: (a) X-ray diffraction of  $\text{CH}_3\text{NH}_3\text{PbI}_3$  perovskite materials prepared as powder form and inset shows tetragonal structure of materials. (b) UV-visible spectra prepared from  $\gamma$ -butyrolactone (GBL) and dimethylformamide (DMF). \* indicates the XRD peaks of  $\text{CH}_3\text{NH}_3\text{PbI}_3$  perovskite materials.

HTMs on the performance of solid-state perovskite solar cells. The fluorine-doped tin oxide (FTO) glass was used as the substrate; a synthesized  $\text{CH}_3\text{NH}_3\text{PbI}_3$  perovskite as a light absorber (electron donor); the polymers such as 2,2',7,7'-tetrakis-(N,N-di-p-methoxyphenyl-amine)-9,9'-spirobifluorene (spiro-OMeTAD), poly(3-hexylthiophene-2,5-diyl) (P3HT), and poly[[4,8-bis[(2-ethylhexyl)oxy]benzo[1,2-b:4,5-b']dithiophene-2,6-diyl][3-fluoro-2-[(2-ethylhexyl)carbonyl]thieno[3,4-b]thiophenediyl]] (PTB7) as hole transport materials; and a sputtered gold grid as the counter electrode.

## 2. Materials and Methods

**2.1. Perovskite Materials.** The methylammonium perovskite material ( $\text{CH}_3\text{NH}_3\text{PbI}_3$ ) was synthesized according to the previously reported method [15]. A hydroiodic acid (30 mL, 57 wt.% in water, Aldrich) was mixed with methylamine (27.8 mL, 0.273 mol, 40% in methanol; TCI) at  $0^\circ\text{C}$  in ice bath with continuous stirring for 2 h. After stirring, the resulting solution was evaporated in a vacuum oven, and the methyl ammonium iodide ( $\text{CH}_3\text{NH}_3\text{I}$ ) compound was formed. The synthesized product was washed with diethyl ether for three times and then dried under vacuum without further purification; a formation of white coloured powder is an indication of purified methyl ammonium iodide precursor. To prepare the final product of  $(\text{CH}_3\text{NH}_3)\text{PbI}_3$ , the 1:1 molar ratio of methylammonium iodide and lead (II) iodide was dissolved in anhydrous  $\gamma$ -butyrolactone (GBL) and then continuously stirred at  $60^\circ\text{C}$  temperature overnight.

**2.2. Solar Cell Fabrication.** Fluorine-doped tin oxide (FTO) glasses (Pilkington, TEC-8,  $8\ \Omega/\text{sq}$ ) were washed with a detergent solution and then cleaned in an ultrasonic bath for 5 min using an ethanol-acetone solution ( $v/v = 1/1$ ) and 2-propanol, in turn, and then further cleaned with the

oxygen plasma treatment for the duration of 15 min. A  $600\ \text{\AA}$  thin layer of dense  $\text{TiO}_2$  blocking layer was deposited on the FTO glass using the RF sputtering method. A commercial  $\text{TiO}_2$  paste (CCIC 18NT) diluted with terpineol was used as a precursor, and the mesoporous  $\text{TiO}_2$  layer was deposited on the blocking layer using the spin-coating (4500 rpm, 40 sec) technique. The coated layer was annealed in air atmosphere at  $500^\circ\text{C}$  for 1 h and then cooled to room temperature. The perovskite liquid is subsequently coating on the  $\text{TiO}_2$  layer using spin coater at 2500 rpm for 40 seconds followed by annealing at  $100^\circ\text{C}$  for 20 min. For the deposition of the hole transport layer, different hole transport materials (HTM) are coated onto a perovskite film using the spin coater with a speed of 2500 rpm for 40 sec. To fabricate the counter electrode, 70 nm Au electrode was deposited onto the hole transport layer using the thermal evaporation method.

**2.3. Composition of HTM.** The spiro-OMeTAD-based HTM was prepared by mixing 170 mM concentration of 2,2',7,7'-tetrakis-(N,N-di-p-methoxyphenyl-amine)-9,9'-spirobifluorene (spiro-OMeTAD, Merk), 198 mM concentration of 4-tert-butylpyridine (TBP, 96%, Aldrich), and 64 mM concentration of bis(trifluoromethane) sulfonimide lithium salt (LiTFSI, 99.95%, Aldrich) together using a cocktail solvent of chlorobenzene and acetonitrile ( $1/0.1 = v/v$ ). The P3HT-based HTM solution was prepared by dissolving P3HT (Aldrich) in a chlorobenzene solvent with the concentration of 13 mg/mL. Likewise, PTB7 was also dissolved in chlorobenzene with the concentration of 12 mg/mL.

**2.4. Characterization.** The active area of the cell was measured by an optical microscope (Olympus), and the thickness of the mesoporous  $\text{TiO}_2$  layer was analysed by a surface profilometer (P-6, KLA-Tencor). The photovoltaic properties of the cells were measured using a Keithley

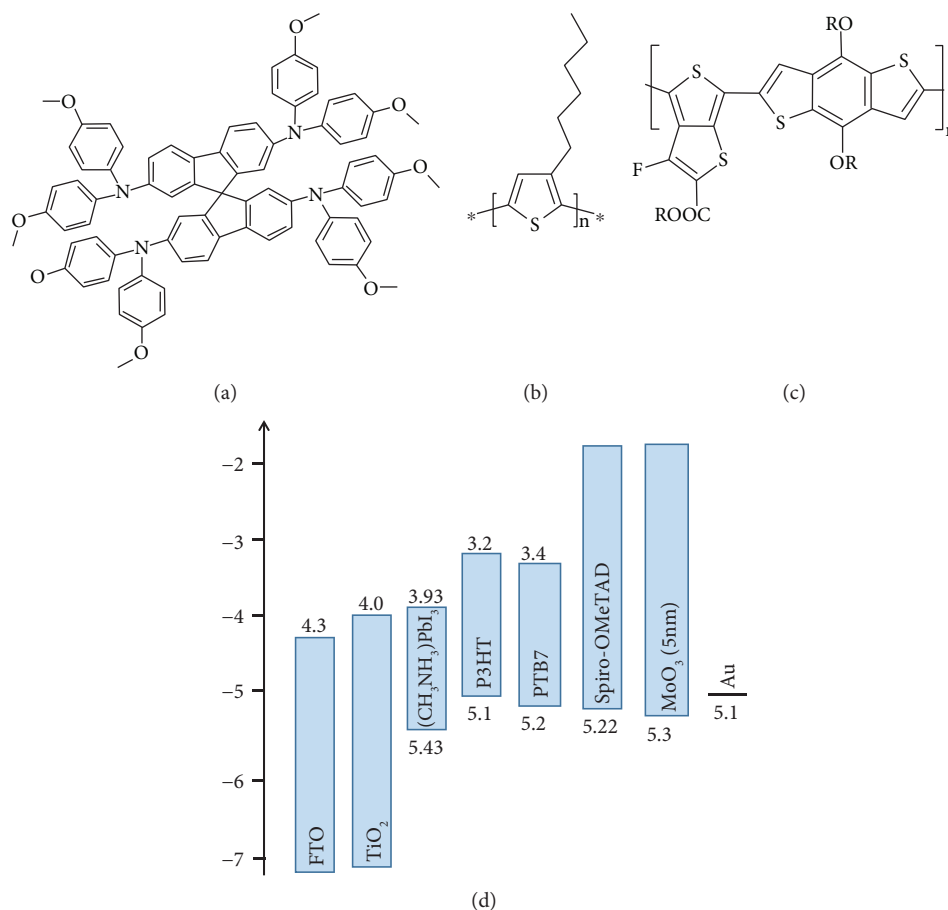


FIGURE 2: Molecular structure of hole conductor materials of (a) spiro-OMeTAD, (b) P3HT, and (c) PTB7. (d) Energy diagram of materials which was used in this study.

TABLE 1: The levels of HOMO, LUMO, and hole mobility of THM materials.

	HOMO	LUMO	Hole mobility
Spiro-OMeTAD			$\sim 10^{-5}$ cm <sup>2</sup> /V·sec
P3HT	-5.1	-3.2	$\sim 10^{-1}$ cm <sup>2</sup> /V·sec
PTB7	-5.15	-3.31	$\sim 10^{-3}$ cm <sup>2</sup> /V·sec

2400 digital source meter under the irradiation of a solar simulator (AM 1.5 G, 100 mW/cm<sup>2</sup>, Sol3A, class AAA, Oriel) as a light source. Irradiation of 1 sun was calibrated by using a certified standard reference cell (PV Measurement Inc.). The photovoltaic performance has been characterized by the measurement of  $V_{oc}$ ,  $J_{sc}$ , fill factor, and overall efficiency values obtained from the J-V curve. The incident photon to current conversion efficiency (IPCE) spectra was measured using a PV measurement (PV Measurement Inc., QEX7 series), and cross-sectional morphology of the solid state solar cell was analysed by a field-emission scanning electron microscopy (FE-SEM, Nano230, FEI Co.).

### 3. Result and Discussion

Here, we fabricated a new bilayer heterojunction with organic-inorganic materials onto the nanoporous or

mesoporous TiO<sub>2</sub> film. The surface-decorated metal-halide perovskite materials with the formula of (C<sub>n</sub>H<sub>2n+1</sub>NH<sub>3</sub>) MX (M = Pb; X = I, Br, Cl) were infiltrated within a TiO<sub>2</sub> matrix, which has a key function of light absorption process. The various organic materials have p-type hole transport properties and are thus referred to as HTMs.

Figure 1(a) shows the powder X-ray diffraction (XRD) peaks of the crystalline perovskite materials. There are six sharp reflection peaks such as (110), (112), (220), (310), (224), and (314) that were observed which confirm the tetragonal perovskite structure (include here any JCPDS number available). The inset of Figure 1(a) shows a tetragonal crystal structure of (C<sub>n</sub>H<sub>2n+1</sub>NH<sub>3</sub>) MX perovskite material. The perovskite material was dissolved into  $\gamma$ -butyrolactone (GBL) or dimethylformamide (DMF) and then coated on the glass plate using spin-coating method. The UV-vis spectrum of the thin perovskite material is measured for the range of 350–900 nm wavelength. From the UV-vis spectra, the synthesized perovskite material absorbs wide range of solar spectrum from the visible to near-infrared region as shown in Figure 1(b). To maximize the energy harvested by the solar cells, light-absorbing materials with wide spectral response ranges could expand the absorbance throughout the visible spectrum. From the observed

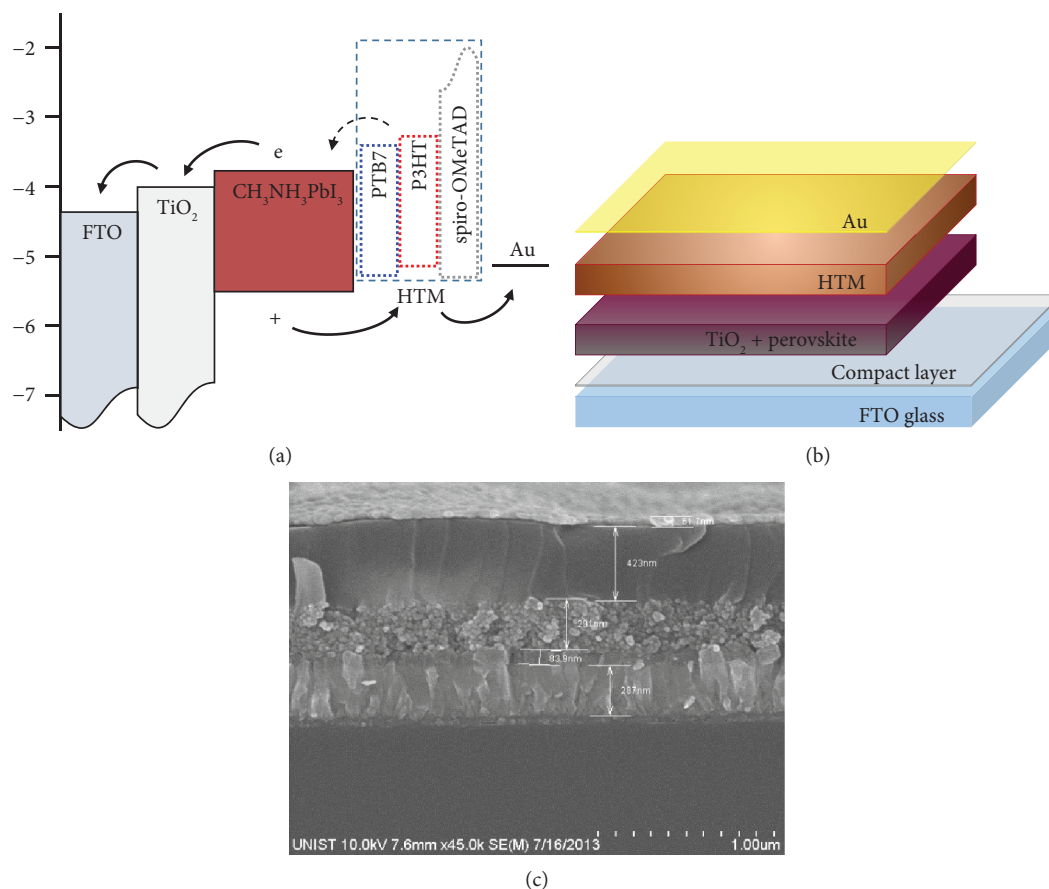


FIGURE 3: (a) Schematic of energy alignment of the different components. (b) Structure of the device architecture. (c) SEM image of the architecture.

UV spectra, the abovementioned criteria could be satisfied by the synthesized CH<sub>3</sub>NH<sub>3</sub>PbI<sub>3</sub> perovskite material.

Because of the high conductivity of perovskite materials, the thick layer of HTM should be coated onto the perovskite material in order to prevent the pinhole effect. However, a thick layer of HTM cause a high series resistance and decrease the efficiency of the device. Figure 2(a) shows the molecular orbital match of three different types of tested hole transport materials (spiro-OMeTAD, P3HT, and PTB7) with the other components of the device. Table 1 shows the HOMO and LUMO energy level as well as hole mobility value of three different HTM materials. The energy diagrams of each component are shown in Figure 2(b) with the HTM materials. From the previous report, spiro-OMeTAD was widely used as a hole conductor in CH<sub>3</sub>NH<sub>3</sub>PbI<sub>3</sub>-based perovskite solar cells, and P3HT and PTB7 were generally used as an electron donor and/or hole transport material in organic solar cells. Notably, even though the P3HT and PTB are usually used as electron donor in organic electronic devices, here we used those materials as hole transport materials.

Figure 3(a) illustrates the energy levels of the system components and model of the charge separation processes; Figure 3(b) shows the schematic configuration of the device with the stacking of different components. In Figure 3(a),

the tested HTM materials are energetically matched with perovskite sensitizer, and the energy level of the perovskite sensitizer is well positioned for the injection of electron into TiO<sub>2</sub> matrix and the injection of holes into the HTM Layer. A cross-sectional SEM image of the fabricated device is shown in Figure 3(c). In order to protect the electron recombination, a thin TiO<sub>2</sub> layer, called the “compact layer,” was deposited onto the transparent conducting oxide (TCO). Mesoporous TiO<sub>2</sub> with metal-halide-based perovskite sensitizer as an active layer, HTM, and Au electrode was deposited in sequence. From the cross-sectional analysis, the thickness of spiro-OMeTAD, P3HT, and PTB7 layer was observed as 420 nm. The role of each HTM on the performance of the device is characterized separately. For that, solar cells containing different HTMs are used separately with the CH<sub>3</sub>NH<sub>3</sub>PbI<sub>3</sub>-coated TiO<sub>2</sub> layer, and the individual device performance is measured under 1-sun illumination.

The photovoltaic parameters of all the three devices are extracted from the *J-V* curves (Figure 4) and are listed in Table 2. For comparison, without HTM (black, circle) sample was prepared. A metal-halide perovskite-sensitized cell without HTM shows a  $J_{sc}$  of 4.5 mAcm<sup>-2</sup>,  $V_{oc}$  of 0.38 V, and FF of 44.7 with efficient ( $\eta$ ) of 0.8%. The device made of spiro-OMeTAD- (red, circle) based HTM layer shows the best efficiency of 6.9% with a  $J_{sc}$  of 13.9 mAcm<sup>-2</sup>,  $V_{oc}$  of 0.82 V, and

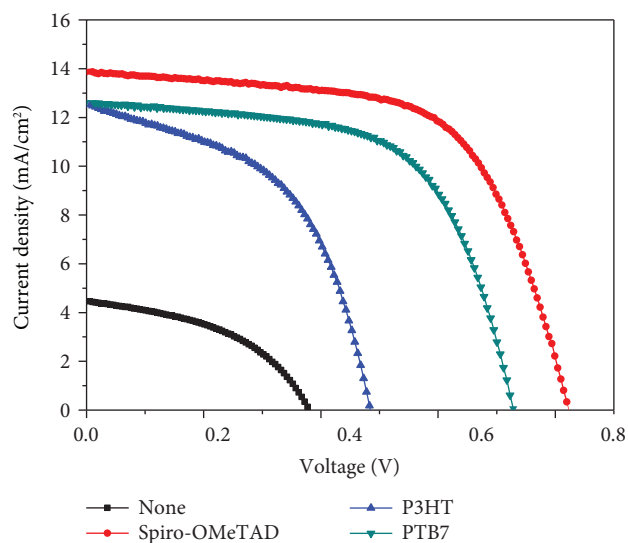


FIGURE 4: Photocurrent-voltage curves without HTM sample (black, circle), spiro-OMeTAD sample (red, circle), P3HT sample (blue, triangle), and PTB7 sample (cyan, triangle).

TABLE 2: Photovoltaic performance of the cells with various HTMs.

	$J_{sc}$ (mA/cm <sup>2</sup> )	$V_{oc}$ (V)	FF (%)	Eff (%)
—	4.5	0.38	44.7	0.8
OMeTAD	13.9	0.82	60.2	6.9
P3HT	12.5	0.51	50.6	3.2
PTB7	12.6	0.72	60.4	5.5

FF of 60.2. Although P3HT is usually used as a hole conductor in organic solar cells, the device made with P3HT does not show a high efficiency in perovskite-based solar cells. In general, PTB7 is used as an electron donor for organic solar cells, but in perovskite solar cells, it plays a role of hole conductor at this study. The device made of PTB7 hole transport layer exhibits a  $J_{sc}$  of 12.6 mAcm<sup>-2</sup>,  $V_{oc}$  of 0.72 V, FF of 60.4, and  $\eta$  of 5.5% by demonstrating a good charge-separation kinetics, and the efficiency value is comparable to the conventional spiro-OMeTAD-based device. Moreover, the thickness of the PTB7 hole transport layer is thinner (around 200 nm) than that of the spiro-OMeTAD layer (423 nm). In general, a thicker layer causes the higher series resistance of the device; however, the spiro-OMeTAD with a thinner layer of around 200 nm causes higher pinhole effects that may lead to the poor cell performance. In this work, we have demonstrated that PTB7 with a relatively thin hole transport layer showed the comparable efficiency value with the spiro-OMeTAD-based conventional cells. Obviously, P3HT and PTB7 show light absorption in UV range and also play a role of electron donor in organic solar cells; their role of hole transport behaviour in perovskite solar cell was confirmed using IPCE spectra.

Figure 5 shows the IPCE spectra of a device made of spiro-OMeTAD-based hole transport layer (black square) and PTB7 layer (red circle). The IPCE spectra of the cells

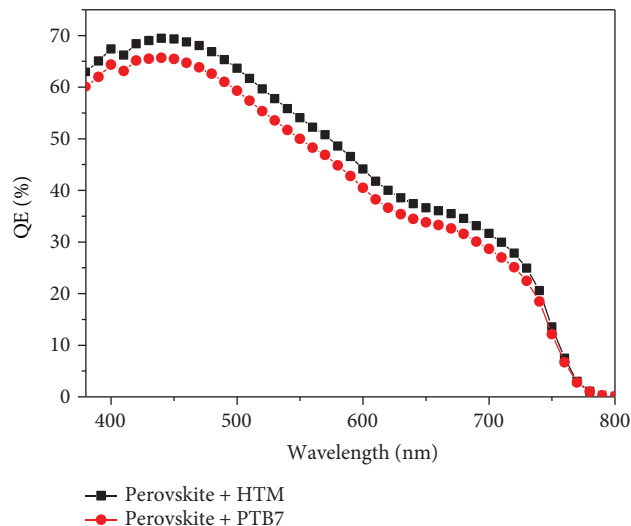


FIGURE 5: Incident photon to current conversion efficiency (IPCE) of the perovskite solar cells. Perovskite with spiro-OMeTAD (black, square) and perovskite with PTB7 (red, circle).

indicate that the devices show spectral responses from the near-infrared to visible regions, with the maximum photoreponse at ~450 nm and broader peaks extending to the infrared region. This IPCE spectra matched well with the UV-vis absorbance of the synthesized perovskite film as shown in Figure 1(b). However, polymer-based HTM cells do not show any other peculiar photoresponse for polymers, which confirms that here, the P3HT and PTB7 polymers play a role of only a hole conductor not as an electron donor.

## 4. Conclusions

In conclusion, we have demonstrated the solid-state solar cells with the CH<sub>3</sub>NH<sub>3</sub>PbI<sub>3</sub> organic perovskite material as the light absorber and three different organic hole transport materials. Among the three HTMs (spiro-OMeTAD, P3HT, and PTB7), spiro-OMeTAD cells show the best efficiency with 6.9% under AM 1.5 G. However, PTB7, which is a common electron donor material in organic solar cells, shows the hole transport behaviour in perovskite-based solid-state solar cells, and also a relatively thinner layer of PTB7 shows a good efficiency of 5.5%. Moreover, the energy level matching of these organic HTMs is well matched with the other components of the device. This interesting observation opens up the door for the investigation of different cost-effective materials for the highly efficient organic-inorganic hybrid solar cells in the near future.

## Data Availability

The data used to support the findings of this study are available from the corresponding author upon request.

## Conflicts of Interest

The authors declare that there are no conflicts of interest regarding the publication of this paper.

## Acknowledgments

This research was supported by the KU Research Professor Program of Konkuk University.

## References

- [1] B. O'Regan and M. Grätzel, "A low-cost, high-efficiency solar cell based on dye-sensitized colloidal TiO<sub>2</sub> films," *Nature*, vol. 353, no. 6346, pp. 737–740, 1991.
- [2] M. Grätzel, U. Bach, D. Lupo et al., "Solid-state dye-sensitized mesoporous TiO<sub>2</sub> solar cells with high photon-to-electron conversion efficiencies," *Nature*, vol. 395, no. 6702, pp. 583–585, 1998.
- [3] M. Law, L. E. Greene, J. C. Johnson, R. Saykally, and P. Yang, "Nanowire dye-sensitized solar cells," *Nature Materials*, vol. 4, no. 6, pp. 455–459, 2005.
- [4] J. Lim, M. Lee, S. K. Balasingam, J. Kim, D. Kim, and Y. Jun, "Fabrication of panchromatic dye-sensitized solar cells using pre-dye coated TiO<sub>2</sub> nanoparticles by a simple dip coating technique," *RSC Advances*, vol. 3, no. 14, p. 4801, 2013.
- [5] Y. Jo, J. Y. Cheon, J. Yu et al., "Highly interconnected ordered mesoporous carbon-carbon nanotube nanocomposites: Pt-free, highly efficient, and durable counter electrodes for dye-sensitized solar cells," *Chemical Communications*, vol. 48, no. 65, pp. 8057–8059, 2012.
- [6] S. A. McDonald, G. Konstantatos, S. Zhang et al., "Solution-processed PbS quantum dot infrared photodetectors and photovoltaics," *Nature Materials*, vol. 4, no. 2, pp. 138–142, 2005.
- [7] D. J. Milliron, S. M. Hughes, Y. Cui et al., "Colloidal nanocrystal heterostructures with linear and branched topology," *Nature*, vol. 430, no. 6996, pp. 190–195, 2004.
- [8] A. J. Nozik, "Quantum dot solar cells," *Physica E: Low-dimensional Systems and Nanostructures*, vol. 14, no. 1-2, pp. 115–120, 2002.
- [9] I. Robel, V. Subramanian, M. Kuno, and P. V. Kamat, "Quantum dot solar cells. Harvesting light energy with CdSe nanocrystals molecularly linked to mesoscopic TiO<sub>2</sub> films," *Journal of the American Chemical Society*, vol. 128, no. 7, pp. 2385–2393, 2006.
- [10] S. Günes, H. Neugebauer, and N. S. Sariciftci, "Conjugated polymer-based organic solar cells," *Chemical Reviews*, vol. 107, no. 4, pp. 1324–1338, 2007.
- [11] W. U. Huynh, J. J. Dittmer, and A. P. Alivisatos, "Hybrid nanorod-polymer solar cells," *Science*, vol. 295, no. 5564, pp. 2425–2427, 2002.
- [12] M. C. Scharber, D. Mühlbacher, M. Koppe et al., "Design rules for donors in bulk-heterojunction solar cells—towards 10 % energy-conversion efficiency," *Advanced Materials*, vol. 18, no. 6, pp. 789–794, 2006.
- [13] B. C. Thompson and J. M. J. Fréchet, "Polymer-fullerene composite solar cells," *Angewandte Chemie-International Edition*, vol. 47, no. 1, pp. 58–77, 2008.
- [14] H. J. Snaith, "Estimating the maximum attainable efficiency in dye-sensitized solar cells," *Advanced Functional Materials*, vol. 20, no. 1, pp. 13–19, 2010.
- [15] A. Kojima, K. Teshima, Y. Shirai, and T. Miyasaka, "Organometal halide perovskites as visible-light sensitizers for photovoltaic cells," *Journal of the American Chemical Society*, vol. 131, no. 17, pp. 6050–6051, 2009.
- [16] H. S. Kim, C. R. Lee, J. H. Im et al., "Lead iodide perovskite sensitized all-solid-state submicron thin film mesoscopic solar cell with efficiency exceeding 9%," *Scientific Reports*, vol. 2, no. 1, p. 591, 2012.
- [17] M. M. Lee, J. Teuscher, T. Miyasaka, T. N. Murakami, and H. J. Snaith, "Efficient hybrid solar cells based on meso-structured organometal halide perovskites," *Science*, vol. 338, no. 6107, pp. 643–647, 2012.
- [18] G. E. Eperon, V. M. Burlakov, P. Docampo, A. Goriely, and H. J. Snaith, "Morphological control for high performance, solution-processed planar heterojunction perovskite solar cells," *Advanced Functional Materials*, vol. 24, no. 1, pp. 151–157, 2014.
- [19] M. J. Carnie, C. Charbonneau, M. L. Davies et al., "A one-step low temperature processing route for organolead halide perovskite solar cells," *Chemical Communications*, vol. 49, no. 72, pp. 7893–7895, 2013.
- [20] J. H. Heo, S. H. Im, J. H. Noh et al., "Efficient inorganic-organic hybrid heterojunction solar cells containing perovskite compound and polymeric hole conductors," *Nature Photonics*, vol. 7, no. 6, pp. 486–491, 2013.
- [21] J. Burschka, N. Pellet, S. J. Moon et al., "Sequential deposition as a route to high-performance perovskite-sensitized solar cells," *Nature*, vol. 499, no. 7458, pp. 316–319, 2013.
- [22] D. Bi, S.-J. Moon, L. Haggman et al., "Using a two-step deposition technique to prepare perovskite (CH<sub>3</sub>NH<sub>3</sub>PbI<sub>3</sub>) for thin film solar cells based on ZrO<sub>2</sub> and TiO<sub>2</sub> mesostructures," *RSC Advances*, vol. 3, no. 41, article 18762, 2013.
- [23] D. Bi, L. Yang, G. Boschloo, A. Hagfeldt, and E. M. J. Johansson, "Effect of different hole transport materials on recombination in CH<sub>3</sub>NH<sub>3</sub>PbI<sub>3</sub> perovskite-sensitized mesoscopic solar cells," *The Journal of Physical Chemistry Letters*, vol. 4, no. 9, pp. 1532–1536, 2013.
- [24] E. Edri, S. Kirmayer, D. Cahen, and G. Hodes, "High open-circuit voltage solar cells based on organic-inorganic lead bromide perovskite," *The Journal of Physical Chemistry Letters*, vol. 4, no. 6, pp. 897–902, 2013.

## Research Article

# Self-Ordered Voids Formation in SiO<sub>2</sub> Matrix by Ge Outdiffusion

**B. Pivac** <sup>1</sup>, **P. Dubček**<sup>1</sup>, **J. Dasović**<sup>1</sup>, **H. Zorc**<sup>1</sup>, **S. Bernstorff** <sup>2</sup>,  
**J. Zavašnik**<sup>3</sup> and **B. Vlahovic**<sup>4</sup>

<sup>1</sup>Ruder Bošković Institute, Bijenička 54, 10000 Zagreb, Croatia

<sup>2</sup>Eletra-Sincrotrone Trieste, SS 14, Km 163.5, 34149 Basovizza, Italy

<sup>3</sup>Center for Electron Microscopy and Microanalysis, Jožef Stefan Institute, Jamova Cesta 39, SI-1000 Ljubljana, Slovenia

<sup>4</sup>North Carolina Central University, Durham, NC, USA

Correspondence should be addressed to B. Pivac; pivac@irb.hr

Received 7 December 2017; Accepted 12 March 2018; Published 26 April 2018

Academic Editor: Iftikhar Ali Sahito

Copyright © 2018 B. Pivac et al. This is an open access article distributed under the Creative Commons Attribution License, which permits unrestricted use, distribution, and reproduction in any medium, provided the original work is properly cited.

The annealing behavior of very thin SiO<sub>2</sub>/Ge multilayers deposited on Si substrate by e-gun deposition in high vacuum was explored. It is shown that, after annealing at moderate temperatures (800°C) in inert atmosphere, Ge is completely outdiffused from the SiO<sub>2</sub> matrix leaving small (about 3 nm) spherical voids embedded in the SiO<sub>2</sub> matrix. These voids are very well correlated and formed at distances governed by the preexisting multilayer structure (in vertical direction) and self-organization (in horizontal direction). The formed films produce intensive photoluminescence (PL) with a peak at 500 nm. The explored dynamics of the PL decay show the existence of a very rapid process similar to the one found at Ge/SiO<sub>2</sub> defected interface layers.

## 1. Introduction

An enhancement of the absorption in the visible range is crucial for increasing the conversion efficiency of solar cells. Recently, several attempts have been made to use photonic crystals for enhancing light absorption in thin layers [1–3]. But the specific design of possible new photovoltaic devices is still an open discussion, and definite guidelines for reliable light absorption enhancement have not been proposed.

Silicon dioxide, which is transparent at visible wavelengths, is fully compatible with Si technology, and due to its low cost it is interesting as a potential photonic material. Indeed a successful application of silica in photonics has been demonstrated [4, 5]. Furthermore, it has been recently shown that the use of silica based photonic crystals significantly contributes to radiative cooling of solar absorbers and hence increases their efficiency of solar energy conversion [6]. Among other applications, the fabrication of void arrays in the bulk of dielectrics has drawn great attention for its potential applications in three-dimensional (3D) optical storage, photonic crystal, and integrated optics [7]. Since the

early observation of femtosecond-laser induced periodically aligned nanovoids inside conventional borosilicate glass by Kanehira et al. in 2005 [8], many groups have been devoted to exploring the applications and formation mechanisms of self-organized void arrays.

Many other different ways to produce porous SiO<sub>2</sub> layers have been explored. Recently it has been shown that Ge implantation in fused silica followed by annealing creates spherical voids in the matrix with dimensions of few to few tenths of nanometers [9, 10]. In the following a new and rather simple procedure for transparent silica photonic layer production will be proposed, based on Ge outdiffusion and void formation and self-organization in silica matrix.

## 2. Experimental

**2.1. Sample Preparation.** A multilayer film consisting of alternating SiO<sub>2</sub> and Ge layers, each 2 nm thick, was prepared by e-gun deposition of 20 bilayers, in vacuum better than 10<sup>-6</sup> Torr. The solid sources for the SiO<sub>2</sub> and Ge layer deposition were grains (4N and 6N purity, resp., from

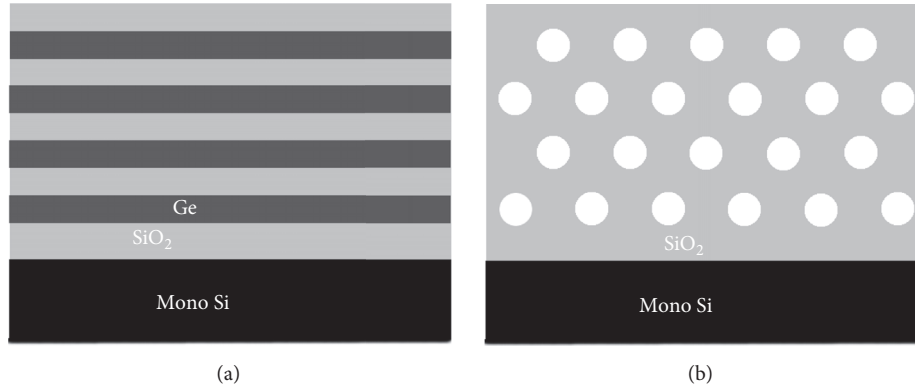


FIGURE 1: Schematic representation of an as-deposited 2 nm SiO<sub>2</sub>/2 nm Ge multilayer with a 20 nm SiO<sub>2</sub> capping layer at the top (a) and after annealing at 800°C, showing cavities (white) in SiO<sub>2</sub> matrix (b).

Alfa Res.). Cleaned and freshly etched p-type (100)-oriented Si monocrystals were used as substrates, held at 200°C during the deposition. The Si substrates were rotated on a planetary holder during the deposition to ensure lateral homogeneity of the films over the whole substrate surface. After deposition, the samples were annealed at 800°C for 1 h in flowing N<sub>2</sub> atmosphere. During this annealing Ge initially clusters into nanoparticles [11] and afterwards outdiffuses from the film (below the measurable level of Raman and XRD spectroscopy). Finally layers of cavities were obtained separated by the approx. 2 nm of SiO<sub>2</sub> spacer layer is shown schematically in Figure 1.

**2.2. Characterization Procedure.** Grazing incidence small-angle X-ray scattering (GISAXS) experiments were performed at Elettra-Sincrotrone, Trieste, Italy, on the SAXS beamline [12], using synchrotron radiation with photon energy of 8 keV. Several grazing angles of incidence  $\alpha_i$  were selected in the range  $0.23^\circ < \alpha_i < 0.23^\circ + 0.1^\circ$ , for which the effective area of the beam footprint was smaller than the sample surface area (approx.  $10 \times 10$  mm). The selected angles above the critical angle  $\alpha_c$  allowed the X-rays to penetrate through the capping layer and deep enough into the film. The angular range of the detector was calibrated by measuring the SAXS standard silver behenate. A narrow, partly transparent Al strip was placed in front of the detector for local intensity reduction in order to avoid saturation in the specular plane direction where the usually much stronger surface scattering is present.

Two-dimensional patterns of the scattering intensity were recorded with a 2D image plate detector with  $2000 \times 2000$  pixels, having a dynamical range of  $10^6$  and a pixel size of  $0.2 \times 0.2$  mm, at the distance  $L = 1800$  mm from the sample. The optical path from the sample to the detector was kept in vacuum in order to reduce the background due to air scattering.

Raman spectra were acquired on a Labram HR Evolution system equipped with a microscope and a 473 nm laser excitation source.

The optical reflectivity in the UV-Vis range was measured with a Perkin Elmer Lambda 45 spectrometer with a gold mirror as reference.

Photoluminescence (PL) was measured at room temperature using a continuous wave laser diode at 405 nm, and the PL spectra were collected using a BWTek BCR 112E spectrometer coupled with a Sony ILX511 CCD linear image sensor.

The crystallinity and phase composition of the nanoparticles were analysed with an aberration-corrected transmission electron microscope (TEM), operating at 300 keV and capable of chemical analyses by employing energy dispersive X-ray spectroscopy (EDS). Samples for the TEM study were prepared as cross-sections of thin films. These were glued face-to-face with an epoxy resin, formatted into 3 mm disks and mechanically thinned to approximately 100  $\mu\text{m}$ . The central part of the disks was additionally dimpled on a rotation wheel down to 10  $\mu\text{m}$  and ion-milled with Ar<sup>+</sup> ions at 4 keV until perforation.

### 3. Results and Discussion

The results of the Raman spectroscopy, shown in Figure 2, confirm the existence of Ge layers alternated with SiO<sub>2</sub> layers in the as-deposited sample. This sample, represented by the black curve, shows the presence of amorphous Ge layers with characteristic broad peaks close to 90, 190, 240, and 279  $\text{cm}^{-1}$  corresponding to the Ge TA, LA, and LO modes, respectively [13]. The peak at 520  $\text{cm}^{-1}$  is due to the Si TO mode derived from the substrate. After annealing at 800°C or higher Ge was not anymore observed in the sample (within the sensitivity of the employed Raman instrument). The only peak observed for the annealed sample, at 521  $\text{cm}^{-1}$ , is due to the TO band from the silicon substrate. The same behavior was verified with X-ray diffraction (not shown here).

Since Ge was not anymore observable (by Raman and XRD spectroscopy) upon annealing at high temperatures, in order to explore the remaining structures in the sample, several techniques were considered. Scanning electron microscopy has the intrinsic difficulty of surface charging

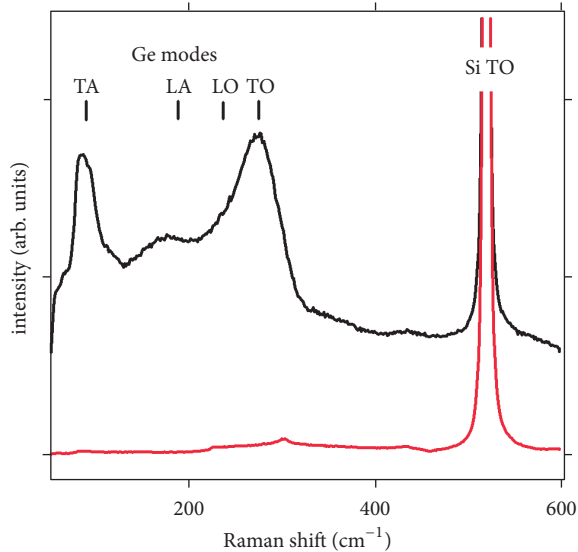


FIGURE 2: Raman spectra of an as-deposited (black), and an annealed at 800°C (red) multilayer sample.

in dielectrics which is usually removed by covering the sample surface with an Au layer. Since we expected to explore structures (voids) with sizes of less than 5 nm a metal cover could mask the structures of interest, which indeed happened in several of our attempts. Therefore as a measuring technique of choice for such a task grazing incidence small-angle X-ray scattering (GISAXS) was selected.

It is long known that with X-ray scattering complementary information (to microscopy results) can be obtained in reciprocal space. However, for a long time, the weak interaction of hard X-rays with matter hampered its straightforward use for surface and/or interface studies. Nevertheless, pioneering works in the 80s [14], combining the use of high brilliance synchrotron radiation with grazing incidence geometry, enabled reaching sufficient surface sensitivity with a reasonable signal to noise ratio. In comparison to conventional microscopy, GISAXS [15] has several advantages:

- (i) It is a nondestructive technique, provided that the samples withstand hard X-ray exposure.
- (ii) each measurement is averaging over the whole measured sample surface, providing therefore statistical information over several square centimeters as compared to nanoregions in microscopy;
- (iii) Depth profiling of the samples can be easily performed by varying the grazing incident angle of the X-rays beam, which allows probing selectively the surface, buried interfaces, and the bulk of a sample;
- (iv) The GISAXS technique provides morphological information from the nanometer to micrometer length scales. Furthermore, it can be combined, simultaneously and on the same samples, with the grazing incidence wide angle X-ray scattering or diffraction (GIWAXS) technique which is sensitive to the atomic arrangement and strain state.

2D GISAXS patterns obtained from the sample annealed at 800°C are presented in Figure 3. Here (in Figure 3(a)) the X-ray scattering originating from nanoparticles or voids embedded in the bulk is mixed with the one caused by the surface morphology and the roughness of the interface between layers, which are dominantly contributing to the signal close to the specular plain. Therefore the scattering, there, is generally most intense (this is the reason why a narrow Al foil was placed in the beam path, to partly attenuate the strong intensity signal in the specular plain).

The specific shape with two shoulders close to the Yoneda plain ( $q_z$  close to  $0.2 \text{ nm}^{-1}$ ) visible in Figure 3(b) suggests X-ray scattering from correlated objects in the sample. Nevertheless, a scattering contribution from the very surface cannot be excluded. To remove the contribution from the roughness originating dominantly from the surface, the intensity taken at the critical angle in Figure 3(a) was subtracted numerically from the intensity obtained at a larger angle of grazing incidence (i.e.,  $0.038^\circ$  above the critical angle) shown in Figure 3(b), displaying therefore only the contribution derived from the deeper regions of the film (Figure 3(c)) [16]. The differential result obtained in this way confirms that the observed nanoparticles exist deeper inside the films.

In the first approximation, it was assumed that the spherical voids are grown evenly distributed throughout the film. For such a case a scattering model was developed, where the particles radius  $R$  is allowed to vary according to a normal size distribution. The spatial distribution of the particles is described by the local monodisperse approximation (LMA). Applying numerical fitting to the measured experimental data of Figure 3(b), a wide size distribution for the voids diameter ( $D$ ) was found, centered at  $D_h = 2.95 \pm 0.35 \text{ nm}$  in horizontal direction and  $D_v = 2.33 \pm 0.31 \text{ nm}$  in vertical direction. Thus the fitting revealed that the voids are spherical with only a very small eccentricity.

In Figure 4 the fitting results for the scattering pattern of Figure 3(b) are summarized and presented as voids size distribution in vertical and horizontal directions. When the fitting was applied to the scattering data after subtracting the surface scattering (Figure 3(c)), the distributions of the size values get wider and slightly shifted in direction of bigger particles as compared to the fitting results obtained for Figure 3(b). This is explained by the influence of surface features which are generally smaller than the voids formed inside the film.

Due to the precise deposition of well-defined multilayered  $\text{SiO}_2/\text{Ge}$  layers, after annealing well-defined layers of cavities were obtained at the positions where the Ge layers used to be prior to annealing. This causes the appearance of a Bragg sheet [17] in Figures 3(a) and 3(b) at about  $q_z = 1.3 \text{ nm}^{-1}$  parallel to the  $q_y$  axis due to the periodicity contrast of the void layers. The period  $d$  of the void layers is calculated from the Bragg sheet position by the expression  $d = 2\pi/q_z$ , where  $q_z$  is the distance to the maximum of the first Bragg sheet. The measured period is  $d = 4.8 \text{ nm}$ , very close to the original bilayer thickness.

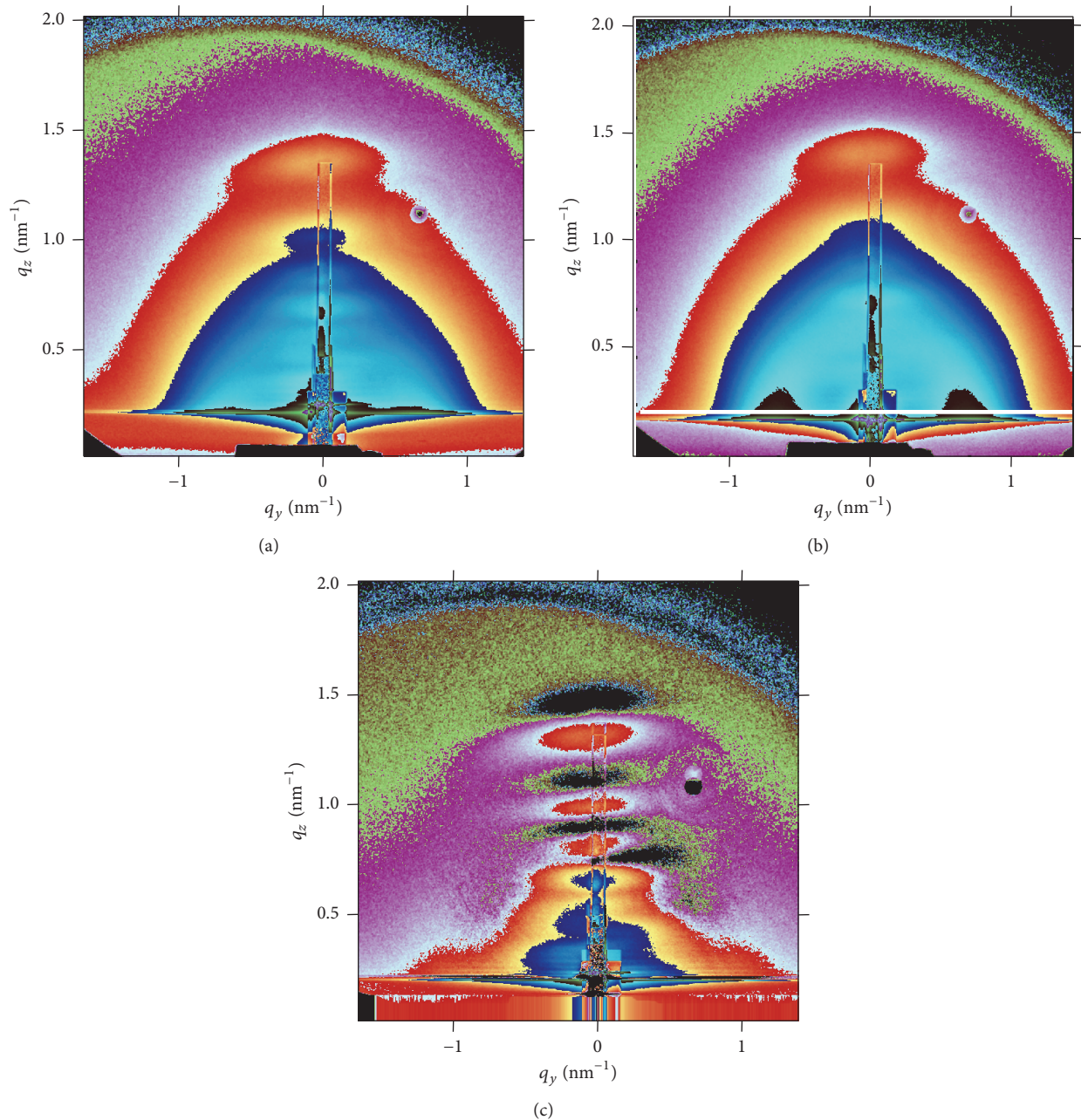


FIGURE 3: 2D GISAXS intensity pattern from the sample annealed at  $800^\circ\text{C}$  obtained (a) at the critical angle of grazing incidence  $\alpha_c$ . The white line represents the Yoneda plain position where the linear intensity plot for the correlation analysis was taken. (b) 2D GISAXS pattern from the sample obtained at  $\alpha_c + 0.038^\circ$ . (c) Numerical difference between the intensities from (b) and (a) (see the text for details).

A horizontal cut taken from the 2D scattering pattern shown in Figure 3(b) at the position of the horizontal white line is presented in Figure 5. The figure shows two very pronounced correlation peaks placed at about  $q_y = \pm 1.3 \text{ nm}^{-1}$ , indicating a rather strong correlation of the average voids interspacing in horizontal direction. Therefore, it was shown that in addition to the vertical ordering defined by the multilayer deposition, horizontal self-ordering has been obtained also. Furthermore, from the fitting procedure the void-to-void distance in horizontal direction is obtained

as  $7.03 \pm 1.85 \text{ nm}$  and in vertical direction as  $4.29 \pm 1.84 \text{ nm}$ . The results for the diameters and distance between the voids in horizontal and vertical directions are summarized in Figure 4.

Looking carefully at the intensity distribution, one can see that the correlation is present in all the directions as shown in Figure 6. The figure is constructed of consecutive  $q_y = \text{const.}$  cut plots for the range above the Yoneda plain. The correlation peak forms a ring around the direct beam as indicated in Figure 6 with a transparent blue line. Since the

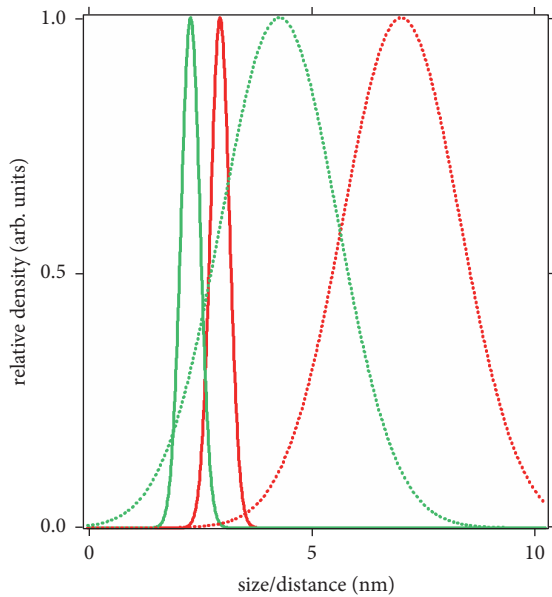


FIGURE 4: Distribution of void diameters (full lines) and correlation distances (dotted lines) for vertical (green lines) and horizontal (red lines) direction.

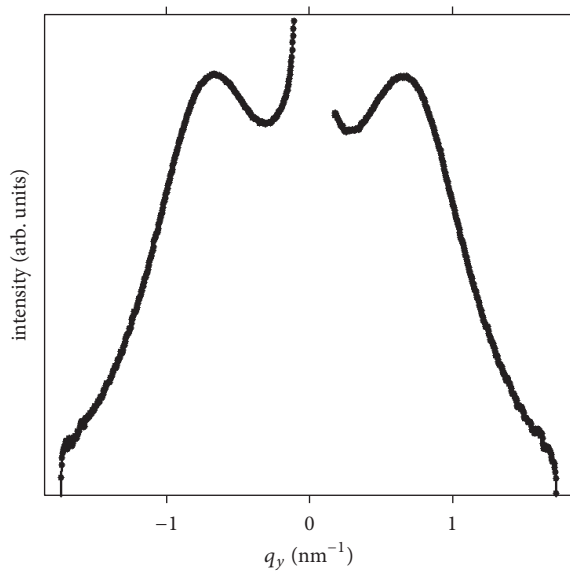


FIGURE 5: GISAXS intensity parallel to the sample surface taken at  $q_z = 0.2 \text{ nm}^{-1}$  (see two-dimensional GISAXS pattern in Figure 3(b)) for the annealed film.

voids are concentrated within the previously Ge containing layer, the correlation peak is strongest at the Yoneda plain, where scattering is parallel to this plain. In the perpendicular direction the correlation is enhanced into the Bragg peak as the periodicity of void layer positions is preserved after annealing. The slight variation in the voids position in vertical direction within the layers results in a correlation peak spreading from the Yoneda plain up, with the intensity rapidly decreasing due to the lower concentration of the offset voids. Namely, the deposited layers are not perfectly flat, but some

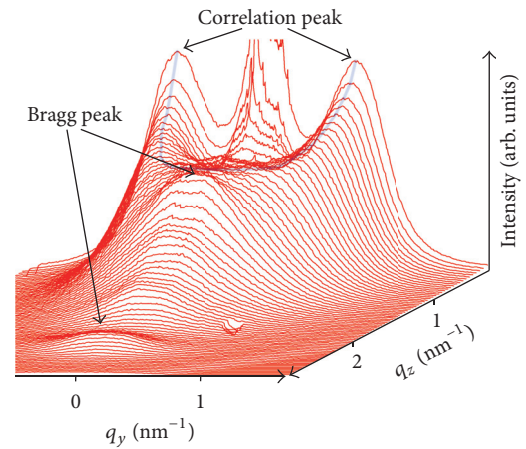


FIGURE 6: 3D plot of GISAXS intensities for the annealed sample. The Bragg sheets are indicated, as well as the signal maxima, due to the correlation (the transparent blue line).

surface roughness is present in the underlying layers and this is propagated upwards, with the upper layers thickness remaining more or less constant.

To support our findings we performed cross-section TEM analysis of the annealed samples where voids have been detected by GISAXS. Indeed as shown in Figure 7 the presence of voids is clearly evidenced. Each void measures approximately 5 nm in diameter. STEM-EDS mapping of the Si, Ge, and O distribution was performed on the same sample (selected area ROI, shown in Figure 7(a)). Although undetectable by Raman and XRD, Ge is still present in the layer and is homogeneously distributed throughout the layer (however, small Ge-free areas show the presence of voids).

Figure 8 shows the UV-VIS reflectance of the as-deposited  $\text{SiO}_2/\text{Ge}$  multilayer superstructure which could be used as antireflectance coating, since the reflectance is strongly reduced with respect to the Si substrate in the whole measured range. Quite similar is the behavior of the pure  $\text{SiO}_2$  layer deposited on Si, in the spectral range  $\lambda > 500 \text{ nm}$ . During annealing at  $800^\circ\text{C}$  the investigated sample substantially became a  $\text{SiO}_2$  layer with voids and a small remaining part of Ge (as revealed by EDS microscopy) and shows qualitatively a similar behavior as an amorphous  $\text{SiO}_2$  layer. The reflectance of a clean Si substrate is also added to Figure 8 as a reference.

Silicon rich layers [18] and/or  $\text{SiO}_2/\text{Ge}$  multilayers [19], after annealing at appropriate temperatures, produce a significant PL signal which indicates that structural changes, that is, nanoparticles or voids, developed in the films. In order to check the effect of voids creation within a  $\text{SiO}_2$  matrix the PL was measured from  $\text{SiO}_2$  layers with voids and compared with the PL from as-deposited  $\text{SiO}_2/\text{Ge}$  multilayers; see Figure 9. A very intensive PL peak centered at about 500 nm can be seen. Such signal, but with lower intensity, was already observed in samples with Ge nanoparticles and attributed to defective  $\text{SiO}_x$  nanolayers close to the Ge/ $\text{SiO}_2$  interface [19].

The emission and relaxation dynamics of this peak was explored and the results are given in the inset of Figure 9. The

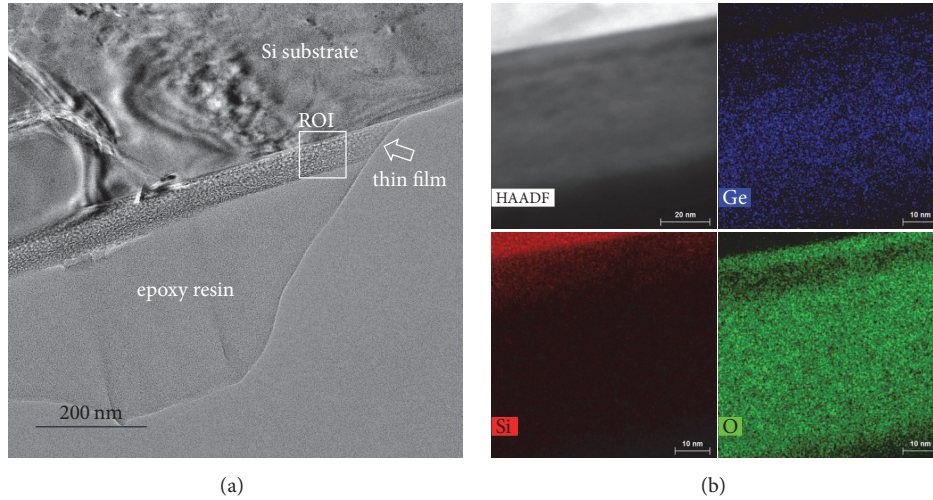


FIGURE 7: (a) Overview bright-field TEM micrograph of an annealed sample, showing the single-crystal Si substrate at the top, followed by layered voids formed in the amorphous SiO<sub>2</sub> thin-film layer. The thickness of the whole thin-film layer at this point is 60 nm. The rectangular region of interest (ROI) was analysed in detail in (b), where STEM-EDS mappings of the fine structures were performed.

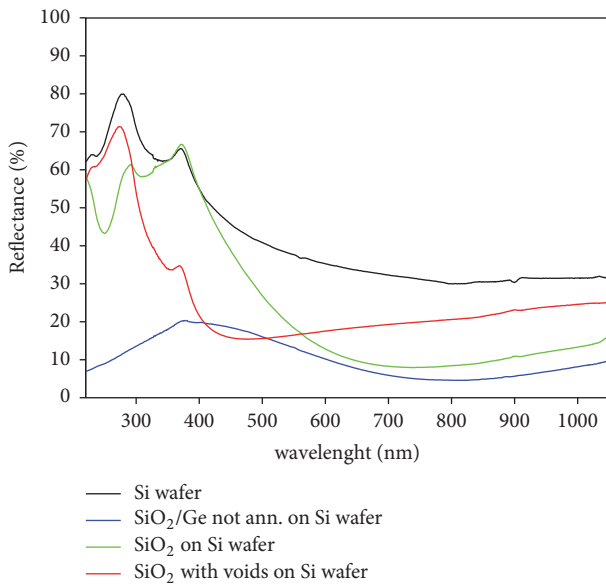


FIGURE 8: UV-Vis reflectance spectra of the as-deposited sample (SiO<sub>2</sub>/Ge multilayers, blue curve), annealed sample (substantially SiO<sub>2</sub> with voids, red curve), and pure silica layer of the same thickness (green curve) on Si substrate. The clean Si substrate was also measured for comparison (black curve).

decay curve has been fitted using two stretched exponential functions according to the expression:

$$I(t) = I_0 \exp\left(-\left(\frac{t}{\tau_{1,2}}\right)^{\beta_{1,2}}\right) \quad (1)$$

where  $\tau_{1,2}$  are the PL lifetimes and  $0 \leq \beta_{1,2} \leq 1$  are the dispersion exponents. The corresponding PL lifetimes and stretching constants are  $t_1 = 139 \pm 15$  ns with  $\beta_1 = 0.33 \pm 0.01$

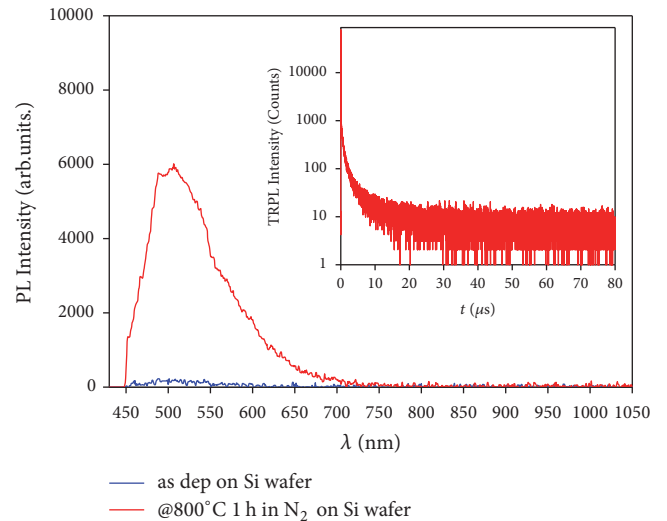


FIGURE 9: PL spectra of as-deposited (blue) and annealed (red, with voids) silica layer on Si substrate. The inset shows the time-resolved photoluminescence obtained from the annealed sample, recorded at 375 nm excitation wave length.

and  $t_2 = 7.0 \pm 0.7$  ns with  $\beta_2 = 0.30 \pm 0.01$ . These results are similar to previous findings in samples with Ge nanodots in silica matrix [13], where it was concluded that the PL is due to defected SiO<sub>x</sub> layers at the interface between Ge nanodots and the silica matrix. Likewise, here the PL originates from the border region around the voids.

To further confirm our statement that voids formed in SiO<sub>2</sub> matrix after a major Ge outdiffusion from the multilayer sample, the GISAXS results were analysed in the light of the Porod theory [20] and are presented in Figure 10. Assuming that the thickness of the shell enveloping the voids has a uniform thickness  $D$ , it is possible to estimate the parameter

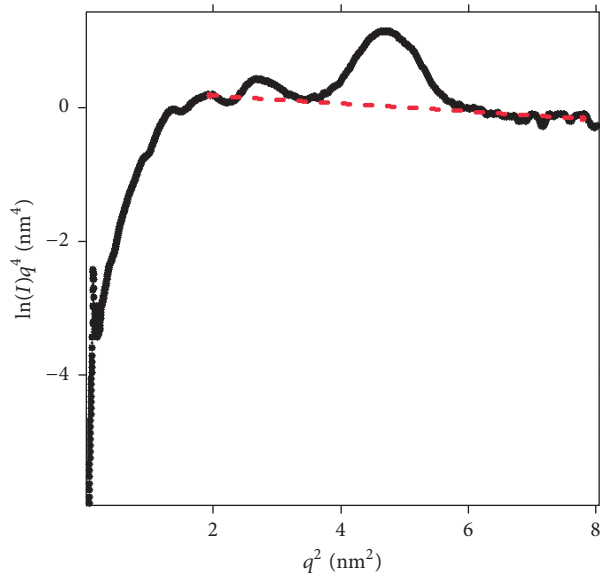


FIGURE 10: Plot of GISAXS intensity in the form  $\ln[q^4 I(q)]$  versus  $q^2$  for the  $\text{SiO}_2/\text{Ge}$  2/2 nm sample, annealed at  $800^\circ\text{C}$  and thus containing voids embedded in the  $\text{SiO}_2$  matrix. For  $q^2 > 6 \text{ nm}^{-2}$  the straight line (to the detector limit for the applied setup) shows the fit from which the thickness of the border region around the voids is calculated. The peak at  $q^2 = 4.5 \text{ nm}^{-2}$  represents the Bragg peak.

$\sigma$  of the layer, which describes the electron density gradient through [21]

$$\ln [q^4 I(q)] = \ln K - \sigma^2 q^2, \quad (2)$$

where  $q$  is the wave vector,  $I$  is the GISAXS intensity, and  $K$  is a constant.

The layer thickness  $D$  is related to  $\sigma$  by  $D = (2\pi)^{1/2} \sigma$  and was calculated to be 1.5 nm. The parameter  $D$  represents the thickness of the defected  $\text{SiO}_2$  layers surrounding the voids which are responsible for the PL activity.

#### 4. Conclusions

The structure and behavior of  $\text{SiO}_2/\text{Ge}$  multilayers deposited by e-gun on Si substrate is explored after annealing at  $800^\circ\text{C}$  in flowing  $\text{N}_2$  atmosphere. It is shown that such treatment drives out (outdiffuses) almost the complete Ge content, leaving behind voids in  $\text{SiO}_2$  matrix at the former Ge layer positions. Such voids are spherical with about 3 nm diameter. The average correlation distance is about 7 nm and 4 nm in horizontal and vertical directions, respectively. It is shown that the defected  $\text{SiO}_2$  layer around the voids causes very intensive photoluminescence with wavelengths close to 500 nm. The time-resolved PL analysis suggests that the mechanism of the observed void luminescence is similar to the one from defect layers at a  $\text{Ge}/\text{SiO}_2$  interface. The analysis of the GISAXS data in the light of the Porod theory shows that the voids are enveloped with a shell of disordered silica about 2 nm in thickness.

With this it was shown that this approach yields a well self-organized void formation within a  $\text{SiO}_2$  matrix at relatively low temperatures. The optical properties of such self-organized voids show interesting properties for application in silica photonics.

#### Conflicts of Interest

The authors declare that they have no conflicts of interest.

#### Acknowledgments

This work has been supported in part by the Croatian Science Foundation under Project no. 6135. The support from CREST Center, North Carolina Central University, Durham, NC, USA, is also appreciated.

#### References

- [1] Z. Yu, A. Raman, and S. Fan, "Fundamental limit of nanophotonic light trapping in solar cells," *Proceedings of the National Academy of Sciences of the United States of America*, vol. 107, no. 41, pp. 17491–17496, 2010.
- [2] S. Wiesendanger, M. Zilk, T. Pertsch, C. Rockstuhl, and F. Lederer, "Combining randomly textured surfaces and photonic crystals for the photon management in thin film microcrystalline silicon solar cells," *Optics Express*, vol. 21, no. 103, pp. A450–A459, 2013.
- [3] Y. Tanaka, K. Ishizaki, M. De Zoysa et al., "Photonic crystal microcrystalline silicon solar cells," *Progress in Photovoltaics*, vol. 23, no. 11, pp. 1475–1483, 2015.
- [4] Y. Gong and J. Vučković, "Photonic crystal cavities in silicon dioxide," *Applied Physics Letters*, vol. 96, no. 3, Article ID 031107, 2010.
- [5] Y. Gong, S. Ishikawa, S.-L. Cheng, M. Gunji, Y. Nishi, and J. Vučković, "Photoluminescence from silicon dioxide photonic crystal cavities with embedded silicon nanocrystals," *Physical Review B: Condensed Matter and Materials Physics*, vol. 81, no. 23, Article ID 235317, 2010.
- [6] L. Zhu, A. P. Raman, and S. Fan, "Radiative cooling of solar absorbers using a visibly transparent photonic crystal thermal blackbody," *Proceedings of the National Academy of Sciences of the United States of America*, vol. 112, no. 40, pp. 12282–12287, 2015.
- [7] E. N. Glezer, M. Milosavljevic, L. Huang et al., "Three-dimensional optical storage inside transparent materials," *Optics Express*, vol. 21, no. 24, pp. 2023–2025, 1996.
- [8] S. Kanehira, J. Si, J. Qiu, K. Fujita, and K. Hirao, "Periodic nanovoid structures via femtosecond laser irradiation," *Nano Letters*, vol. 5, no. 8, pp. 1591–1595, 2005.
- [9] D. Barba, F. Martin, J. Demarche, G. Terwagne, and G. G. Ross, "Nanocavities and germanium nanocrystals produced by Ge ion implantation in fused silica," *Nanotechnology*, vol. 23, no. 14, Article ID 145701, 2012.
- [10] C. Li, H. Feng, B. Liu et al., "Effect of nanocavities on Ge nanoclustering and out-diffusion in  $\text{SiO}_2$ ," *Nanotechnology*, vol. 28, no. 3, Article ID 035707, 2017.
- [11] B. Pivac, P. Dubček, J. Popović et al., "Influence of stress on the properties of Ge nanocrystals in an  $\text{SiO}_2$  matrix," *Journal of Applied Crystallography*, vol. 49, no. 6, pp. 1957–1966, 2016.

- [12] H. Amenitsch, S. Bernstorff, and P. Laggner, “High-flux beam-line for small-angle x-ray scattering at ELETTRA,” *Review of Scientific Instruments*, vol. 66, no. 2, pp. 1624–1626, 1995.
- [13] Y. Sasaki and C. Horie, “Resonant Raman study of phonon states in gas-evaporated Ge small particles,” *Physical Review B: Condensed Matter and Materials Physics*, vol. 47, no. 7, pp. 3811–3818, 1993.
- [14] P. Eisenberger and W. C. Marra, “X-ray diffraction study of the Ge(001) reconstructed surface,” *Physical Review Letters*, vol. 46, no. 16, pp. 1081–1084, 1981.
- [15] J. R. Levine, J. B. Cohen, Y. W. Chung, and P. Georgopoulos, “Grazing-incidence small-angle X-ray scattering: new tool for studying thin film growth,” *Journal of Applied Crystallography*, vol. 22, no. 6, pp. 528–532, 1989.
- [16] B. Pivac, P. Dubček, I. Capan et al., “GISAXS study of Si nanostructures in SiO<sub>2</sub> matrix for solar cell applications,” *Physica Status Solidi (a) – Applications and Materials Science*, vol. 210, no. 4, pp. 755–759, 2013.
- [17] M. Störmer, J.-M. André, C. Michaelsen, R. Benbalagh, and P. Jonnard, “X-ray scattering from etched and coated multilayer gratings,” *Journal of Physics D: Applied Physics*, vol. 40, no. 14, article no. 022, pp. 4253–4258, 2007.
- [18] A. Coyopol, G. García-Salgado, T. Díaz-Becerril et al., “Optical and structural properties of silicon nanocrystals embedded in SiO<sub>x</sub> matrix obtained by HWCVD,” *Journal of Nanomaterials*, vol. 2012, Article ID 368268, 2012.
- [19] J. Dasović, P. Dubček, I. Pucić, S. Bernstorff, N. Radić, and B. Pivac, “The interface quality of Ge nanoparticles grown in thick silica matrix,” *Applied Surface Science*, vol. 414, pp. 1–7, 2017.
- [20] B. Pivac, P. Dubček, J. Dasović, H. Zorc, and S. Bernstorff, “Study of the interface layers between Si nanoparticles and SiO<sub>2</sub> matrix deposited by e-gun evaporation,” *Physica Status Solidi (b) – Basic Solid State Physics*, p. 1700633, 2018.
- [21] Z. H. Li, Y. J. Gong, D. Wu et al., “A negative deviation from Porod’s law in SAXS of organo-MSU-X,” *Microporous and Mesoporous Materials*, vol. 46, no. 1, pp. 75–80, 2001.